Maren Lium

Spiral Image Reconstruction for 7T MRI with Gradient System Characterization

Master's thesis in Applied Physics and Mathematics
Supervisor: Johanna Vannesjö
June 2022

Master's thesis

◼ NTNU
Norwegian University of
Science and Technology

Maren Lium

Spiral Image Reconstruction for 7T MRI with Gradient System Characterization

Master's thesis in Applied Physics and Mathematics
Supervisor: Johanna Vannesjö
June 2022

Norwegian University of Science and Technology
Faculty of Natural Sciences
Department of Physics

NTNU
Norwegian University of
Science and Technology

Abstract

Background and purpose: Single-shot spiral imaging is of high interest as an alternative to EPI due to its increased time efficiency and decreased sensitivity to motion. However, spiral imaging is highly susceptible to imperfections of the gradient system, which causes image distortions, blurring, and signal loss due to k-space trajectory deviations and eddy-current induced temporal magnetic field fluctuations. This project aims to develop an offline image reconstruction pipeline that uses field responses predicted by an impulse response model of the gradient system at a 7T MR scanner.

Methods: Gradient system characterization was performed on a 7T system based on field response measurements of a phantom with a thin-slice excitation approach. The measured gradient impulse response function (GIRF) was used to predict field responses to single-shot spiral gradient sequences, which were compared to measured responses in addition to the nominal gradients. Image reconstruction based on the predicted trajectories was performed for phantom and in vivo data acquired with a 32-channel head receive coil, and the images were compared with reconstructions based on separate trajectory measurements and the nominal trajectories.

Results: A GIRF was successfully characterized and yielded predictions that agreed well with the separately measured gradients. The nominal spiral trajectories deviated significantly more from the separately measured trajectories compared to the GIRF-predictions, even with delay-correction of the nominal trajectories. Image reconstruction using the GIRF-predicted trajectories resulted in images that were comparable to using separate trajectory measurements. There were observed image artifacts even in the reconstructions based on measured trajectories. For low R-values, distortions and blurring due to off-resonance effects were most prominent, and residual aliasing dominated for high R-values.

Conclusion: An offline image reconstruction pipeline for single-shot imaging with spiral k-space trajectories has been developed and tested for a 7T MR scanner. A GIRF with both self and 0th order cross-terms can be determined with simple thin-slice excitation phantom measurements, and GIRF-predicted trajectories yield highly accurate results for the 0th and 1st order field responses for technically challenging single-shot spiral readouts. The GIRF-predicted field responses enable image reconstruction with the same quality as separately measured field responses, although some image artifacts remain, which could be addressed in later work.

Sammendrag

Bakgrunn og formål: Spiralavbildning i MR er av stor interesse som et alternativ til EPI på grunn av økt tidseffektivitet og redusert sensitivitet for bevegelse. Men spiralavbildning er svært følsom for avvik i oppførselen til gradientsystemet. Slike avvik vil føre til forvrengninger, uskarphet, og tap av signal i det rekonstruerte bildet på grunn av endringer i banen i k-rommet og tidsavhengige variasjoner i det magnetiske feltet som følge av virvelstrømmer. Målet til dette prosjektet er å legge til rette for bilderekonstruksjon som korrigerer for avvik i gradientsystemet ved å predikere endringer i k-romsbanen og magnetfeltet på en 7T MR-maskin. Prediksjonene skal gjennomføres med en impulsresponsmodell.

Metode: Karakteriseringen av gradientsystemet til et 7T-system ble gjennomført basert på målinger av et fantom med en tynnsjiktmetode. Den målte impulsresponsen til gradientsystemet (GIRF) ble deretter brukt til å predikere feltresponser til spiralsekvenser som ble sammenliknet med faktiske målinger av feltresponsene og de ukorrigerte spiralbanene. De predikerte k-romsbanene ble brukt til bilderekonstruksjon av både fantom- og in vivo-målinger med en 32-kanal mottaksspole for hodeavbildning. De rekonstruerte bildene ble sammenliknet med bilder rekonstruert med separate spiralmålinger og de ukorrigerte k-romsbanene.

Resultater: En GIRF ble beregnet og ga gradientprediksjoner som samsvarte bra med de målte spiralgradientene. Det var et betydelig større avvik for de ukorrigerte spiralbanene sammenliknet med GIRF-prediksjonene, selv når det ble medregnet en forsinkelse i de ukorrigerte spiralbanene. Bilderekonstruksjonen med GIRF-prediksjoner resulterte i bilder som var sammenliknbare med bildene rekonstruert med målte spiralbaner. Selv med de målte spiralene ble det observert artefakter i de rekonstruerte bildene. For lave R-tall var det uskarpheter på grunn av ujevnheter i magnetfeltet som var mest framtredende, mens gjenværende foldningsfeil dominerte for høye R-tall.

Konklusjon: Bilderekonstruksjon for spiralavbildning har blitt utviklet og testet på en 7T-maskin. En GIRF som beskriver både 0. og 1. ordens feltrespons kan bli beregnet med enkle tynnsjiktmålinger av et fantom. GIRF-prediksjoner av spiralbaner gir presise resultater for avvik i magnetfelt og gradientform for avanserte spiralavlesninger. De predikerte feltresponsene oppnår bilderekonstruksjon av samme kvalitet som med målte feltresponser, til tross for at enkelte artefakter fortsatt forekommer.

Preface

This thesis was written as part of my master's degree in biophysics and medical technology at the department of physics at the Norwegian University of Science and Technology (NTNU), which I finished in the summer of 2022. The work presented in this thesis was carried out during the spring semester of 2022 and was a continuation of the project thesis of Ingeborg Sæten Skre which she performed in the fall semester of 2021. I would therefore like to express my gratitude for the groundwork she put into this project and acknowledge her contribution to large parts of the MATLAB code presented in appendix A.1.

I would like to thank Lars Kasper and Alex Jaffray at the Techna Institute of the University Health Network (UHN) in Toronto, Canada. I would not have been able to finish the reconstruction part of the project in time if I had not received their help or access to their code. I acknowledge their contribution to the Julia code presented in appendix A.2. I would also like to thank Desmond Tse at the 7T center at St. Olavs Hospital for setting up all the sequences used in this project. Finally, I would like to thank my supervisor Johanna Vannesjö for taking me on as a master's student on such short notice and allowing me to participate in an exciting research project. I have received invaluable guidance and feedback while I still had plenty of time to explore and get to know the research field by myself.

Maren Lium
Trondheim, June 2022

Contents

Abbreviations

ADC	Apparent diffusion coefficient
ASL	Arterial spin labeling
BOLD	Blood oxygenation-level dependent
BW	Bandwidth
CNR	Contrast-to-noise ratio
CT	Computed tomography
DWI	Diffusion-weighted imaging
emf	Electromotoric force
EPI	Echo-planar imaging
FA	Flip angle
FFT	Fast Fourier transform
fMRI	Functional magnetic resonance imaging
FOV	Field of view
FWHM	Full width at half maximum
GIRF	Gradient impulse response function
GRAPPA	Generalized autocalibrating partially parallel acquisitions
LTI	Linear and time-invariant
MR	Magnetic resonance
NMR	Nuclear magnetic resonance
qMRI	Quantitative magntic resonance imaging
RF	Radiofrequency
RMS	Root mean square
SENSE	Sensitivity encoding
SMASH	Simultaneous acquisition of spatial harmonics
SNR	Signal-to-noise ratio
TA	Acquisition time
TE	Echo time
TR	Repetition time
VS-EPI	Variable speed echo-planar imaging

1 Introduction

Magnetic resonance (MR) imaging is a non-invasive medical imaging technique that offers high-resolution images with great soft-tissue contrast without ionizing radiation. In addition to regular anatomical images, MR imaging may provide information about blood flow, diffusion, brain activity, and more. While it has long been used clinically for imaging all body parts, the main disadvantage of MR imaging is the long acquisition time needed for high-resolution images compared to alternative imaging techniques such as computed tomography (CT) or ultrasound. Some MR scans might take up to several minutes, resulting in reduced comfort for the patient and increased probability of motion, which will introduce artifacts in the images.

Some applications of MR imaging rely on fast acquisition to achieve time-series data, increase the signal-to-noise ratio (SNR), or limit the effects of patient movement. Some examples are blood oxygenation-level dependent (BOLD) functional MR imaging (fMRI) [1], arterial spin labeling (ASL) [2], and diffusion-weighted imaging (DWI) [3]. Single-shot imaging is needed to accomplish sufficiently short acquisition times. Single-shot schemes such as echo-planar imaging (EPI) [4] and spiral imaging [5] are fast imaging techniques that can collect all image data in a single readout by traversing all of k-space after one excitation, whereas conventional two-dimensional imaging schemes require N readouts to produce an image with $N \times N$ pixels. Another technique that has been developed to decrease scan time is parallel imaging, which in contrast to fast imaging allows this without compromising resolution. Parallel imaging is a technique that utilizes the additional spatial information from multiple receiver coils to reduce the amount of data needed per pixel, usually resulting in increasing imaging speed with a factor of 2-4 [6]. Single-shot and parallel imaging are complementary, and several MR imaging schemes that rely on fast acquisition use a combination of these two techniques.

Today, most single-shot sequences are based on EPI, but there has been an increased interest in spiral imaging since it has the potential for shorter acquisition time. As with all MR sequences, both EPI and spiral imaging rely on linear magnetic field gradients for spatial encoding of the images, but how these are implemented causes spiral imaging to be faster than EPI. However, there are still three main issues preventing routine use of spiral imaging [7, 8]: First, it is highly sensitive to imperfections in the gradient system, which will result in image distortion, blurring, and signal loss. Secondly, it is also greatly influenced by inhomogeneities in the static magnetic field B_0 inside the scanner, which is affected by the local susceptibility differences of the imaged object. B_0-inhomogeneities also cause blurring and signal loss. Finally, spiral imaging causes a more complicated reconstruction problem in combination with parallel imaging compared to EPI [9].

Several methods have been proposed to compensate or correct for errors due to gradient system imperfections. In most cases, these methods are sequence-specific. For EPI, a common method uses additional reference readouts to correct for phase inconsistencies between odd and even readout lines [10], and other post-processing strategies that do not require extra scans have also been proposed [11–13]. For spiral imaging, a method that estimates and corrects for net delays of the linear gradient field chains has been suggested [7]. However, sequence-specific correction strategies are limited by underlying model assumptions. A more robust approach is to measure the actual k-space trajectories due to gradient imperfections

1

and use them as the basis of image reconstruction [14–16]. The k-space measurements can either be performed before image acquisition [16–18], which requires a longer scan time, or they can be performed simultaneously [19–21], which requires additional expensive hardware.

Another solution to compensate for gradient system imperfections is to characterize the gradient system in a one-time effort and use this knowledge to predict the actual gradient behavior for all later imaging schemes. By assuming that the gradient system is linear and time-invariant (LTI) the behavior of the system can be fully described by the gradient impulse response function (GIRF), which can be found by measuring the field responses to known input gradients [22, 23]. Compensating for system imperfections with a GIRF may be performed without additional hardware and does not increase the scan time after the GIRF has been determined.

The two last issues that hinder the use of spiral imaging, B_0-inhomogeneities and image reconstruction, have recently been overcome by combining an extended signal model that incorporates static field imperfections and coil sensitivity encoding [24] with iterative reconstruction [9]. The extended signal model also includes dynamic imperfections in the external magnetic field, which may be observed through GIRF-predictions or k-space measurements before or during acquisition. Local B_0-inhomogeneities may be measured before the image acquisition and stored in a field map which is used to correct for errors caused by susceptibility differences during image reconstruction.

This project aims to implement single-shot spiral imaging at the 7 Tesla (T) MR scanner in Trondheim. For this purpose, an offline image reconstruction pipeline will be set up that corrects for k-space trajectory deviations and static field inhomogeneities. The k-space trajectories will be estimated with GIRF-predictions, and the impact of the predictions in image reconstruction will be assessed by comparing them with reconstructions based on the nominal k-space trajectories.

2 Theory

In this section, all the relevant theory required to understand the work performed in this project will be presented. It will start with the basic principles of MR imaging such as signal origin, k-space formalism, and static field inhomogeneity, before moving on to more advanced and specific subjects such as fast imaging techniques, k-space trajectory measurements, gradient system characterization, and parallel imaging.

2.1 Principles of MR imaging

MR imaging is an imaging technique that uses a strong external magnetic field and radiofrequency (RF) pulses to create three-dimensional anatomical and functional images of tissue. It is based on the well-known nuclear magnetic resonance (NMR) phenomenon, from which images are formed with spatial encoding principles. This section will explain the origin of the MR signal and how it is manipulated to provide spatial information. The content is mostly based on the book *Principles of Magnetic Resonance Imaging: A Signal Processing Perspective* by Liang and Lauterbur [25] unless otherwise specified.

2.1.1 The NMR phenomenon

As the name implies, the NMR phenomenon involves nuclei in the object to be imaged, magnetic fields that are applied externally by the radiologist, and the resonance phenomenon that follows from the interaction between the nuclei and magnetic fields. A fundamental property of nuclei is that nuclei with an odd number of protons and/or neutrons possess an angular momentum $\vec{J}$, usually called *spin*, which is a quantum mechanical property. Since nuclei are positively charged, they will also have an associated magnetic moment $\vec{\mu}$, which will interact with other magnetic fields. If nuclei with magnetic moments are placed in an external magnetic field, they will align either parallel or anti-parallel to the field, and they will start to precess about the direction of the field. This is illustrated in figure 2.1. The last effect is known as nuclear precession, and the precession frequency, called the Larmor frequency ω_0, is only dependent on the type of nucleus and the magnetic field strength

$$\omega_0 = \gamma B_0, \tag{2.1}$$

where γ is the gyromagnetic ratio of the nucleus and B_0 is the magnetic field strength. In MR imaging, the most common nucleus to image is the hydrogen nucleus ^{1}H due to its relatively strong magnetic moment and abundance in biological tissue.

Nuclear precession and magnetic resonance are quantum mechanical phenomena, but it is often more useful to use a classical approach when discussing MR theory. This may be done by introducing the net magnetization $\vec{M}$, which is the sum of all magnetic moments in the field of view (FOV). At room or body temperature, there will be a slight abundance of hydrogen nuclei, henceforth referred to as spins, aligned
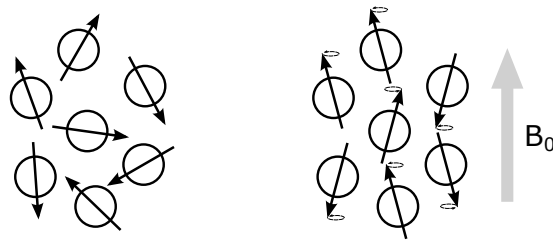
Figure 2.1: When exposed to a magnetic field $\vec{B}_0$, the spins will align either parallel or anti-parallel and start to precess at the Larmor frequency ω_0 about the direction of the field.

parallel to the magnetic field, resulting in a net positive magnetization. Although the individual spins are at an angle to the field direction they will be out of phase at equilibrium, and the net magnetization vector will be perfectly aligned with the external magnetic field. This is illustrated in figure 2.2. It is the net magnetization vector that is measured in an MR experiment.
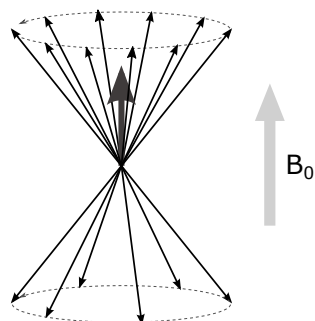
Figure 2.2: Illustration of the net magnetization of an ensemble of spins at equilibrium. More spins are aligned parallel to the field than antiparallel, which results in a net total magnetization M parallel to $\vec{B}_0$. The individual spins are out of phase, which results in no net magnetization perpendicular to the magnetic field.

2.1.2 The MR signal

To measure the magnetization of a sample, the net magnetization vector must have a component in the transverse plane perpendicular to the static magnetic field $\vec{B}_0$. In MR, this is achieved by "pushing" the net magnetization into the transverse plane using an RF-pulse. If an RF-pulse with the same frequency as the Larmor frequency is applied perpendicular to the static magnetic field, the net magnetization will start to precess about the applied magnetic field of the RF-pulse. This causes the net magnetization to spiral down towards the transversal plane in the laboratory frame of reference as shown in figure 2.3a. By changing the frame of reference to one that is rotating about the direction of $\vec{B}_0$ at the Larmor frequency, the spiraling motion is reduced to a tilting of the magnetization into the x'y'-plane. The x'- and y'-axis are the axes of the rotating frame of reference. This is illustrated in figure 2.3b. The tilting angle, or flip angle (FA), of the net magnetization, is decided by the duration of the RF-pulse.

Now that the net magnetization vector is perpendicular to $\vec{B}_0$, and still precessing at the Larmor frequency, the time varying magnetization can induce a voltage $V(t)$ in a receiver coil, as stated by the Faraday law of induction

$$V(t) = -\frac{\mathrm{d}\Phi_B(t)}{\mathrm{d}t},\tag{2.2}$$

where $\Phi_B(t)$ is the flux of magnetic field lines through the receiver coil at time t.

Neglecting relaxation effects, the signal $S(t)$ at time t after RF excitation detected by the receive coil is
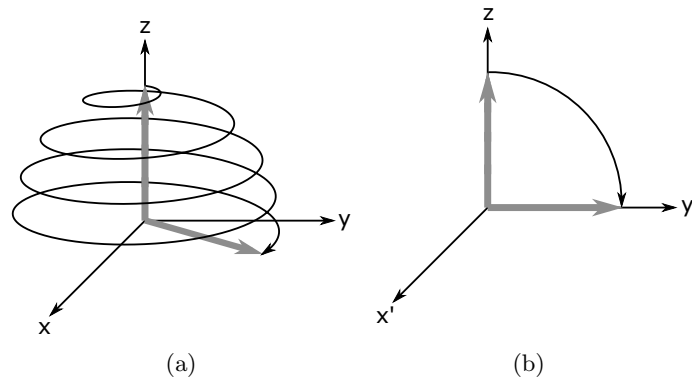
Figure 2.3: Illustration of the RF-excitation of the net magnetization vector in (a) the laboratory frame of reference and (b) the rotating frame of reference.

proportional to the volume integral of the spin density $\rho(\vec{r})$

$$S(t) \propto \int_V \rho(\vec{r}) e^{-i\phi_s(\vec{r},t)} \mathrm{d}^3 r, \tag{2.3}$$

where $\phi_s(\vec{r}, t)$ is the phase of the signal at time t which is given by the time integral of the frequency $\omega(\vec{r}, t)$

$$\phi_s(\vec{r}, t) = \int_0^t \omega(\vec{r}, \tau) \mathrm{d}\tau. \tag{2.4}$$

2.1.3 Spatial encoding

In order to form images from the received signal, which part of the signal that comes from each voxel in the subject must be distinguished. In MR, this is achieved by applying linear field gradients $\vec{G}(t)$ such that the total magnetic field along the z-direction at position $\vec{r}$ is

$$B(\vec{r}) = B_0 + \vec{G}(t) \cdot \vec{r}, \tag{2.5}$$

when the static magnetic field B_0 is applied along the z-direction. As can be seen from the Larmor equation (2.1), this translates into a spatially varying frequency that can be used to locate the signal

$$\omega(\vec{r}, t) = \omega_0 + \gamma \vec{G}(t) \cdot \vec{r}. \tag{2.6}$$

If a linear field gradient is applied during excitation of the sample it is termed a *slice selective* gradient, and if it is applied after excitation to spatially encode the signal it is termed a *spatial encoding* gradient. In the case of a slice selective gradient, the frequency of the RF-pulse determines which slice along the direction of the gradient is excited. Since the spins outside the slice have different resonance frequencies they will not be affected by the RF-pulse. Usually, slice selective and spatial encoding gradients are combined to form images. First, a slice selective gradient is applied in one direction, and then spatial encoding gradients are applied in the two remaining spatial directions.

2.1.4 k-space formalism

A useful concept for MR image acquisition is *k-space*. By applying a spatial encoding gradient for a given amount of time, the spins will get a phase shift corresponding to their location in space as described by

$$\phi_s(\vec{r}, t) = \omega_0 t + \gamma \vec{r} \cdot \int_0^t \vec{G}(\tau) \mathrm{d}\tau, \tag{2.7}$$

Figure 2.4: Illustration of the spatial frequency induced by the spatial encoding gradients. The first figure shows an array of spins after RF excitation. Then, the spins are exposed to a gradient G_y 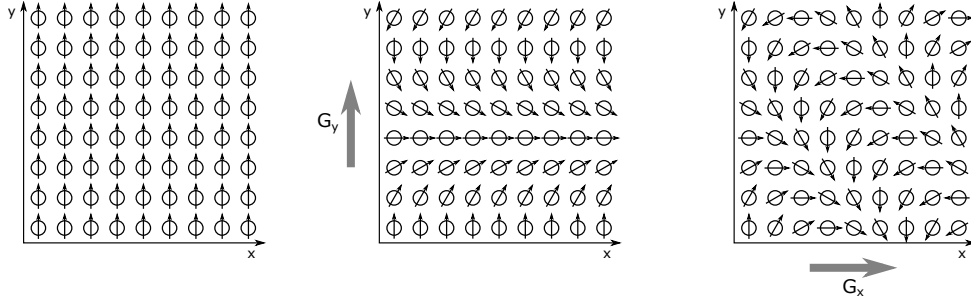for a given time, which induces a phase shift along the y-direction. In the third figure, the spins are also exposed to a gradient G_x which induces a phase shift along the x-direction as well.

which is simply the time integral of the frequency presented in equation (2.5), thus creating a *spatial frequency*. This is illustrated in figure 2.4 after applying gradients in the x- and y-directions in a slice.

When acquiring data for an MR image, the data is sampled and stored in k-space. The k-space of an image is usually stored slice-wise, with a two-dimensional k-space for each image slice. The axes of these slices are commonly termed k_x and k_y and are defined as follows

$$k_x(t) = \gamma \int_0^t G_x(\tau)\mathrm{d}\tau \tag{2.8a}$$

$$k_y(t) = \gamma \int_0^t G_y(\tau)\mathrm{d}\tau, \tag{2.8b}$$

where G_x and G_y are spatial encoding gradients applied in the x- and y-direction, respectively.

Assume that a slice selective gradient is applied in the z-direction, parallel to $\vec{B}_0$, so that only one slice at a given z-position is excited. By substituting the expressions in equations (2.7) and (2.8) into the signal equation presented in equation (2.3), and demodulating to remove the carrier signal (ω_0), one gets

$$S(k_x, k_y) \propto \int_{-\infty}^{\infty} \int_{-\infty}^{\infty} \rho(x, y)e^{-i(k_x x + k_y y)}\mathrm{d}x\mathrm{d}y, \tag{2.9}$$

where the time dependency is given implicitly through $k_x = k_x(t)$ and $k_y = k_y(t)$. Thus, the trajectory along which the signal is being sampled in time is given by the strength and direction of the applied gradients over time. By varying the gradients, it is theoretically possible to maneuver through k-space in any desired pattern. In other words, the role of the spatial encoding gradients $G_x(t)$ and $G_y(t)$ is to map the measured time signal from the object onto a spatial frequency signal in k-space. Based on this knowledge, different gradient sequences can be designed to traverse k-space along selected paths known as k-space trajectories.

From equation (2.9), the MR signal can be recognized as the two-dimensional Fourier transform of the spin density distribution within the imaged object. An image of the spin distribution can then be recovered by doing an inverse Fourier transform of the signal. Note that to form an image in this way, the k-space of the image must be *fully sampled*. For k-space to be fully sampled means that there are enough sampling points with the right density so that an image with the desired resolution and FOV can be reconstructed. There must be an equal number of k-space sampling points as pixels in the reconstructed image, and the FOV and resolution are defined by the density and maximum values of the k-space sampling points, respectively. This is illustrated in figure 2.5, where the relationship is given by

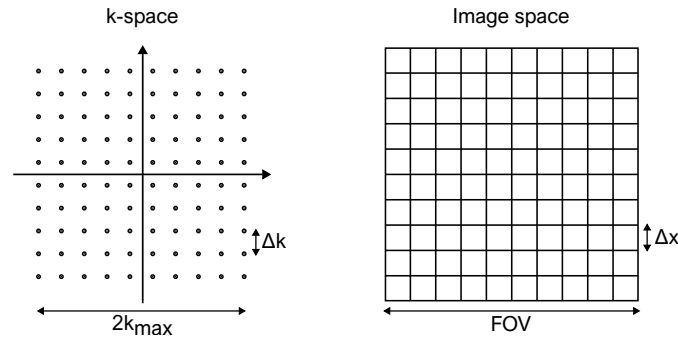$$\Delta k = \frac{1}{\mathrm{FOV}} \qquad \Delta x = \frac{1}{2k_{max}}. \tag{2.10}$$

Figure 2.5: Illustration of the relationship between k-space sampling density and resolution (Δx) and FOV in the image.

2.1.5 B_0-inhomogeneity and B_0-mapping

When an object is placed inside the MR scanner, it will be magnetized according to its magnetic susceptibility χ, which describes the amount of internal polarization for a given external magnetic field strength. Materials are classified as diamagnetic, paramagnetic, or ferromagnetic depending on how they are magnetized in an external magnetic field. Diamagnetic materials have a negative susceptibility, and the internal magnetization will oppose the external magnetic field, resulting in a lower total field. Paramagnetic and ferromagnetic materials have positive susceptibilities, and their internal magnetization is parallel to the external field, resulting in a higher total field. This is illustrated in figure 2.6. Most biological materials are diamagnetic since they consist of water, while air is slightly paramagnetic. Different tissues and tissue-air interfaces will cause magnetic field inhomogeneities when placed inside the scanner, which will cause mismapping of data and artifacts due to varying precessional frequencies.
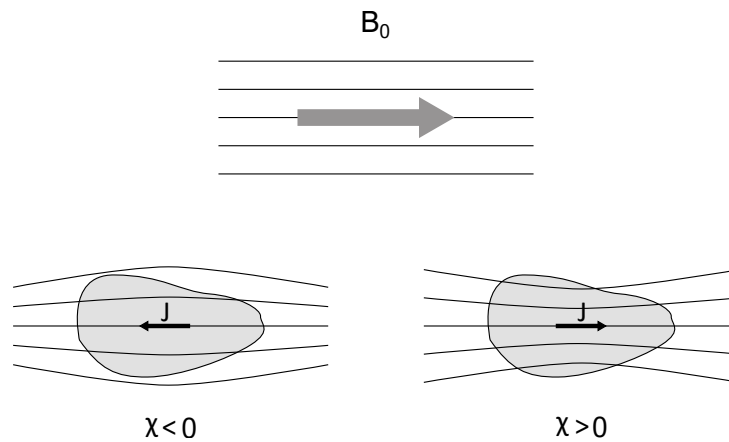
Figure 2.6: How materials with different magnetic susceptibilities affect the total field when placed inside an external magnetic field B_0. Diamagnetic materials ($\chi < 0$) will get an internal polarization J that opposes the external field, while the internal polarization in para-/ferromagnetic materials ($\chi > 0$) will be in the same direction as the external field.

It is therefore useful to have a map that provides information about the static inhomogeneities in the magnetic field. This can be achieved by acquiring the same image at two different echo times (TE), which simply denotes the center of the acquisition window. Both images can be acquired after a single excitation. Since the precessional frequency is directly proportional to the magnetic field strength, as described by equation (2.1), and the two images have been exposed to the same linear field gradients, the phase difference at a given position will be proportional to the magnetic field strength $B(\vec{r})$. Note that the signal has been demodulated to remove the carrier, or resonance, frequency $\omega_0 = \gamma B_0$, so that the phase difference at position $\vec{r}$ is due to the field offset from the assumed value of the magnetic field

$\Delta B_0(\vec{r}) = B(\vec{r}) - B_0$:

$$\phi(\vec{r}, TE_2) - \phi(\vec{r}, TE_1) = \gamma \Delta B_0(\vec{r})(TE_2 - TE_1)$$

$$\Delta B_0(\vec{r}) = \frac{1}{\gamma} \frac{\phi(\vec{r}, TE_2) - \phi(\vec{r}, TE_1)}{TE_2 - TE_1}, \tag{2.11}$$

where $\phi(\vec{r}, TE_1)$ and $\phi(\vec{r}, TE_2)$ are the phases at position $\vec{r}$ of the images acquired at echo times TE_1 and TE_2, respectively. Equation 2.11 can then be used to calculate a B_0-map, or field map, from the double-echo gradient echo sequence which describes the field offset on a voxel-level. Note that this method will not be able to account for temporal changes in the magnetic field.

2.1.6 Concomitant fields

In MR theory it is generally assumed that the magnitude of the magnetic field is equal to the z-component B_z. The magnitude at position $\vec{r} = x\hat{x} + y\hat{y} + z\hat{z}$ is given by equation (2.5), and can be expanded to

$$B_z = B_0 + xG_x + yG_y + zG_z, \tag{2.12}$$

with $\vec{G} = G_x\hat{x} + G_y\hat{y} + G_z\hat{z}$. However, for Maxwell's equations to hold, there must also appear one or two transverse components B_x and B_y when applying a linear field gradient [7]. These transverse field terms are known as *concomitant fields*, and the true magnitude of the magnetic field when applying the linear field gradients is

$$B = \sqrt{B_x^2 + B_y^2 + B_z^2} \tag{2.13}$$

where B_z is given by equation (2.12).

The size and direction of the concomitant fields can be computed from Maxwell's equations and are as follows [7]

$$\text{Apply } G_x \longrightarrow B_x = zG_x,$$
$$\text{Apply } G_y \longrightarrow B_y = zG_y,$$
$$\text{Apply } G_z \longrightarrow B_x = -\frac{x}{2}G_z \text{ and } B_y = -\frac{y}{2}G_z.$$

Due to the transverse concomitant fields, the magnitude of the magnetic field will be slightly larger than what is predicted with the assumption in equation (2.12), as is illustrated in figure 2.7. Since the Larmor frequency depends on the magnetic field strength, this will result in a phase error over time $d\phi_c = \gamma \Delta B_c dt$ where $\Delta B_c = \sqrt{B_x^2 + B_y^2 + B_z^2} - B_z$. By expanding ΔB_c as a Taylor series to first order, which is sufficient for field strengths of $B_0 > 1\text{T}$, one gets [7]

$$d\phi_c = \frac{\gamma}{2} \frac{dt}{B_0} \left(z^2(G_x^2 + G_y^2) + \frac{1}{4}(x^2 + y^2)G_z^2 - xzG_xG_y - yzG_yG_z \right). \tag{2.14}$$

Note that since $\Delta B_c > 0$, the phase error is always positive irrespective of the polarity of the applied gradients. The phase error will also decrease with increasing static magnetic field B_0, as seen from the factor $1/B_0$.

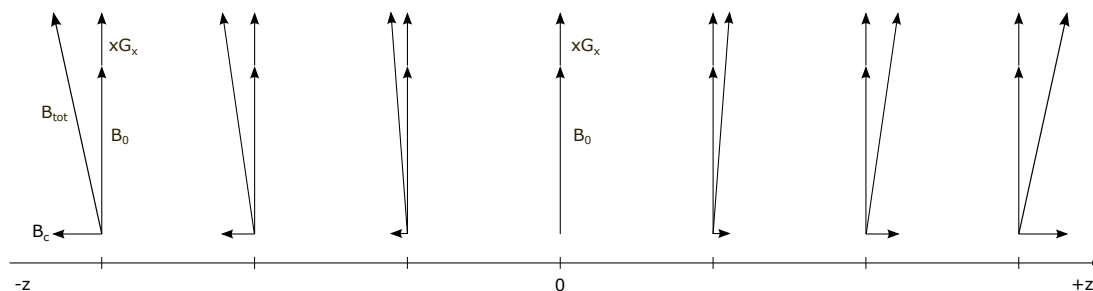
Figure 2.7: Illustration of concomitant fields as a result of applying a linear field gradient G_x, and how it makes the total magnetic field B_{tot} deviate from the static magnetic field B_0 as the distance from the isocenter along with the z-direction increases. Note that the x-value is constant.

2.2 Fast imaging sequences

Fast imaging is one of the most significant areas of MR imaging and is one of the main topics in this project. It is therefore essential to have a good intuition on how it works and be familiar with the benefits and drawbacks of sampling larger areas of k-space at once. Two imaging sequences that are of particular interest in this project are EPI and spiral imaging, since they have the possibility of sampling all of k-space in one excitation.

2.2.1 Echo-planar imaging

EPI is an ultra-fast MR imaging sequence that covers all or large portions of k-space after a single RF-excitation, yielding total image acquisition in a fraction of a second. This section will consider the case of full k-space coverage after each excitation, known as single-shot EPI.

A typical rectilinear EPI gradient sequence is presented in figure 2.8a with the corresponding k-space trajectory presented in figure 2.8b. The sequence initiates with a slice selection along the z-direction, which excites a slice in the xy-plane. Then, prephasing gradients are applied in both the x- and y-direction before the data acquisition, which specifies the starting position in k-space. Finally, a series of periodic bipolar gradients and gradient blips are applied in the x- and y-directions, respectively, during which the data is sampled. The bipolar gradients along the x-direction shift the position back and forth in the k_x-direction while the gradient blips along the y-direction shift the position in k_y between each line until all of k-space is covered.

Since single-shot EPI needs to cover all of k-space between each RF excitation, special demands are placed on the MR hardware. Because the acquisition needs to be fast to avoid signal decay, the gradients have to be strong and able to change polarity quickly. The illustration in figure 2.8a does not account for the rise-time of the gradients, and such immediate responses as illustrated are not realistic. EPI requires gradient systems with slew rates of about 200 T/m/s and maximum gradient strengths of about 20 mT/m. In comparison, normal imaging sequences usually have slew rates of about 17 T/m/s and maximum gradient strengths of about 10 mT/m.
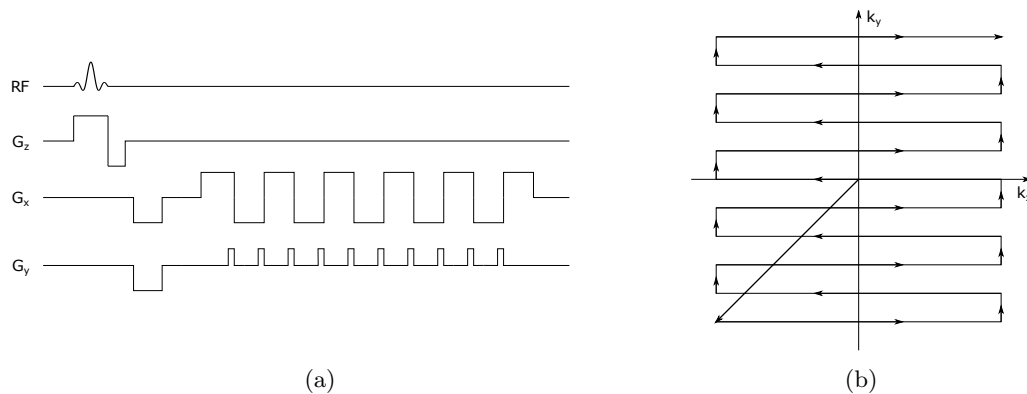
Figure 2.8: (a) Single-shot EPI sequence and (b) corresponding k-space trajectory. The rise-time of the gradients has been ignored for simplicity.

Due to the large bipolar gradients during readout, EPI is prone to artifacts such as blurring, distortion, and ghosting. This is due to the high sensitivity of phase errors that follows from the strong gradients and the long readout time that results in a low bandwidth (BW). Ghosting in EPI is an artifact that appears as two distinct copies of the object shifted $N/2$ pixels along the phase encoding direction, which is the direction along which the blips are applied. An example of the ghosting artifact is presented in figure 2.9 toghether with an illustration of the cause of the artifact.
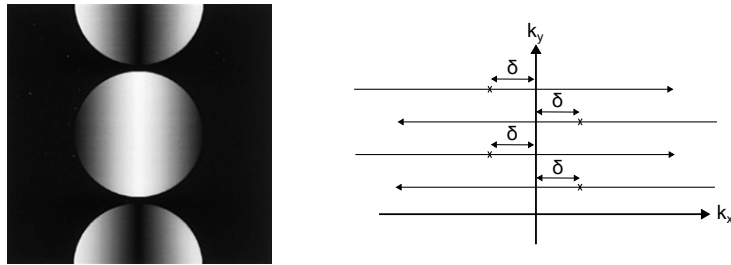
Figure 2.9: Illustration of EPI ghosting due to eddy current-induced phase shifts in the alternating frequency encoding lines in EPI. The figure is adapted from the article by Grieve, Blamire, and Styles [26].

If the forward and backward readout lines in EPI are not exact mirror images of each other, artifacts will be the result. If there is a phase shift between the alternating lines, as illustrated to the right in figure 2.9, the result will be discrete ghosts, as shown to the left in figure 2.9. Such phase shifts are usually caused by the induction of eddy currents in the gradient hardware due to the alternating polarity of the strong frequency encoding gradients.

2.2.2 Spiral imaging

Spiral imaging utilizes increasing sinusoidal gradients in both the x- and y-direction to create a spiraling k-space trajectory that covers all of k-space. The efficient use of the gradient system that avoids the sharp turns in k-space as seen in EPI, as well as not needing to sample the outer edges of k-space, causes spiral imaging to have a shorter readout length for a given resolution and FOV compared to EPI. There are many ways to design spiral trajectories, but the most common trajectory is the archimedean spiral where the successive turns of the spiral have a constant separation [27], which is the type of spiral sequence that will be used in this project.

An archimedean spiral imaging gradient sequence is presented in figure 2.10a with the corresponding k-space trajectory presented in figure 2.10b. The principle of the gradient sequence is similar to the one presented for EPI, with a slice selection and k-space sampling with oscillating spatial encoding gradients. In contrast to rectilinear EPI, the oscillating gradients have a gradually increasing strength, and the data points are not located on a cartesian grid. Thus, spiral imaging is more susceptible to experimental errors such as hardware imperfections and eddy currents. Such errors will cause the gradients to deviate from the planned shapes which will cause the measured k-space trajectory to diverge from the ideal, or nominal, track. If this is not accounted for during image reconstruction, there may occur severe blurring, signal loss, or other artifacts in the image.

(a)   (b)

Figure 2.10: (a) Archimedean spiral imaging sequence and (b) corresponding k-space trajectory. The rise-time of the slice-selective gradient has been ignored for simplicity.

2.3 Sources to gradient imperfections
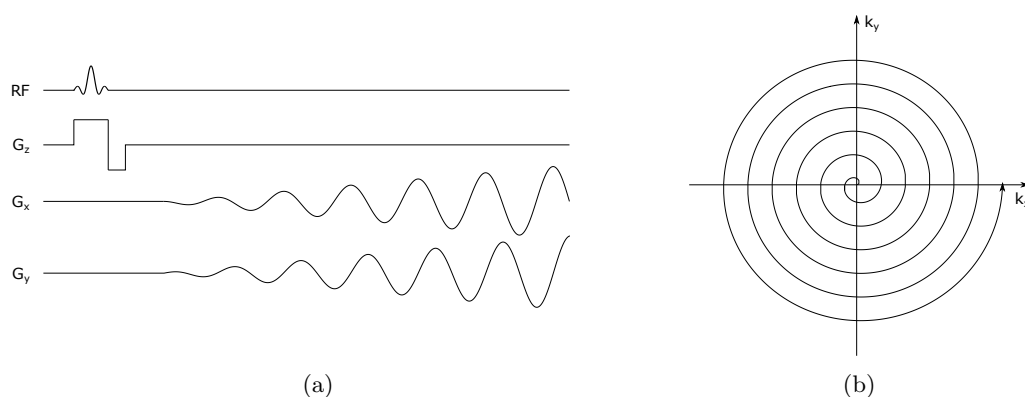
As previously stated, fast imaging sequences such as EPI and spiral imaging are highly sensitive to imperfections in the gradient waveforms. Gradient imperfections may occur for several reasons, and two of them are eddy currents effects and hardware imperfections, which will be described in this section.

Eddy current induction

When there is a changing magnetic field in proximity to a conducting wire, Faraday's law states that there will be induced an electromotoric force (emf) ϵ in the wire as given by [28]

$$\epsilon = -\frac{\mathrm{d}\Phi_B}{\mathrm{d}t}, \tag{2.15}$$

where Φ_B is the flux of magnetic field lines through the conducting wire. The minus sign was introduced by Lenz [28] and indicates that the emf will drive a current in the loop that induces a magnetic field that opposes the changing flux.

When applying time-varying linear field gradients in an MR system, there will be a change in flux through all the conducting hardware that the MR system consists of. This will induce an emf that will drive eddy currents in the hardware, which cause unwanted time-varying gradients and changes in the static magnetic field. As can be seen from equation (2.15), stronger and more rapidly changing gradients will give rise to larger eddy current effects, which explains why fast imaging schemes such as EPI and spiral imaging are prone to eddy current induced artifacts.

Eddy currents can be modeled as a linear response to the changing gradient field [29]

$$B_e(t) = -\frac{\mathrm{d}G}{\mathrm{d}t} * h_e(t), \tag{2.16}$$

where $B_e(r,t)$ represents the eddy current field induced by the changing gradient field G, $*$ is the convolution operator, and h_e describes the eddy current response of the MR system. For a more in-depth description of the properties of linear systems, see section 2.5.

Eddy currents have a non-linear spatial dependence [30], but in many cases, it is sufficient to use a linear approximation,

$$B_e(r,t) = B_{0e}(t) + G_e(t) \cdot r, \tag{2.17}$$

where $B_{0e}(t)$ and $G_e(t)$ are the 0th and 1st order spatial components of the eddy current field, respectively, and r is the spatial location.

2.3.1 Mechanical vibrations of gradient hardware

When a current I passes through a wire segment $\mathrm{d}\vec{l}$ in the presence of a magnetic field $\vec{B}$, the wire experiences a force known as the Lorentz force [28], which is given by

$$\mathrm{d}\vec{F} = \vec{I}\mathrm{d}l \times \vec{B}. \tag{2.18}$$

To generate linear field gradients in MR imaging, currents are run through gradient coils. Since these coils are in the presence of the static magnetic field, they will experience a force as stated in equation (2.18). In the case of rapidly switched gradient fields, strong time-dependent mechanical forces are produced that can stimulate modes of vibration in the gradient coils and cause vibrations under resonance conditions [31]. Vibrations in the gradient coils can cause unwanted shifts [31] and fluctuations [32] in the magnetic field.

2.4 Measuring k-space trajectories

Due to the mechanisms described in section 2.3, the actual k-space trajectories will deviate from the planned ones. It is necessary to have a way to measure the actual trajectories to describe the error and to predict the true trajectories at a later stage. This section will present a method for measuring the correct k-space trajectory of a gradient waveform which makes use of a thin-slice excitation, as first described by Duyn et al. [16] and extended by Robison et al. [29]. This method enables corrections for the eddy current induced modulation of the linear gradients, as well as correcting the effects of eddy current-induced magnetic field fluctuations $B_{0e}(t)$. Most modern MR systems compensate for the modulation of gradients, and some scanners also have built-in B_{0e}-correction. Despite this, residual B_0 eddy currents may remain uncorrected.

The proposed method measures the signal phase from a uniform spherical phantom to measure the k-space trajectory. It requires four measurements in order to determine the trajectory $k_x(t)$ from the gradient field pulse $G_x(t)$, which are illustrated in figure 2.11. Each measurement starts with a slice selective pulse that excites the slice at position x_0 or $-x_0$ and then applies the gradient pulse to be measured $G_x(t)$ during signal detection. At each position, the measurement is repeated with a positive and negative gradient.
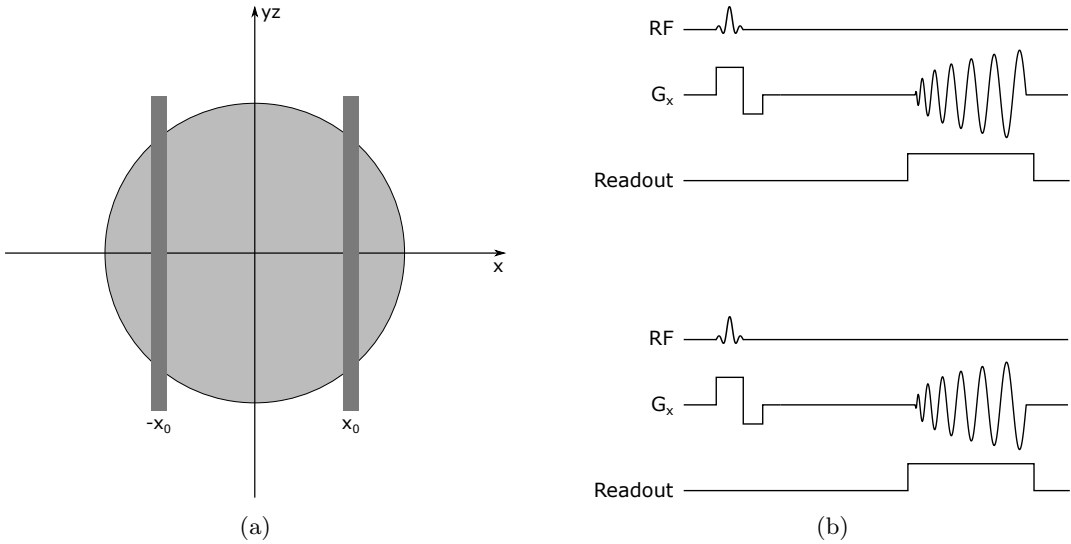
Figure 2.11: Measuring k-space. The illustration in (a) depicts the experimental setup and (b) shows the sequence diagrams of the measurements. Figure adapted from [29].

In the absence of motion, the phase of the MR signal at position x_0 with the applied gradient $G_x(t)$ at time t after excitation is given by

$$\phi(x_0, t) = \gamma \int_0^t \left(G(\tau) \cdot x_0 + B_e(x_0, \tau) \right) d\tau + \Delta\omega_0(x_0)t + \phi_c(x_0, t) + \phi_{ss}(x_0, t) + \phi_{tr}(x_0), \qquad (2.19)$$

where $\Delta\omega_0$ is the susceptibility-induced off-resonance frequency, ϕ_c is the phase resulting from concomitant gradient fields, ϕ_{ss} is the phase from the slice selective gradient, and ϕ_{tr} is the phase due to the location of the transmit and receive coils. By using the assumption presented in equation (2.17), the phase can be presented as

$$\phi(x_0, t) = \hat{k}_x(t)x_0 + \phi_{B_0}(t) + \Delta\omega_0(x_0)t + \phi_c(x_0, t) + \phi_{ss}(x_0, t) + \phi_{tr}(x_0), \qquad (2.20)$$

where $\hat{k}_x$ is the actual k-space trajectory and ϕ_{B_0} is the B_0 eddy current phase. Note that equation (2.20) assumes all eddy currents from gradients in previous repetitions have decayed away by the start of the readout.
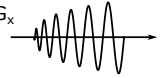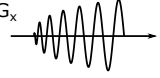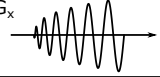
Figure 2.12: Overview of the four measurements used to measure the k-space trajectory with the corresponding phase terms. Figure adapted from the article by Robison et al. [29].

In order to measure $\hat{k}_x$ and ϕ_{B_0}, the four measurements are combined as shown in figure 2.12. By subtracting the phase of the two measurements at position x_0, where $\phi_I(t)$ has positive and $\phi_{II}(t)$ has negative gradient polarity, the unwanted field terms are removed

$$\phi_I(t) - \phi_{II}(t) = 2\hat{k}_x(t)x_0 + 2\phi_{B_0}(t) \equiv \phi_A(t). \tag{2.21}$$

This is also achieved for the phase of the measurements at position $-x_0$, where $\phi_{III}(t)$ has positive and $\phi_{IV}(t)$ has negative gradient polarity

$$\phi_{IV}(t) - \phi_{III}(t) = 2\hat{k}_x(t)x_0 - 2\phi_{B_0}(t) \equiv \phi_B(t). \tag{2.22}$$

Finally, $\phi_A(t)$ and $\phi_B(t)$ can be combined to get the k-space trajectory $\hat{k}_x(t)$ and the B_0 phase ϕ_{B_0} as follows

$$\hat{k}_x(t) = \frac{\phi_A(t) + \phi_B(t)}{4x_0} \quad \text{and} \quad \phi_{B_0}(t) = \frac{\phi_A(t) - \phi_B(t)}{4}. \tag{2.23}$$

One way to obtain the phase difference between two measurements is to divide the complex-valued signal from one measurement with the other. To get to equation (2.21), the signal from measurement I is divided by the signal from measurement II such that

$$\frac{S_I}{S_{II}} \propto \frac{e^{i\phi_I}}{e^{i\phi_{II}}} = e^{i(\phi_I - \phi_{II})} = e^{i\phi_A}, \tag{2.24}$$

and then the phase difference can be extracted by retrieving the phase of the result.

2.5 Linear time-invariant systems

This section will introduce the concept of LTI systems and present some of their main properties. The content is based on the description provided by Schetzen in *Linear Time-Invariant (LTI) Systems* [33], unless otherwise specified.

An illustration of a simple system is presented in figure 2.13, which produces the output $o(t)$ from the input $i(t)$. This response will be denoted as $i(t) \to o(t)$. For a *linear* system, if $i_1(t) \to o_1(t)$ and $i_2(t) \to o_2(t)$, this would mean that $C_1 i_1(t) + C_2 i_2(t) \to C_1 o_1(t) + C_2 o_2(t)$, where C_1 and C_2 are arbitrary complex constants. In other words, in a linear system, the response of a linear combination of inputs is the same linear combination of the individual responses of each input. If the system is also *time-invariant*, it has the property that the characteristics of the system is fixed in time. This means that if $i(t) \to o(t)$, then $i(t - \tau) \to o(t - \tau)$, where τ is an arbitrary time point.
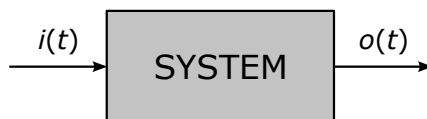
Figure 2.13: Illustration of a system with input $i(t)$ and output $o(t)$.

By combining these properties into a linear *and* time-invariant, or LTI, system, if the input is a linear combination of a waveform $f(t)$ and translates of that waveform $f(t - \tau)$

$$i(t) = \sum_n C_n f(t - \tau_n), \tag{2.25a}$$

then the system response is given by

$$o(t) = \sum_n C_n g(t - \tau_n), \tag{2.25b}$$

where $g(t)$ is the system response to $f(t)$.

Consider a segment of some arbitrary waveform $i(t)$, for example as illustrated in figure 2.14a. Any input waveform can be approximated by a piecewise constant curve $i_\epsilon(t)$, which consists of a sum of rectangles under the curve with width ϵ and height $i(n\epsilon)$ that are centered at time points $n\epsilon$

$$i_\epsilon(t) = \sum_{n\epsilon=-\infty}^{\infty} \epsilon\, i(n\epsilon)\delta_\epsilon(t - n\epsilon), \tag{2.26}$$

where $\delta_\epsilon(t)$ is defined as

$$\delta_\epsilon(t) = \begin{cases} \frac{1}{\epsilon} & \text{if } -\frac{\epsilon}{2} < t < \frac{\epsilon}{2}, \\ 0 & \text{otherwise}, \end{cases} \tag{2.27}$$

which has an area of one, and is illustrated in figure 2.14b.

From equations (2.25), the LTI system response to $i_\epsilon(t)$ is

$$o_\epsilon(t) = \sum_{n\epsilon=-\infty}^{\infty} \epsilon\, i(n\epsilon)h_\epsilon(t - n\epsilon), \tag{2.28}$$

where $h_\epsilon(t)$ is the system response to $\delta_\epsilon(t)$. To obtain the continuous output $o(t)$, let $\epsilon \to 0$, which yields

$$o(t) = \int_{-\infty}^{\infty} i(\tau)h(t - \tau)\mathrm{d}\tau, \tag{2.29}$$

where

$$h(t) = \lim_{\epsilon \to 0} h_\epsilon(t).$$
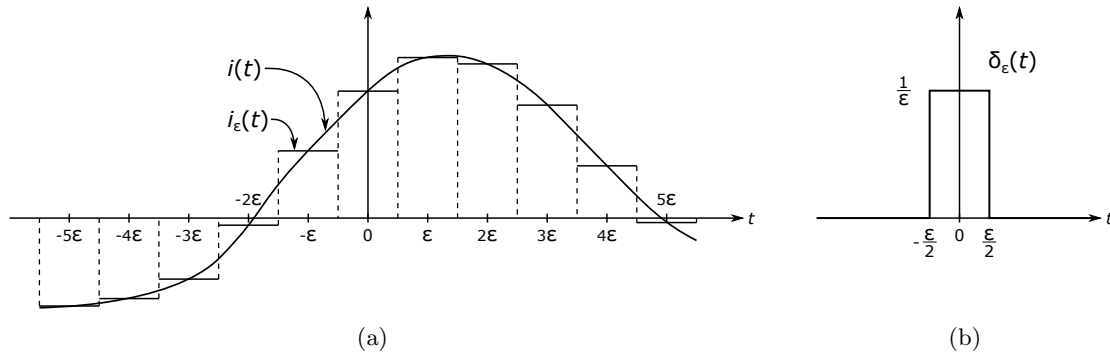
Figure 2.14: Illustration of (a) an arbitrary input waveform $i(t)$ and the corresponding step approximation $i_\epsilon(t)$, and (b) the function $\delta_\epsilon(t)$.

The integral in equation (2.29) is recognized as a *convolution integral*. Also, note that in the limit $\epsilon \to 0$, $\delta_\epsilon(t)$ is the dirac delta $\delta(t)$, also known as the impulse function. Therefore, as $h(t)$ is the system response to $\delta(t)$, it is known as the *impulse response function*.

If the impulse response function $h(t)$ of an LTI system is known, the output of the system can be determined for any input by taking the convolution of the input with $h(t)$. This means that the impulse response of an LTI system can be used to completely characterize the system. The convolution operation can be simplified by taking the Fourier transform since, in the frequency domain, a convolution becomes a simple product

$$O(\omega) = I(\omega) \cdot H(\omega), \tag{2.30}$$

where ω is the angular frequency, and $O(\omega)$, $I(\omega)$, and $H(\omega)$ are the Fourier transforms of $o(t)$, $i(t)$, and $h(t)$, respectively. Note that in system theory, the Fourier transform of the impulse response function $H(\omega)$ is known as the *transfer function*. Unfortunately, due to earlier conventions in the MR field, the term impulse response will be used for both $h(t)$ and $H(\omega)$ when describing an MR gradient system.

2.6   Gradient system characterization

In this project, the behavior of the gradient system will be characterized in order to predict the k-space trajectories of spiral sequences. This section will present the theory behind the method that will be used to determine the response of the gradient system.

By treating an MR gradient system as LTI, one may completely characterize it by determining its gradient impulse response function, or GIRF. This can be performed by measuring the actual gradient waveforms for a set of known input waveforms and calculating the GIRF based on the relation presented in equation (2.30). The method for gradient system characterization that will be presented in this section is based on the description by Vannesjo et al. [23].

Let $\hat{O}(\omega) = O(\omega) + \eta(\omega)$ denote the measured gradient output in the frequency domain, where $\eta(\omega)$ is the noise in the measurement with standard deviation $\sigma(\omega)$. Inserting this into equation (2.30), the resulting estimate of the GIRF in the frequency domain, denoted $H(\omega)$, is

$$\hat{H}(\omega) = \frac{\hat{O}(\omega)}{I(\omega)} = H(\omega) + \frac{\eta(\omega)}{I(\omega)}, \tag{2.31}$$

where $I(\omega)$ denotes the input gradient in the frequency domain. To get a good estimate of $H(\omega)$, $I(\omega)$ should ideally be large and equal for all frequencies of interest. As that corresponds to a dirac delta in the time domain and is impossible to generate, Vannesjo et al. proposes to use a series of short triangular pulses, where each pulse is described by

$$i(t) = \begin{cases} p \cdot (T - |t|), & |t| \leq T \\ 0, & |t| > T, \end{cases} \tag{2.32}$$

where T is half the duration of the triangular pulse, and p is the slope. Figure 2.15a illustrates several such triangular pulses with the same slope but with different lengths, and figure 2.15b illustrates the frequency composition of the triangle pulses. The reason for using several pulses is that the Fourier transform of each triangle has zeros, as can be seen in figure 2.15b, which amounts to blind spots at frequencies

$$\omega|_{I=0} = \frac{2\pi n}{T}, \quad n = \pm 1, 2, 3... \tag{2.33}$$

Thus, by including several pulses of different lengths, one obtains complementary response information. To combine the information from the separate input and output measurements, the least-squares estimate is calculated for $\hat{H}(\omega)$ by

$$\hat{H}(\omega) = \frac{\sum_j I_j^*(\omega) \cdot \hat{O}_j(\omega)}{\sum_j |I_j(\omega)|^2} = H(\omega) + \frac{\sum_j I_j^*(\omega) \cdot \hat{\eta}(\omega)}{\sum_j |I_j(\omega)|^2}, \tag{2.34}$$

where $I^*(\omega)$ is the complex conjugate of $I(\omega)$, and j counts the input gradients.

Until now, the method only determines the self-response of the gradient field components. It can easily be extended to include cross-responses between other undesired field components, such as changes in the static magnetic field due to an applied linear field gradient. To do this, the measured outputs must be expanded to a suitable set of spatial basis functions such as the spherical harmonics, where each harmonic makes up a separate output channel m. Also, each controlled input of the system makes up an input channel l, which, for a gradient system, usually consists of the x-, y-, and z-gradient channels. For each combination of input and output channels, separate impulse responses can be determined. This gives the following complete description

$$O_m(\omega) = \sum_l I_l(\omega) \cdot H_{l,m}(\omega), \tag{2.35a}$$

$$\hat{H}_{l,m}(\omega) = \frac{\sum_j I_{l,j}^*(\omega) \cdot \hat{O}_{l,m,j}(\omega)}{\sum_j |I_{l,j}(\omega)|^2}. \tag{2.35b}$$
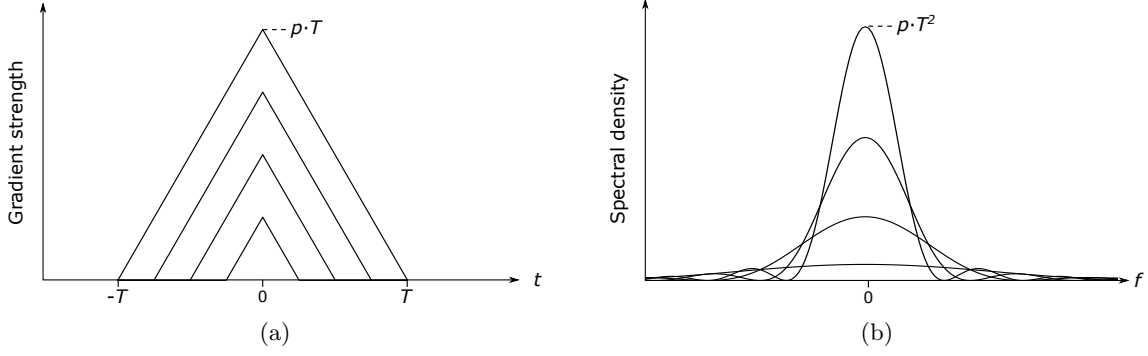
Figure 2.15: (a) Triangular input pulses with slope p, where the longest pulse has duration $2T$, and (b) the frequency composition of the same pulses.

Note that the number of available output channels is limited by the measurement technique.

The measured gradient waveform in output channel m, $\hat{o}_m(t)$ can be determined based on k-space trajectory measurements, for example as described in section 2.4, by using the relation

$$\hat{o}_m(t) = \frac{1}{\gamma} \frac{\mathrm{d}\hat{k}_m(t)}{\mathrm{d}t}, \tag{2.36}$$

where γ is the gyromagnetic ratio of the hydrogen-nuclei, and $\hat{k}_m(t)$ is the time-varying phase accumulated due to fields of the respective output channel. For the technique presented in section 2.4, only the 0th and 1st order field responses is measured, such that $m = 0, x, y, z$. For better readability, the 0th order phase ($\hat{k}_0$) and the 1st order phases ($\hat{k}_{x,y,z}$) will be referred to by the notations used in section 2.4, which are ϕ_{B_0} and $\hat{k}_{x,y,z}$ respectively. The corresponding outputs are $\hat{o}_0 = B_{0e}$ and $\hat{o}_{x,y,z} = \hat{G}_{x,y,z}$. Furthermore, the only cross-responses available with the technique presented in section 2.4 are between the input channel and the 0th order response. As a result, the GIRFs that can be determined with this technique is

$$\hat{H}_{xx}(\omega),\ \hat{H}_{x0}(\omega),\ \hat{H}_{yy}(\omega),\ \hat{H}_{y0}(\omega),\ \hat{H}_{zz}(\omega),\ \text{and}\ \hat{H}_{z0}(\omega).$$

After determining the GIRF, it can be used to predict the actual shapes of planned gradient waveforms. These predictions can be used during image reconstruction to correct for deviations of the k-space trajectories and has been shown to improve image quality [34]. Having defined the gradient waveform in each of the input channels $i_l(t)$, the output waveforms $\hat{o}_m(t)$ can be predicted as follows:

$$\hat{o}_m(t) = \sum_l \int_{-\infty}^{\infty} i_l(t) \cdot \hat{h}_{l,m}(t-\tau)\mathrm{d}\tau \quad \xleftrightarrow{FT} \quad \hat{O}_m(\omega) = \sum_l I_l(\omega) \cdot \hat{H}_{l,m}(\omega). \tag{2.37}$$

2.7   Parallel imaging

This project will use parallel imaging to achieve higher resolutions and reduce artifacts from phase accumulation in the signal. This section will introduce the concept behind parallel imaging in general and present the theory behind SENSE, which is the specific method used to reconstruct the images in this project.

Current MR scanners operate at the limits of potential imaging speed because of the hardware and safety restrictions caused by the rapidly switching of linear field gradients. However, a further increase in imaging speed can be achieved with parallel imaging, which utilizes the spatial information from several receiver coils as spatial encoding. In modern MR scanners, receiver coil arrays typically consist of 32 or 64 individual coils. The signal intensity in a receiver coil decreases with the distance to the source so that the signal can be located based on the relative signal strength in the coils, known as the coil sensitivity c. See figure 2.16a for a simple illustration of how this is used to determine the position of a voxel.

Using parallel imaging as spatial encoding allows for partial sampling, or *undersampling*, of k-space while maintaining full spatial resolution. The amount of undersampling is described by the reduction factor R, which usually ranges from 2-6. Typically the undersampling is performed by reducing the sampling density in k-space, which amounts to reducing the FOV, as illustrated in figure 2.16b for a simple cartesian sampling scheme. Without the additional spatial information from parallel imaging, a reduced FOV would cause aliasing artifacts. If the maximal k-value had been reduced instead, the resolution in the final image would be reduced which is not desirable. Several image reconstruction schemes for parallel imaging have been developed, with some of the most known being SMASH [35], GRAPPA [36], and SENSE [37]. This section will present SENSE, which is a shorthand notation for SENSitivity Encoding.

(a)   (b)
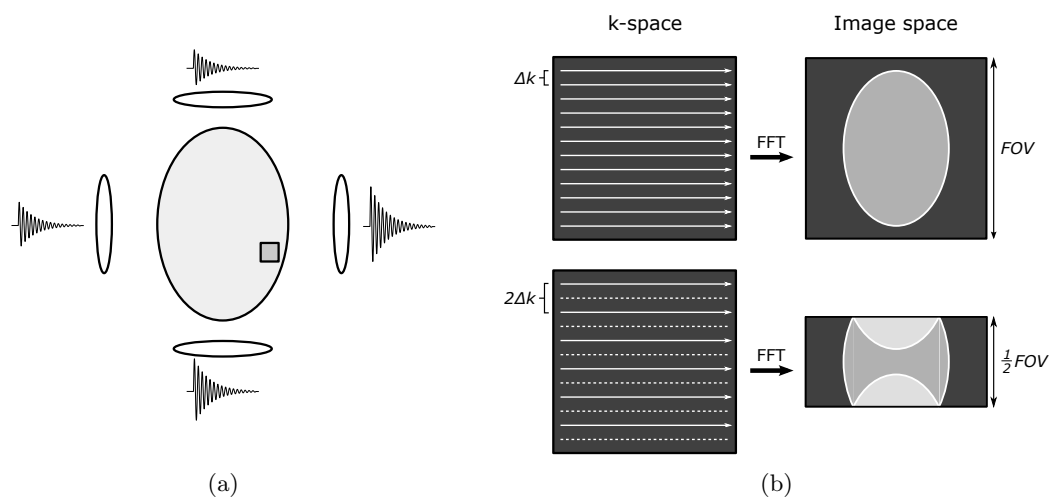
Figure 2.16: Parallel imaging concepts. (a) The signal from the gray voxel will have different intensities in the four coils around the subject, depending on the distance. (b) Undersampling in k-space with $R = 2$. By doubling the distance between the readout lines the FOV is reduced by half, introducing aliasing in the reconstructed image without parallel imaging.

2.7.1   Sensitivity encoding (SENSE)

This section will first describe SENSE in terms of sampling on a cartesian grid in k-space, which amounts to a simple unfolding of the signal in image space. Then, it will provide a more general, albeit less intuitive, description which allows for an arbitrary k-space trajectory in two dimensions, and finally, how B_0-correction is performed with SENSE reconstruction.

Cartesian k-space trajectories

In cartesian sampling, each pixel in the image will periodically repeat itself with a spacing determined by the distribution of data in k-space. In a fully sampled k-space, this repetition occurs only once within the FOV. By undersampling with a factor R, by sampling every Rth line in k-space, the pixels will repeat R times along the undersampled direction in the reduced FOV. This is illustrated in figure 2.17. With N_c coils, one will get N_c aliased images where the pixels are weighed by the coil sensitivity c at the corresponding position in the full FOV. The signal intensity in position (x, y) in the image from coil γ is given by

$$I_\gamma(x, y) = c_\gamma(x, y_1)\rho(x, y_1) + c_\gamma(x, y_2)\rho(x, y_2) + ... + c_\gamma(x, y_R)\rho(x, y_R), \tag{2.38}$$

where ρ describes the true signal intensities in the R superimposed pixels when y is the undersampled direction. This can be rewritten as

$$I_\gamma = \sum_{l=1}^{R} c_{kl}\rho_l \tag{2.39}$$

where the index l counts from 1 to R, specifying the location of the superimposed pixels.

By including all N_c coils, a set of linear equations can be constructed per pixel, described by the following matrix equation

$$\vec{I} = C\vec{\rho}, \tag{2.40}$$

where $\vec{I}$ is a column vector with N_c elements describing the intensity of the same voxel in the reduced FOV in different coils, C is the coil sensitivity matrix with dimensions $N_c \times$ R, and $\vec{\rho}$ is a column vector with R elements describing the intensities of the R unfolded pixels in the full FOV.

To reconstruct the full FOV image, the vector $\vec{\rho}$ must be determined for all pixels in the reduced FOV. This can be performed by using a generalized inverse of the sensitivity matrix

$$\vec{\rho} = (C^H C)^{-1} C^H \vec{I}, \tag{2.41}$$

where the superscripts H and -1 denote the complex-conjugate and inverse, respectively. Equation (2.41) can be solved as long as R $< N_c$. Note that equation (2.41) does not account for noise correlation, which may be an issue if the coils are not entirely decoupled. A detailed description of how to account for this is provided by Pruessmann et al. [37].
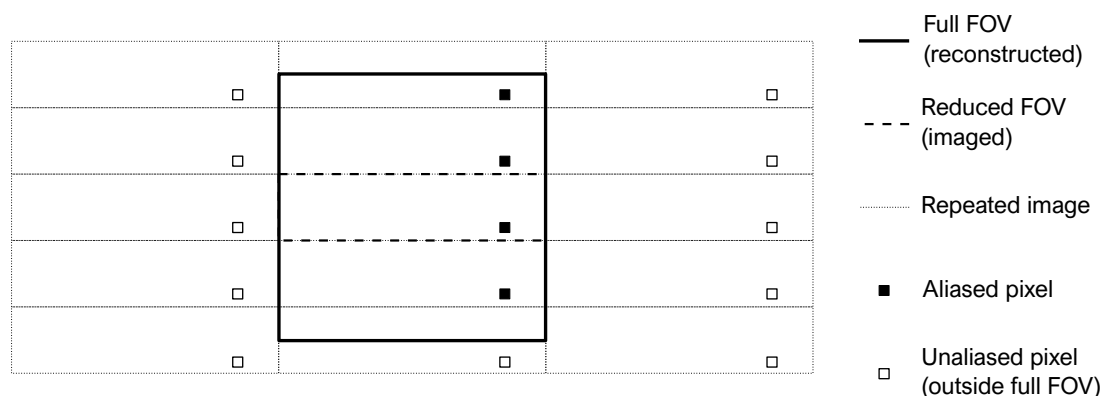
Figure 2.17: Aliasing in cartesian sampling with a reduction factor of R = 4, where the undersampling is performed by reducing the number of k-space lines. The reduced FOV which is being sampled is repeated in both directions. The four black pixels all contribute to the signal that is measured in the pixel in the reduced FOV, and the goal of cartesian SENSE is to unfold the signal into the four separate pixels in the full FOV.

Arbitrary k-space trajectories

With non-cartesian k-space trajectories, the situation is more complicated since the aliasing that occurs due to undersampling is complex and does not allow for a simple unfolding in the image. Therefore, a different method is required to reconstruct undersampled data where the k-space is not sampled in a cartesian manner.

Consider an imaging experiment with N_c coils where the whole subject is located within the volume V. After demodulating the carrier signal, the received signal in coil number γ is given by

$$S_\gamma(t) = \int_V m(\vec{r})e^{-i\vec{k}(t)\cdot\vec{r}}c_\gamma(\vec{r})dV, \tag{2.42}$$

where t is the sampling time, $m(\vec{r})$ is the magnetization at position $\vec{r}$, and $\vec{k}(t)$ is the k-space position at time t, and $c_\gamma(\vec{r})$ is the coil sensitivity at position $\vec{r}$.

Assume that the image to be reconstructed has $N \times N$ pixels and that the total number of sampling points in k-space is N_κ. Equation (2.42) can then be discretized in space and time to yield

$$s_{(\gamma,\tau)} = \sum_{\rho=1}^{N^2} E_{(\gamma,\tau),\rho}m_\rho, \qquad \begin{array}{l} \gamma = 1, ..., N_c \\ \tau = 1, ..., N_\kappa \end{array} \tag{2.43}$$

where $m_\rho = m(\vec{r}_\rho)$, and the indices τ and ρ count sampling time points and image voxels, respectively. E denotes the encoding matrix with elements

$$E_{(\gamma,\tau),\rho} = c_\gamma(\vec{r}_\rho)e^{-i\vec{k}_\tau\cdot\vec{r}_\rho}. \tag{2.44}$$

By placing the measured data from all coils in a vector $\vec{s}$ of size $N_c \times N_\kappa$ and the reconstructed image values in a vector $\vec{m}$ of size N^2, equation (2.43) can be rewritten as a matrix equation

$$\vec{s} = E\vec{m}, \tag{2.45}$$

where the encoding matrix E has dimensions $(N_c \times N_\kappa) \times N^2$. Equation (2.45) may be solved for $\vec{m}$ in order to reconstruct the image by using a generalized inverse

$$\vec{m} = (E^H E)^{-1}E^H\vec{s}. \tag{2.46}$$

However, the right-hand side of equation (2.46) is too large to invert, and it is more efficient to solve the system iteratively using the conjugate-gradient (CG) method [9, 38]. By rearranging the equation as

$$(E^H E)\vec{m} = E^H\vec{s}, \tag{2.47}$$

fast Fourier transform (FFT) with forward and reverse gridding operations can be combined with the CG iteration loops to increase reconstruction speed. For a more in-depth description of this, see the article by Pruessmann et al. [9].

B$_0$-correction

B$_0$-correction during SENSE reconstruction can be performed with an extended signal model if a map of the static inhomogeneity is acquired, for example with the method described in section 2.1.5. Since an offset in B$_0$ causes an offset in resonance frequency of the spins, it will cause an accumulation of phase in the acquired signal over time. By introducing a resonance offset of $\Delta\omega_0(\vec{r}) = \gamma\Delta B_0(\vec{r})$, the signal in equation (2.42) can be expressed as

$$S_\gamma(t) = \int_V m(\vec{r})c_\gamma(\vec{r})e^{-i\vec{k}(t)\cdot\vec{r}-i\Delta\omega_0(\vec{r})t}dV. \tag{2.48}$$

In order to discretize equation (2.48) and end up with the same expression as in equation (2.43), the encoding matrix E now reads

$$E_{(\gamma,\tau),\rho} = c_\gamma(\vec{r}_\rho)e^{-i\vec{k}_\tau\cdot\vec{r}_\rho-i(\Delta\omega_0)_\rho t_\tau}, \tag{2.49}$$

where $(\Delta\omega_0)_\rho = \Delta\omega_0(\vec{r}_\rho)$. By substituting the new encoding matrix into equation (2.47), the reconstruction can still be performed iteratively with the CG method.

3 Methods

All measurements for the work presented in this report were acquired on a Siemens MAGNETOM Terra 7T MR scanner at St. Olavs hospital in Trondheim, Norway. The work consists of three parts in the following order: First, the gradient system was characterized by calculating a GIRF. Second, spiral trajectory measurements were performed and compared to GIRF predictions. Third, image reconstruction was performed for spiral imaging with k-space trajectory correction provided by GIRF predictions.

3.1 Gradient system characterization

The GIRF was determined with the method presented in section 2.6. In total, seven triangular pulses with a slew rate of 190 T/m/s and time-to-peak ranging from 20-140 μs at 20 μs increments were used to calculate the system response.

To measure the triangular pulses, the method described in section 2.4 was used to determine the k-space trajectories, from which the gradient waveforms can be found. First, the data acquisition was performed on a spherical phantom with a one-channel head-coil. The measurements included 15 gradient waveforms in all three directions, consisting of 7 pairs with opposite polarities plus one reference acquisition with no gradient. All measurements were repeated eight times for averaging purposes. The acquisition time was TA = 40.96 ms and began 4.52 ms after RF excitation, and the triangular pulses were centered at 1/32 of the acquisition. The total scan time for all measurements in one direction was 720 s so that all necessary data for GIRF calculation was acquired in 36 minutes. The distance from the isocenter to the slices used for further processing was 5.1 cm, and the slice thickness was 1 mm. Secondly, the acquired data was further processed in MATLAB version R2021b (9.11.0), and the code is shown in appendix A.1. The mapVBVD-function from the toolbox FID-A (version 1.2) was used to import the Siemens raw data into MATLAB. The actual k-space trajectories and the 0th-order phase ϕ_{B_0} of the measurements were calculated according to equations (2.21-2.23) for all applied gradients and averaged over the eight repeated measurements. Finally, the actual gradients and B_{0e} were calculated according to equation (2.36).

The calculation yielded seven triangle pulses with corresponding B_{0e}-responses along the x-, y-, and z-direction, which were used as output in the GIRF calculation. A least-square estimate of the GIRF was calculated according to equation (2.35) using the open-source GIRF-package provided with the paper by Vannesjo et al. [23]. In the end, a raised cosine filter with full width at half maximum (FWHM) of 60 kHz and a roll-off factor of 1/4 was applied to the GIRF.

A similar procedure was used to determine the GIRF with a 32-channel head-coil with the same phantom and sequences. However, the center of the phantom was not centered at the isocenter, and as a result, some of the slices 5.1 cm away from the isocenter contained only a small part of the phantom. This yielded a low SNR and the slices located 3.4 cm away from the isocenter were used for further processing off-site instead. The GIRF calculation was performed using the same method as described for the one-channel

coil. In addition to averaging over the eight repeated measurements, the data were also averaged over the 32 receive channels. Due to the nature of the k-space trajectory calculation, no additional step was needed to remove the receive coil-specific phase shifts in the data. After calculating the gradient waveforms and corresponding B_{e0}-responses, the GIRF was calculated as described in the previous paragraph.

3.2   Spiral trajectory measurements

Spiral sequences with different sequence parameters as described in table 3.1 were designed, and the nominal gradient waveforms were calculated based on the approach first described by Pipe and Zwart [39]. The in-plane resolution ranged from $0.74 - 2.40$ mm, and acquisition acceleration by parallel imaging was used for the higher resolutions with acceleration factors $R = 2 - 4$. An example trajectory is presented in figure 3.1a along with the corresponding gradient waveforms in figure 3.1b. The frequency composition of the gradients of a selection of the spiral trajectories is presented in figure 3.2. Then, k-space trajectory measurements of all the spiral sequences in table 3.1 were performed on a spherical phantom, with repetition time TR = 4000 ms and FA = 90°, with eight averages. Some measurements were performed with a one-channel head coil and others with a 32-channel head coil, as specified in table 3.1. The distance from the isocenter to the slices used for further processing was 5.1 cm for the one-channel receive coil and 3.4 cm for the 32-channel receive coil, and the thickness was 1 mm for both coil setups. Note that the values of TR and slice thickness in table 3.1 refer to the sequence parameters for the spiral image acquisition and thus differ from the values used during k-space trajectory measurements. The measurements and calculations to retrieve the true k-space trajectories and ϕ_{B_0} were performed as described in section 2.4, and the gradients and B_{0e} were calculated according to equation (2.36).

Predictions were made for the spiral gradients using the GIRF-package [23] along with the previously acquired GIRF, and comparisons were made between the measured, nominal, and predicted k-space trajectories, gradient waveforms, and B_{0e}. There was observed a time delay between the measured and nominal waveforms, which was determined numerically by minimizing the root mean square (RMS) error as a function of time shift and corrected for before comparing the waveforms.

Table 3.1: Imaging parameters of the acquired spiral trajectories in this work. The acceleration factor R describes the undersampling during image acquisition.

FOV (mm)	Slice (mm)	R	Res (mm)	TE (ms)	TR (ms)	T_{RO} (ms)	Coil setup
140	2.0	1	2.00	2.1	2000	31.3	1ch
192	2.0	1	2.40	2.4	2000	32.7	1ch, 32ch
192	2.0	2	1.39	2.5	2000	37.3	32ch
192	2.0	3	1.00	2.5	2000	39.3	32ch
164	2.0	1	2.00	2.4	2000	36.7	32ch
164	2.0	2	1.21	2.5	2000	39.5	32ch
140	2.0	1	1.71	2.4	2000	37.8	32ch
140	2.0	2	1.08	2.5	2000	40.0	32ch
140	2.0	4	0.74	2.7	2000	40.5	32ch

3.3   Spiral imaging

3.3.1   Data acquisition

Image data of a spherical water-filled phantom and a healthy volunteer was acquired with a 32-channel head receive-coil. Written informed consent was obtained from the volunteer before imaging.

Single-shot spiral imaging was performed with the imaging parameters presented for the rows with the

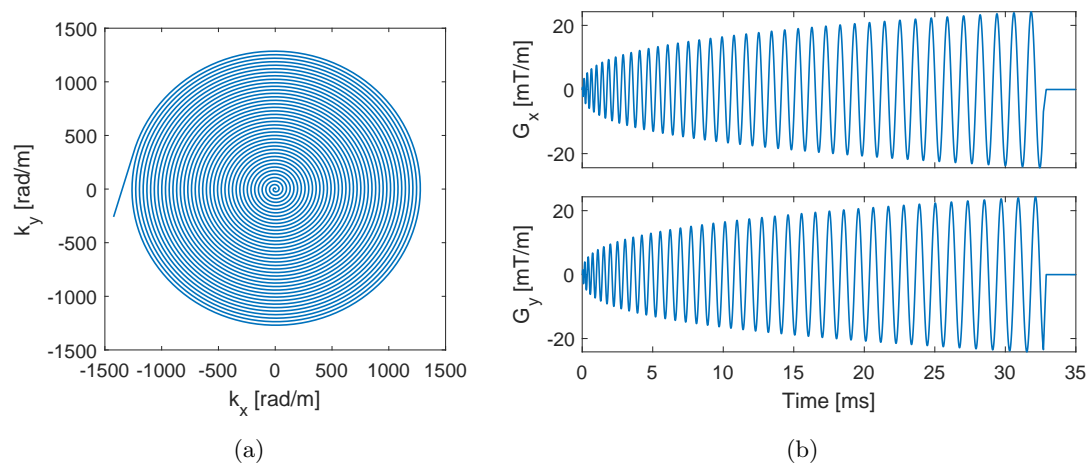(a)   (b)

Figure 3.1: A representative input spiral sequence. (a) Nominal k-space sampling trajectories. (b) Input readout gradients.
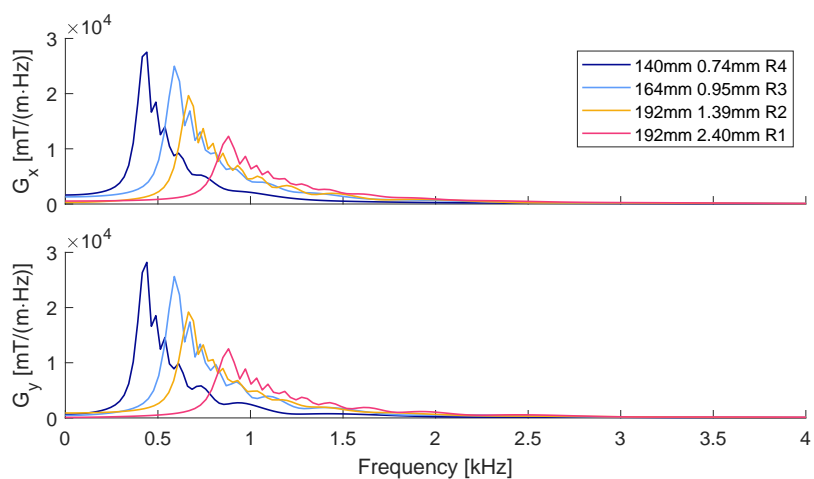

Figure 3.2: Frequency spectra of a selection of spiral input gradients.

32-channel coil in table 3.1, with resolutions ranging from $0.74 - 2.40$ mm and acceleration factors up to R = 4. The spiral trajectories were the same as used during spiral trajectory measurements as described in the previous section, and they were designed with the approach described by Pipe and Zwart [39] to get the desired k-space coverage. Each sequence consisted of 20 repeated measurements of one slice at the isocenter in the transverse orientation. The slice thickness was 2 mm, and the FOV ranged from $140 - 192$ mm, with TR = 2000 ms. The readout length (T_{RO}) and TE varied with trajectory, and the TE was kept as short as possible for all measurements.

For correction of static inhomogeneities in B_0, field map measurements were acquired from two gradient-echo images with different TEs. For the phantom measurements, the following parameters were used: FOV = 192 mm, resolution = 2.0 mm isotropic, slice thickness = 2.0 mm, TE1/TE2 = 4.08/5.10 ms, TR = 200 ms. For the in-vivo measurements, the FOV was increased to 220 mm, keeping the other parameters the same as for the phantom measurement. The field maps were calculated from the phase difference between the voxels in the two images with different TEs according to equation (2.11). The gradient echo acquisitions with the shortest TE were used to calculate the coil sensitivity profiles for the 32-channel head receive coil, which was later used for iterative SENSE reconstruction.

3.3.2   Image reconstruction

Image reconstruction was performed with the open-source MR imaging package *MRIReco* [40], which is written in Julia [41], that offers a high-performance and flexible reconstruction framework. It offers standard cartesian and non-cartesian reconstruction in addition to iterative SENSE-reconstruction, built-in methods for calculating coil sensitivity maps, and B_0-correction. All images in this work were reconstructed with the iterative SENSE scheme in MRIReco which is based on the approach described by Pruessmann et al. [9], using sensitivity profiles based on the ESPIRiT approach [42]. The built-in B_0-correction in MRIReco was used with the field maps calculated from the gradient-echo images. The version of Julia used in this work was 1.7.3.

Each acquired image was reconstructed with nominal, GIRF-predicted, and measured k-space trajectories. The images were reconstructed with and without time shift of the nominal trajectories to investigate the effect of a simple delay-correction. The time shift was determined from the spiral trajectory measurements described in section 3.2. To account for the spatially uniform phase modulations due to eddy current effects the imaging data was demodulated by the predicted or measured ϕ_{B_0} before image reconstruction. The GIRF-predicted trajectories were reconstructed both with and without ϕ_{B_0}-correction to investigate the effects on the reconstructed image. The ϕ_{B_0} was assumed to be zero throughout the acquisition for both nominal cases. To summarize, the following five trajectories were used to reconstruct each spiral image: measured (used as reference), GIRF-predicted with ϕ_{B_0}-correction, GIRF-predicted without ϕ_{B_0}-correction, nominal delay-corrected, and nominal without delay-correction.

As mentioned for the spiral trajectory measurements, the positioning device for the phantom was not tailored for the 32-channel head coil, and the center of the phantom was located above the isocenter. More accurately it was displaced along the anterior-posterior axis, towards the anterior side. This yielded a wrap-around of the signal over to the posterior side of the reconstructed image since the edge of the phantom was outside the FOV. To avoid wrap-around, a linear phase was added to the image data along the phase encoding direction before reconstruction so that the image was shifted 1.0 cm in the posterior direction. This was done for both the gradient echo sequence and the spiral sequences.

The FOVs smaller than 192 mm were too small to encapsulate the entire phantom during phantom measurements, even when shifting the image as described in the paragraph above. To avoid additional image artifacts due to a reduced FOV all phantom images were reconstructed onto a FOV of 192 mm. This resulted in an increase of undersampling with a factor of 1.2 and 1.4 for the images with FOVs of 164 and 140 mm compared to the values presented in table 3.1, respectively.

For the in vivo measurements, a phase shift was added in the phase encoding direction that shifted the images 7 mm towards the posterior side before reconstruction. This was performed for all spiral sequences

and the gradient echo sequence. All in vivo images were reconstructed onto a FOV of 220 mm, resulting in increased R-values with a factor of 1.1, 1.3, and 1.6 for the images with FOVs of 192, 164, and 140 mm, respectively.

3.4 Handling of time axes

For the GIRF predictions to correctly predict the time delay of the system, the handling of the time axis needs to be consistent during GIRF calculation and gradient predictions. This can be done in several ways, but figure 3.3 shows how consistent time axes have been achieved in the work presented in this report. As all the acquired data was discrete in time, the time point of the measurements has been chosen to be in the center of the time intervals with widths of Δt.

The system input was discretized into time steps of 10 µs with the initial time point being located at 5 µs, and the measurements had a time step of 2.5 µs with the initial point at 1.25 µs. As the gradients were found by differentiation of the measured k-space trajectories, the time axes of the calculated gradients were shifted with $\Delta t/2$. As the GIRF calculation needed the time axes of the input and output to have the same size, the input triangles were gridded onto the same time axis as the output gradients.
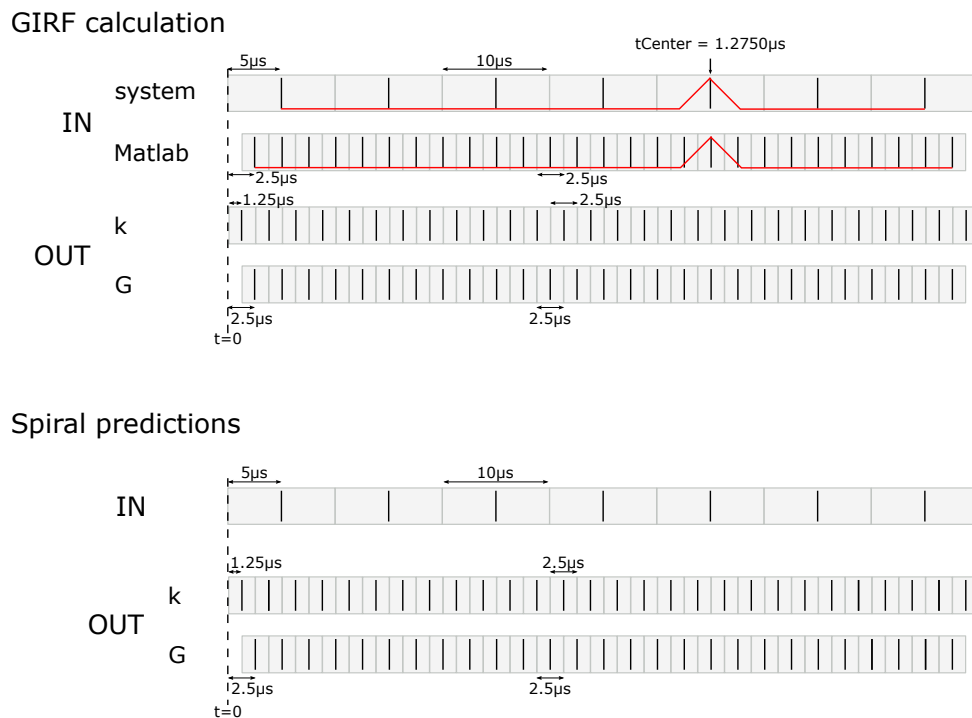
Figure 3.3: Handling of time axes. The gray boxes visualize the time intervals of the discrete measurements, and the lines depict where the data points are chosen to be placed within the time intervals.

4 Results

4.1 Gradient system characterization

The k-space trajectories for the largest triangle pulse is shown in figure 4.1 along with ϕ_{B_0}, measured with the one-channel head-coil. The ϕ_{B_0}-data has been filtered with a raised cosine filter with FWHM of 60 kHz and a roll-off factor of 1/4 to remove noise. The figures to the left show the entire acquisition, while the figures to the right are zoomed in around the time the triangle pulses were applied. Upon applying the triangle pulses, the k-space position changes in a step-wise fashion as expected. The nominal k-space trajectory has a small delay during the triangle pulse compared to the measured trajectory. After the gradient pulse, the measured trajectory oscillates about the constant nominal k-space value, and this behavior is observed in all three directions. Towards the end of the acquisition, the k-space position seems to diverge from the nominal value. The rate and direction depend on the strength and direction of the applied gradient.

There was induced a ϕ_{B_0} due to the applied linear gradients, or else the bottom row in figure 4.1 would have been zero for all times. Note that the direction of the phases indicates the direction of the applied gradients that induced the phase, as a phase has no direction in itself. During the application of the gradient, the largest phase is seen along the y- and z-direction of the scanner. After the gradient has been applied, a distinct oscillation of the phase is observed in the z-direction. The oscillations are smaller along the x- and y-directions, and there is observed a drift of the phase along y. Note that the results shown in figure 4.1 are only for the largest triangle pulse but that all pulses exhibit the same behavior.

The gradient output of the triangle pulses is shown in figure 4.2 along with the B_{0e} response for the measurements of the largest triangle gradient pulse obtained with the one-channel head coil. The gradient and B_{0e} data have been filtered with a raised cosine filter with FWHM of 60 kHz and a roll-off factor of 1/4 to remove noise. The figures to the left show the gradient and field for the whole acquisition, and the figures to the right show the details around the time the triangle pulses were applied. Just as for the k-space trajectories, the nominal gradient has a slight lag compared to the measured gradients. The peaks of the measured gradients are smoother than the nominal, which results in a lower maximum amplitude. The value of the measured maximum varies between the x-, y-, and z-directions. After the applied gradient, there is observed a slight oscillation in the measured gradient in all three directions, where the amplitude decreases with time. The measured eddy current field B_{0e} shows similar properties as the ϕ_{B_0}, with the largest values being observed during the application of the gradient followed by an oscillation that is the largest along the z-direction. The strength of the induced field depends on the gradient strength, but the evolution in time is similar for all triangle input pulses.

Figure 4.1: Measured k (upper row) and ϕ_{B_0} (lower row) of the largest triangle gradient with a maximum amplitude of 26.6 mT/m. The column to the left shows the entire acquisition, while the column to the right displays the data for a short time interval around the application of the gradient.
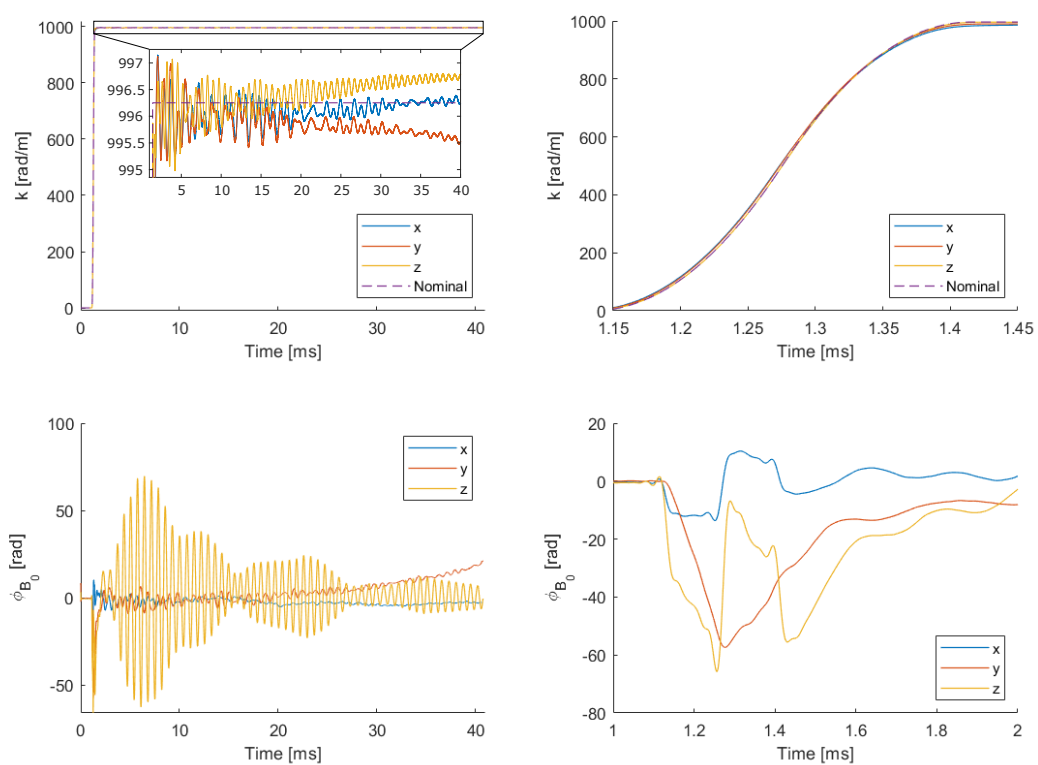
Figure 4.2: Measured G (upper row) and B_{0e} (lower row) of the largest triangle gradient with a maximum amplitude of 26.6 mT/m. The column to the left shows the entire acquisition, while the column to the right displays the data for a short time interval around the application of the gradient.
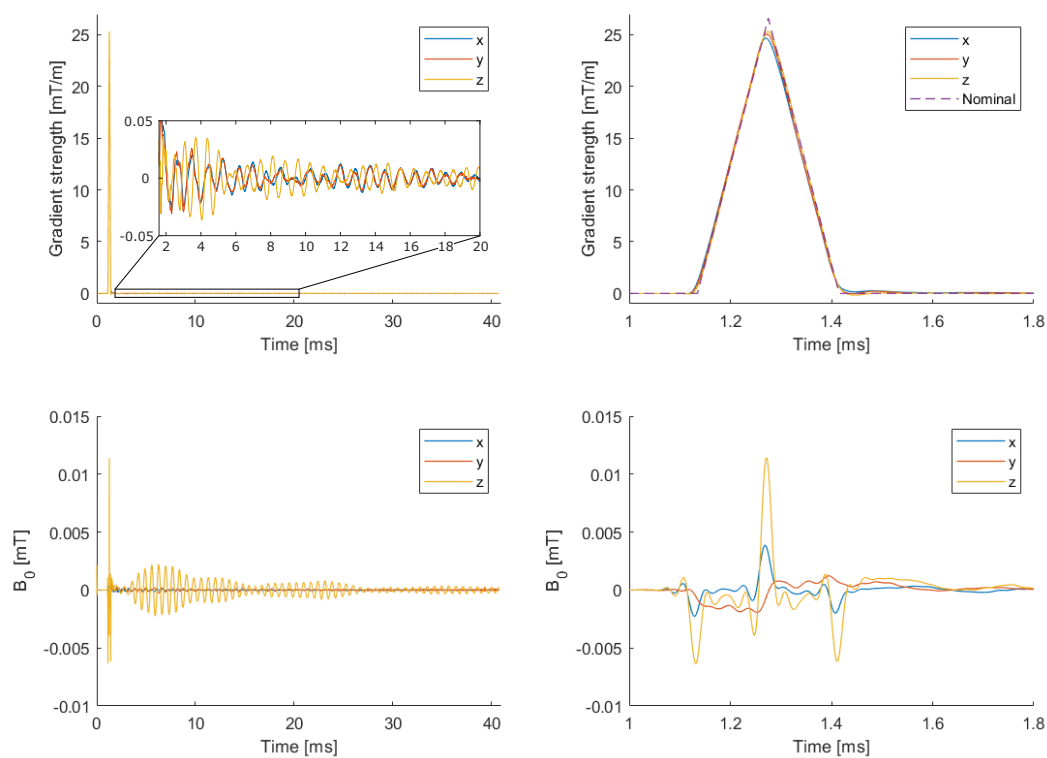
The magnitude and phase plots of the GIRF describing the self-response of the system with a one-channel head-coil are shown in figure 4.3. The GIRF has low-pass characteristics for all three directions, with FWHM of approximately 30-40 kHz, where the response of the z-direction is the broadest. It tapers off towards zero around ± 40 kHz, which is mostly due to the applied low-pass filter. For frequencies below 15 kHz the y- and z-responses are approximately the same, while the x-response is slightly lower and more narrow. For frequencies above 15 kHz, the GIRF is noisier as the power of the input gradients is low. Here, the z-response is the highest while the x- and y-response are about the same. For some frequencies, peaks can be observed in the GIRF. This is seen more clearly in the graph in the upper right of figure 4.3, which displays the magnitude of the response for low frequencies. Here it can be seen that the x- and y-response follow each other's shapes more closely than the z-directions, as their peaks appear on different frequencies compared to the z-response. The x- and y-responses exhibit a peak at 0.562 kHz, and dips at 1.099 kHz, 1.172 kHz, and 1.343 kHz. The z-response exhibits peaks at 1.343 kHz and 1.636 kHz and has a dip at 1.367 kHz. For higher frequencies, there is also a broader peak around 12 kHz. More specifically the peaks are located at 11.79 kHz, 11.99 kHz, and 12.40 kHz for the x-, y-, and z-responses, respectively.

The phase response has a positive slope for all gradient channels at frequencies above 15 kHz. For frequencies below 15 kHz, there is a small positive slope for the x-direction, no slope for the y-direction, and a slightly negative slope for the z-direction. Note that for both ranges, the slope shows a linear behavior. A slope in the phase indicates a delay of the gradients, which was indeed observed in the gradient measurements shown in figure 4.2. The slope of the phase response of the z-gradient is less steep than the x- and y-gradient for all frequencies, indicating a smaller delay. The slightly negative slope of the z-gradient for lower frequencies indicates that the B_{0e} response is seen before the onset of the input gradients, although only barely. For frequencies up to $\sim$1.5 kHz, the x- and y-gradient exhibit approximately the same slope. For higher frequencies, the x-gradient has a steeper slope and thus larger delays compared to the y-gradient. The phase response also has peaks and dips for lower frequencies that seem to align with the ones observed in the magnitude response, albeit with opposite polarity. For the x- and y-response there is a dip at 0.562 kHz, and peaks at 1.099 kHz, 1.172 kHz, and 1.367 kHz. The z-response has a narrow dip at 1.343 kHz, a broader one at 1.685 kHz, and a smaller one at 1.953 kHz, as well as a peak at 1.538 kHz.

The parts of the GIRF that describe the cross responses between the 0th-order field (B_{0e}) and the 1st-order field (linear gradients) are shown in figure 4.4, scaled to the percent of the input. To compare field responses with different spatial orders, such as B_{0e} and linear field gradients, the responses were compared on the surface of a sphere with a radius of 10 cm, centered at gradient isocenter [23]. This means that a gradient of 10 mT/m will amount to a B_{0e} of 1 mT. The same shape can be observed for the responses at all gradient channels, with almost zero response for low frequencies and then an increase for frequencies up to $\sim$25 kHz before it falls off to zero at 40 kHz. The response in the y-direction is the weakest, and it is difficult to determine the frequency with the highest response due to the noise. The x-direction shows a higher response at high frequencies, with a maximum of 4% at 27.3 kHz. The largest response, and thus induced magnetic field, is seen in the z-direction where the maximum response is 13% at 26.7 kHz. There is also a distinct peak in the lower frequency range for the z-response, located at 1.44 kHz, which is not observed in any other direction. This frequency matches the main frequency component of the measured B_{0e}-field along the z-direction shown in the lower left of figure 4.2.

The phase of the cross-response GIRF is shown before unwrapping due to the large jumps in phase caused by low signal. The phase for low frequencies (≤ 5 kHz) is very noisy, which is due to the low magnitude in this region. The less noisy parts, such as the phases of the x- and z-responses for frequencies above 5 kHz, shows a linearly increasing behavior for frequencies above 15 kHz, and the z-direction has a flat region with some peaks for frequencies lower than 15 kHz. It is also likely that the x- and y- phase responses are zero for frequencies close to zero, although the lack of unwrapping makes it appear different. The phase of the x-response exhibit a slightly more steep behavior than the z-direction. The cross-response in the y-direction is weak and noisy, making the phase response hard to interpret.

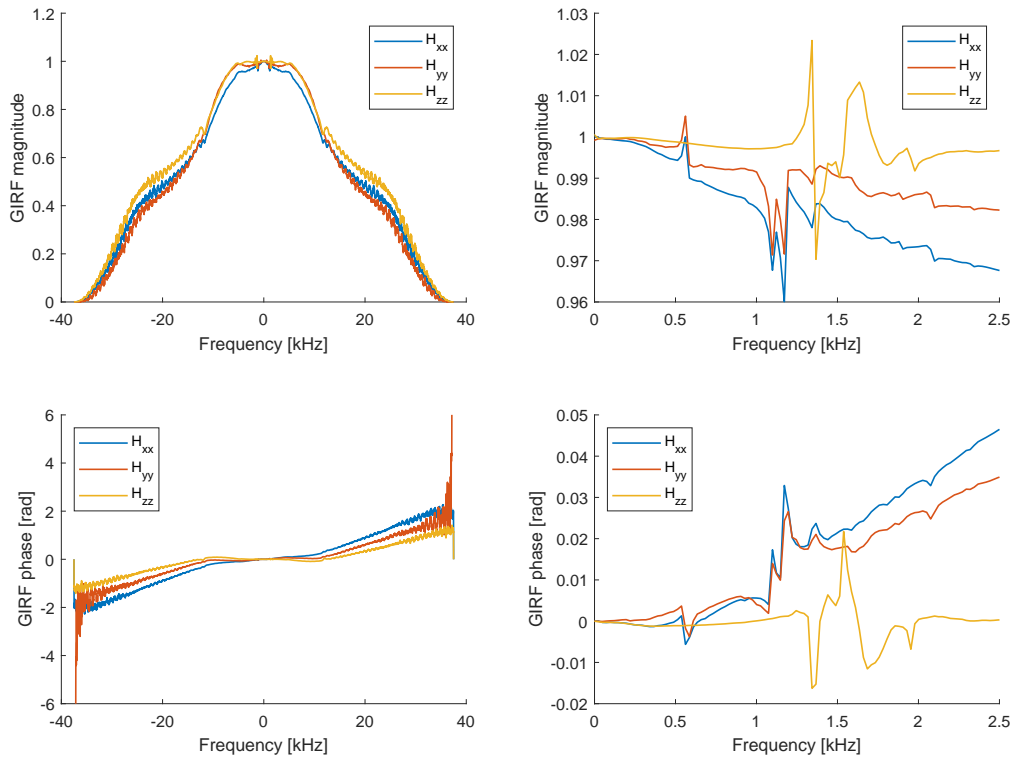Figure 4.3: Magnitude (upper row) and phase (lower row) of the GIRF describing the self-response of the system with a one-channel head-coil. The column to the left shows the whole frequency domain, and the column to the right is zoomed in on low positive frequencies.
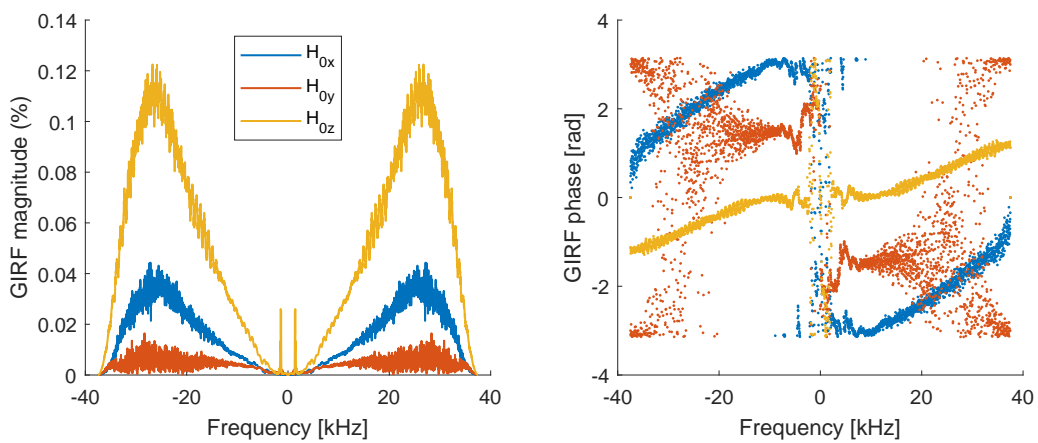

Figure 4.4: Magnitude scaled to the percent of input (left) and phase (right) of the GIRF describing the cross-response of the system with a one-channel head-coil.
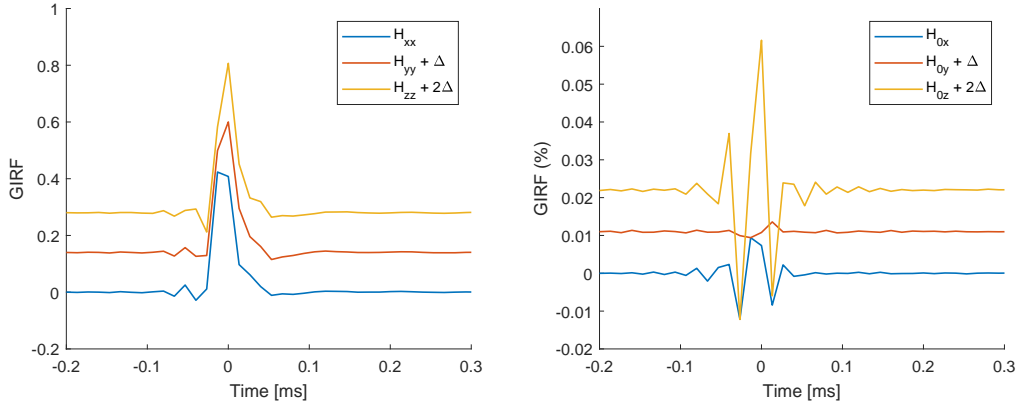
Figure 4.5: GIRF in the time domain for the gradient (left) and B_{0e} (right) responses for the system with a one-channel head-coil. Vertical shifts (Δ) are added to the y- and z-components for better readability.

Figure 4.5 shows the impulse response in the time domain for all three gradient channels with the one-channel head-coil. The gradient response is shown to the left and the B_{0e} response is shown to the right. The gradient responses rise slightly faster than they fall, and there is a tendency for a delayed second lobe before they go to zero. There is also a slight oscillation before the main lobes. The responses start to rise before $t = 0$, which indicates that there is observed a field response before the application of the nominal gradient. This is mainly due to the delay-correction applied in the MR system, which consists of a constant shift in the time of the nominal gradient relative to the acquisition. It is also observed that the main lobes of the z-responses are slightly behind the other directions, which is reflected in the less steep slopes of the phases of the z-direction in figure 4.3 and 4.4. The B_{0e} response has a more oscillating appearance, and the amplitudes vary greatly between the x-, y- and z-directions. As is reflected in figure 4.4, the z-response is the largest, followed by the x-direction and then the y-direction.

The results from the GIRF-measurements with the 32-channel head-coil are presented in appendix B. As expected, they look rather similar to the results of the one-channel coil presented above. Figure B.1 shows the k-space trajectories and ϕ_{B_0} measured with the 32-channel coil. The k-space trajectories are almost identical to the ones measured with the one-channel coil, except that the delays between the measured and nominal trajectories are visibly larger for the 32-channel coil. The time evolution of ϕ_{B_0} in the 32-channel coil after the application of the triangle pulse is almost identical along the x- and z-directions, whereas the drift of the ϕ_{B_0} in the y-direction is smaller for the 32-channel coil. Also, the amplitude of the oscillations in the ϕ_{B_0} along z is larger for the 32-channel coil. During the application of the pulse the induced ϕ_{B_0} looks rather different for the two coil setups, although the phase along the z-direction has the same general shape. After approximately 1.35 ms, the phase induced in the x-direction is almost twice as large for the 32-channel coil than for the one-channel coil. And in the y-direction, the phase measured with the 32-channel coil is much smaller and has a different shape in time compared to the phase measured with the one-channel coil.

The gradients and fields measured with the 32-channel head-coil are shown in figure B.2 in appendix B. Just as for the k-space trajectories, the measured gradient shapes are similar to the ones acquired with the one-channel coil, one difference being a larger delay between the measured and nominal gradient waveforms. The measured B_{0e}-field during the application of the pulse has the same shape but is slightly larger for the 32-channel coil along the x- and z-directions. Along y, the induced field is smaller and has opposite polarity in the 32-channel coil compared to the one-channel coil.

The GIRF describing the self-response of the system with the 32-channel coil is shown in figure B.3 in appendix B. Both the magnitude and phase have the same shape and location of peaks as the GIRF for the one-channel setup. The main difference between the two is that the 32-channel GIRF has lower noise levels for high frequencies, which is due to the increased signal from the 32 coils. Another difference can be seen in the phase of the GIRF for low frequencies, where the phase has a more steep increase with higher frequencies for the 32-channel setup than for the one-channel setup in all directions, indicating a

larger delay just as observed. The cross-response part of the GIRFs, shown in figure B.4 in appendix B for the 32-channel coil setup, are also very similar for the two coil setups. However, in addition to a lower noise level due to the increased SNR of the 32-channel measurements, the phase along the y-direction seems to have a negative slope for the 32-channel setup. The low magnitude of the cross-response GIRF causes unwrapping of the phase to be impossible, and it is difficult to say how the phase behaves for very high and low frequencies.

4.2 Spiral trajectory measurements

Figure 4.6 shows the nominal, nominal delay-corrected, measured, and predicted k-space trajectories of a representative spiral imaging sequence, as well as the distance to the measured trajectory Δk to better visualize the errors. The nominal and measured trajectories gradually separate in the center of k-space and keep an approximately constant Δk during the remaining acquisition, which yields a lower maximal k-value k_{max} for the measured trajectory compared to the nominal. This will lead to a lower resolution if left uncorrected. In both nominal cases, there is observed a high-frequency oscillation in Δk, and the error steadily increases as the trajectories separate until it reaches a plateau that exhibits low-frequency oscillations. From the error, it is also clear that delay-correction improves the accuracy during the beginning of the gradient, although the oscillating behavior is still present.

The GIRF-predicted trajectory closely follows the measured, and the error is considerably smaller than for the nominal cases. It is also noted that both the high and low-frequency oscillations seen in the Δk of the nominal trajectories are less pronounced than the predicted trajectories. The RMS of the difference to the measured trajectory shown at the bottom of figure 4.6 is 0.8 rad/m, 10.0 rad/m, and 16.7 rad/m for the nominal, nominal delay-corrected, and predicted trajectories, respectively. For all spiral trajectories included in this work, the RMS of the difference to the measured trajectories was, presented as median (range): 1.1 $(0.8 - 2.1)$ rad/m, 12.1 $(9.2 - 16.1)$ rad/m, and 19.8 $(12.7 - 22.3)$ rad/m for the predicted, nominal delay-corrected, and nominal trajectories, respectively. There were not seen any major differences in the results for the two coil setups. However, this is based on only two measurements with the one-channel head coil and more measurements are required to say this with certainty. The RMS-values for all measured spiral trajectories are presented in table C.1 in appendix C.

Figure 4.7a shows the gradient time course of the nominal, nominal delay-corrected, measured, and predicted data. The difference to measured data is shown in the lower plot. The measured time course has slightly reduced peak values compared to the nominal, which is caused by the smoothing by the low-pass characteristics of the gradient system. As seen in the figure, the nominal gradient deviates the most from the measured. Delay-correction reduces the difference, but not enough to surpass the predicted gradient. The results from all spiral measurements in this work are as followed, presented as median (range): The deviation between the measured and nominal gradients has RMS-values of 0.26 $(0.15 - 0.29)$ mT/m and maximum values of 0.74 $(0.53 - 0.98)$ mT/m, which are reduced to RMS-values of 0.13 $(0.07 - 0.15)$ mT/m and max values of 0.65 $(0.47 - 0.88)$ mT/m by delay-correction of the nominal gradient. The RMS-values and largest deviations between the measured and GIRF-predicted gradients are 0.02 $(0.01 - 0.03)$ mT/m and 0.08 $(0.05 - 0.13)$ mT/m, respectively.

The measured and predicted time course of B_{0e} is displayed in figure 4.7b. The lower plots show the deviation of the predicted and nominal time courses compared to the measured. The measured 0th order field component exhibits oscillations at the readout gradient frequency with peak values up to 2.7 µT. This behavior is predicted by the GIRF, although the amplitude is often slightly underestimated. The RMS of the difference between the nominal and measured B_{0e} as shown in the figure is 0.81 µT, and the RMS of the difference between the predicted and measured B_{0e} is 0.25 µT. The results for all spiral trajectories in this work, presented as median (range), are as follows: The RMS and max error of the difference between the nominal and measured B_{0e} are 0.78 $(0.52 - 1.20)$ µT and 2.71 $(1.50 - 4.23)$ µT, respectively. This is equivalent to the RMS and peak values to the measured B_{0e} field since the nominal field is zero. The difference between the GIRF-predicted and measured B_{0e} had RMS-values and max errors of 0.25 $(0.20 - 0.34)$ µT and 1.05 $(0.88 - 4.81)$ µT, respectively.
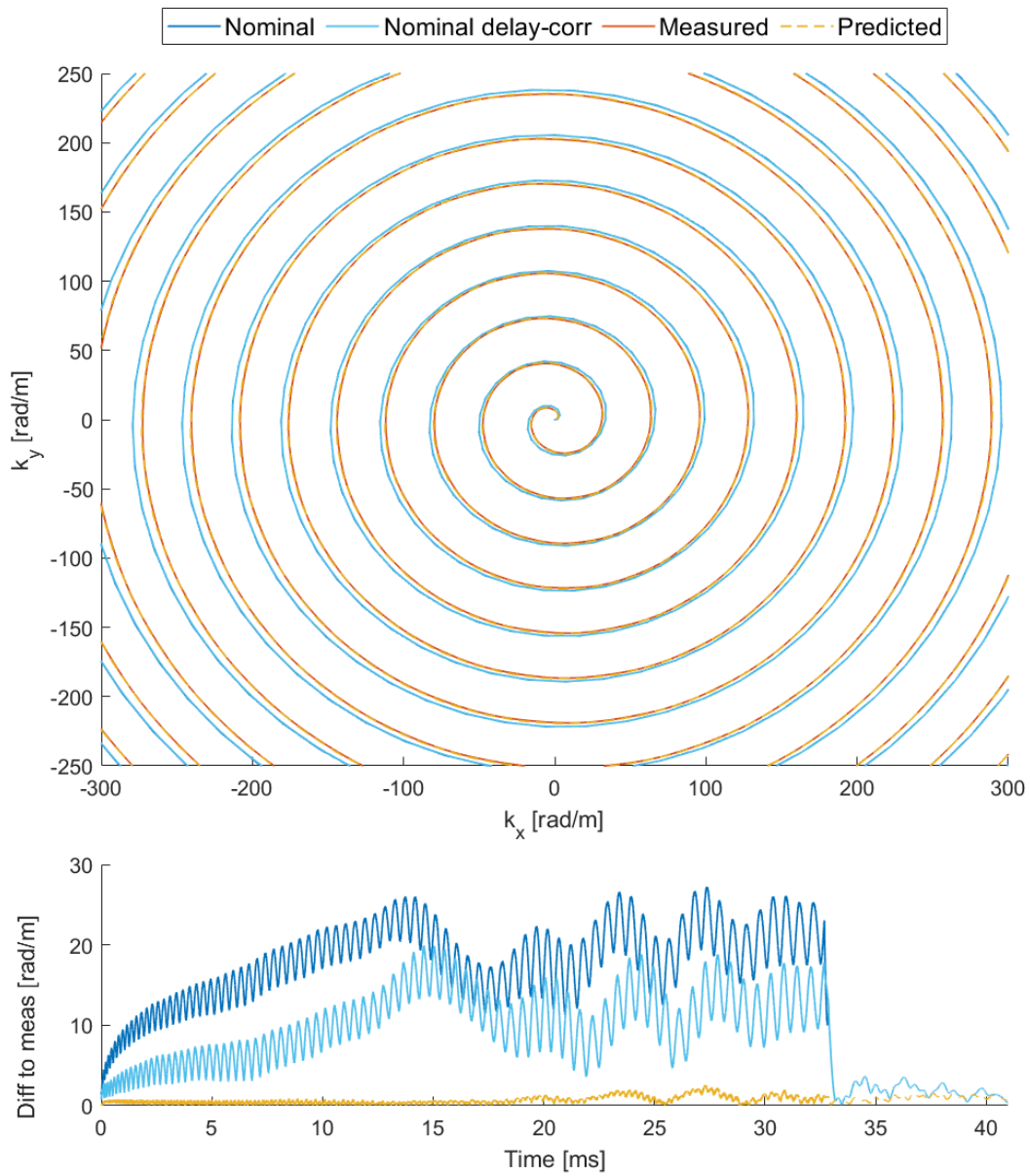
Figure 4.6: Comparison of nominal, nominal delay-corrected, measured and predicted k-space trajectories of a representative sequence. The lower figure shows the difference to the measured trajectory as a function of time.

(a)

(b)
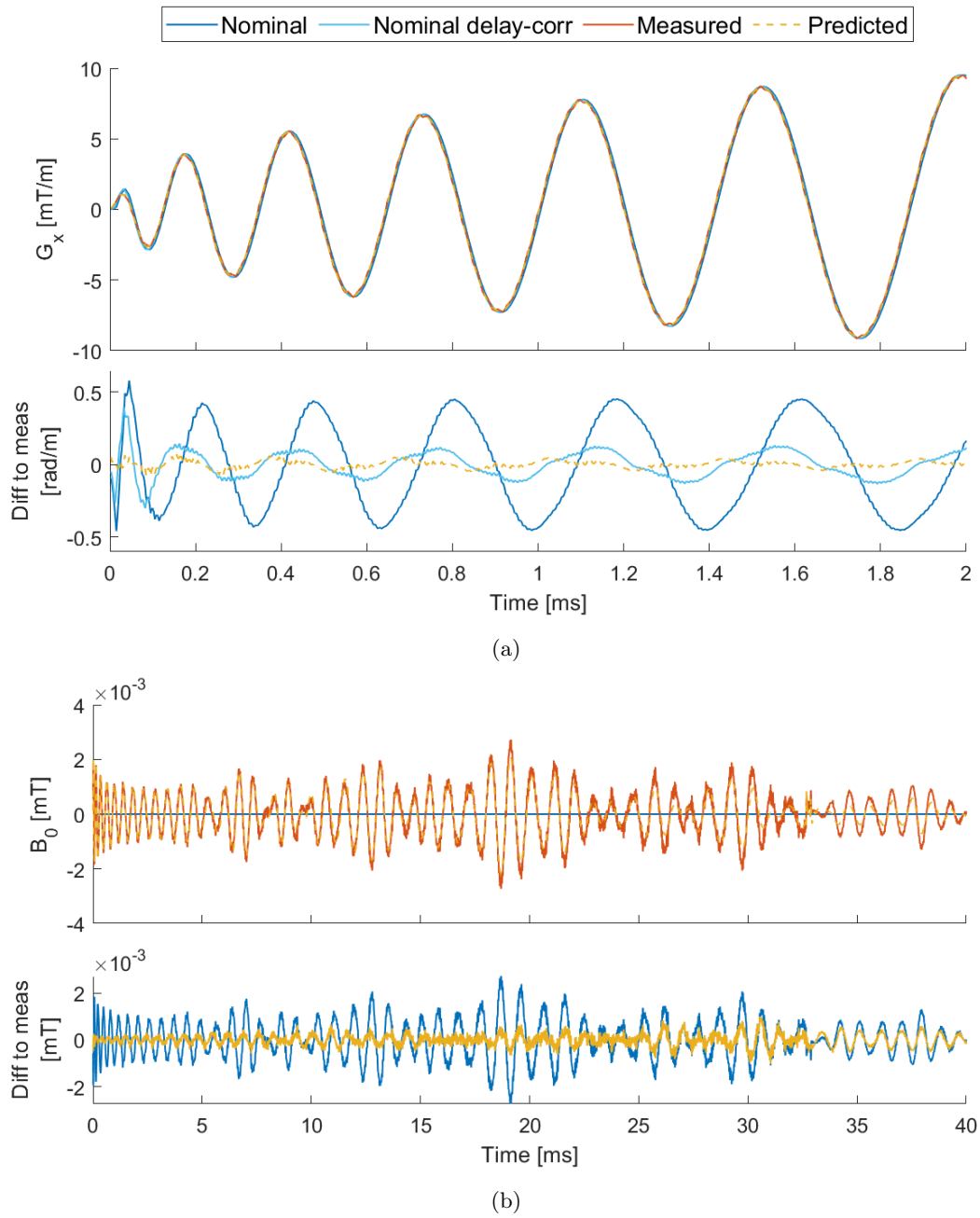
Figure 4.7: Comparison of nominal, nominal delay-corrected, measured and predicted (a) readout gradients G_x and (b) B_{0e} for a representative sequence. The lower plots show the differences to the measured data.

4.3 Image reconstruction

4.3.1 Phantom images

The acquired B_0-map for the phantom measurements is shown to the left in figure 4.8. There is a strong increase in the magnetic field at the bottom of the figure, which corresponds to the posterior direction in the transversal plane. There are also observed smaller variations when moving right-left in the images, with peak values seen in the center of the anterior-posterior axis. These inhomogeneities result in image distortions and blurring, which are visible in the center image of figure 4.8 which displays a reconstructed spiral image with resolution = 1.0 mm and R = 2 without B_0-correction. The most prominent distortion is seen at the bottom of the figure and is due to the increased field strength in that area. By applying B_0-correction during reconstruction, the artifacts due to B_0-inhomogeneities are greatly reduced. This is illustrated in the rightmost image in figure 4.8. However, there are still some imperfections remaining even after B_0-correction, especially at the bottom of the image.

Figure 4.9 shows magnitude images of the phantom for all reconstruction types as described in section 3.3.2 in the following order from left to right: measured trajectories (reference), GIRF-predicted trajectories with ϕ_{B_0}-correction, GIRF-predicted trajectories without ϕ_{B_0}-correction, nominal trajectories with delay-correction, and nominal trajectories. All reconstruction types have been B_0-corrected. Underneath the magnitude images, the voxel-wise difference between the corresponding reconstruction and the reference reconstruction is displayed. The difference images are scaled to the percentage of the maximum values in the reference reconstruction.

All reconstructions based on the nominal trajectories show artifacts in the form of ringing-like circles that gets more prominent towards the edges of the phantom. For higher acceleration factors, aliasing artifacts can be seen in the center of the phantom and are easily distinguishable in figure 4.9b-c. These artifacts have a slight resemblance to the appearance of aliasing in EPI, but due to the nature of the spiral k-space trajectories, the signal is distributed over the entire image and not in discrete ghosts. All artifacts in the nominal reconstruction are often seen in spiral MR images as a result of aliasing and k-space trajectory deviations. By introducing delay-correction to the nominal trajectories, the reconstructed image quality does improve slightly. However, there are still visible artifacts, especially in the form of ringing parallel to the edge of the phantom. The delay-correction seems to have the largest effect on the central aliasing artifact for reconstructions with R > 1.

The reconstructions based on the GIRF-corrections show a large increase in quality compared to the nominal, and the magnitude images are almost indistinguishable from the reference reconstructions. The difference images show that there are small differences to the reference reconstructions, but for all
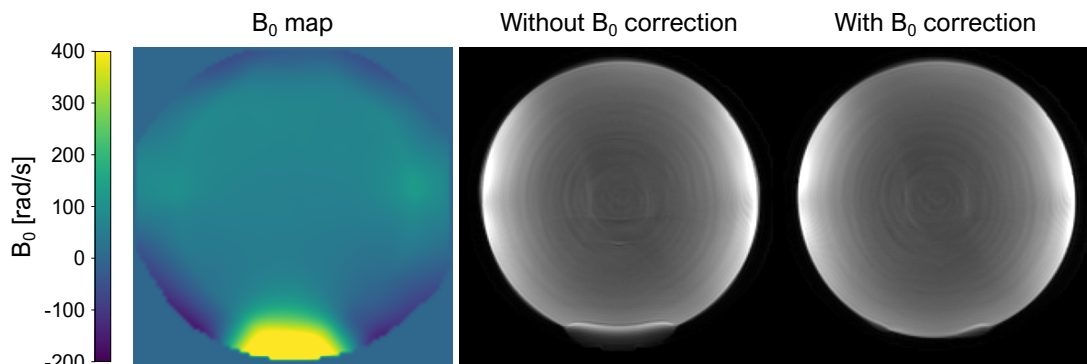
Figure 4.8: B_0-inhomogeneity during phantom measurements, and the effect of B_0-correction. The B_0-map is windowed to [-200 rad/s, 400 rad/s], and the reconstructed image has a resolution of 1.0 mm and an acceleration factor of R = 3.
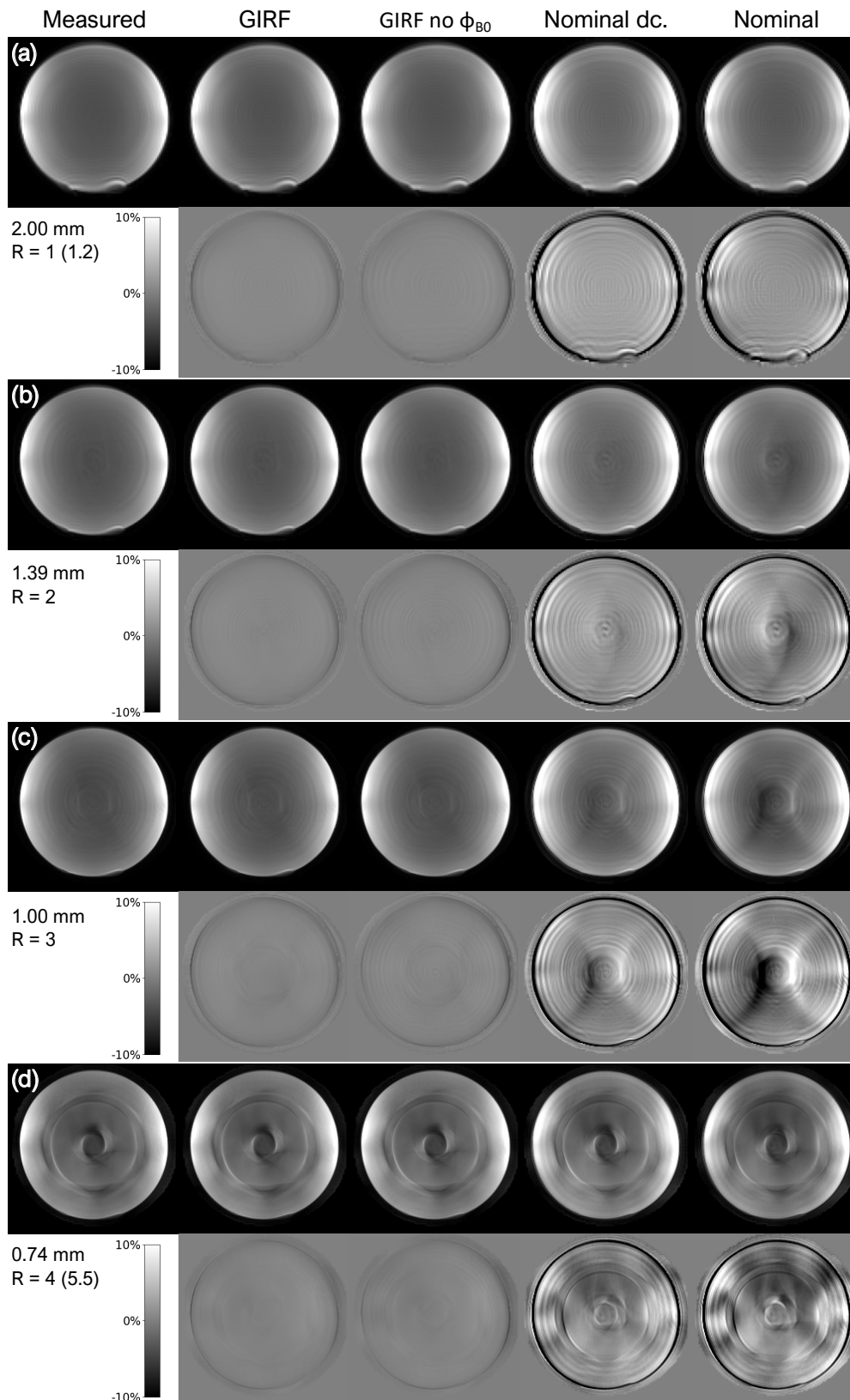
Figure 4.9: Phantom images of selected spiral imaging sequences in transverse orientation. All reconstruction types performed in this work are shown including difference images with the reconstruction with measured k-space trajectories as reference. The difference images are scaled to $\pm 20\%$ of the maximum image value in the measured image. The R-value in parenthesis shows the true value when considering the increase in reconstructed FOV.

reconstructions in figure 4.9, the maximum differences to the reference reconstructions are less than 6% both with and without ϕ_{B_0}-correction. The results also show that applying ϕ_{B_0} has little effect on the reconstructed images in the transversal orientation. Note that this may differ depending on the slice orientation as it decides which gradient axis will play out the spiral sequence. In the transversal case, it is the gradients along the x- and y-direction that create the spiral trajectory, which also happens to be the directions with the smallest B_{0e}-responses (as seen in figure 4.4). The ϕ_{B_0}-correction is therefore expected to be more important for the sagittal and coronal slice orientations, which uses a gradient along the z-direction of the scanner.

The reference reconstructions based on the measured trajectory show a high quality for R-values up to 3. More artifacts are seen for higher R-values, but for reconstructions with R < 4, the images have a high quality despite the artifacts. However, for R-values above 4, more severe artifacts appear in the reconstructed images, as seen in figure 4.9d. On the other hand, this kind of behavior is expected for spiral imaging when the k-space sampling gets too sparse, since the sensitivity profiles do not provide sufficient spatial information to unfold aliasing with high undersampling factors. In this case, the limit seems to lie around R = 4 − 5. Also, the B_0-correction seems to improve with higher R-values and resolutions, as can be seen from the decrease in the distortion in the lower parts of the phantom in figures 4.9a-d. In figure 4.9a with R = 1.2 the artifact causes severe distortion, whereas in figure 4.9d with R = 5.5 it is almost completely corrected for.

Using the reconstructed images with measured trajectories as reference, the results of the reconstructions are quantified in figure 4.10. The figure shows the RMS of the difference in magnitude images, scaled to the percentage of the maximum value in the reference image, for all reconstruction types and spiral sequences. The results presented in figure 4.10 reflects what is seen in the reconstructions in figure 4.9. There is a large improvement of quality when using the GIRF-predicted trajectory during reconstruction compared to using the nominal, where most spiral images see an improvement from an RMS-value of over 5% with the nominal to an RMS-value of less than 1% for the GIRF-predicted trajectories. Figure 4.10 also shows more clearly that while delay-correction does improve the RMS slightly in some cases, there are also cases where the RMS-value stays the same or increases by a fraction when applying delay-correction. The latter is seen for R = 1 − 2 with resolutions ranging from 1.71 − 1.21 mm. By applying ϕ_{B_0}-correction to the reconstructions with GIRF-predicted trajectories, the RMS-values are slightly reduced, as was observed in the reconstructed images. No systematic difference in the RMS values is observed for the different resolutions or acceleration factors.
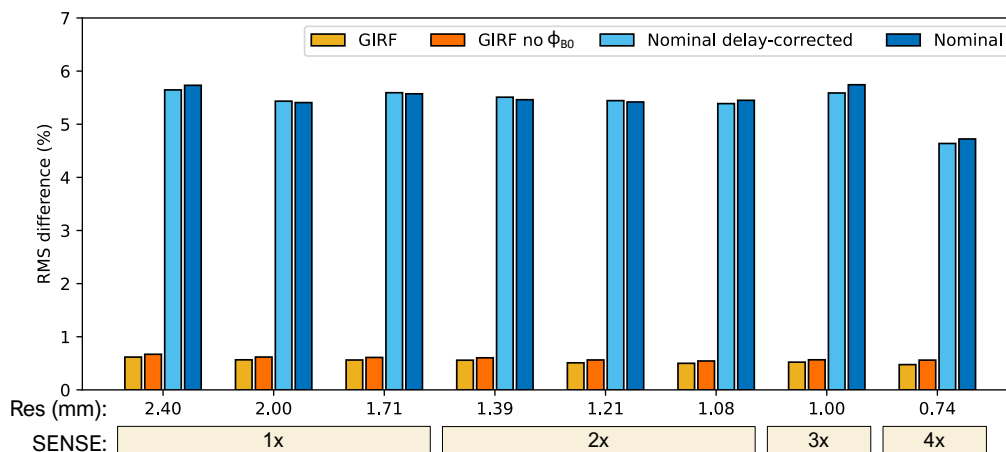

Figure 4.10: The root-mean-square difference over all voxels in a selection of difference images, where the measured k-space trajectory reconstruction was used as reference.

4.3.2 In vivo images

The B_0-map acquired for the in vivo measurements is displayed in figure 4.11 along with a reconstructed image without B_0-correction and a reconstructed image with B_0-correction. The in vivo field map is less homogeneous and has higher field deviations compared to the phantom measurements. This is to be expected due to the increased complexity of a human brain compared to a phantom, with more interfaces between tissues with different magnetic susceptibilities. Especially the frontal part of the brain, which is in the proximity of the sinuses, shows large field disturbances due to the air-tissue interface. This results in a severe off-resonance artifact in the frontal region which is typical for spiral images. By applying B_0-correction to the image, the severity of the artifacts is reduced, especially near the sinuses. More subtle corrections can also be seen on the skull encapsulating the brain and in the central and posterior parts of the brain. There are still some off-resonance artifacts left in the corrected reconstruction, but it is clear that the B_0-correction did have a large impact on the image quality

In vivo magnitude images of all the different reconstruction types with B_0-correction are shown in figure 4.12 along with the corresponding difference images. The difference images were calculated and scaled in the same fashion as for the phantom measurements. Despite the short TE, there is still sufficient contrast and resolution to distinguish between white and gray matter in all images, and increasing the TE would increase the contrast. Compared to the phantom measurements, the in vivo images have a smaller visual difference depending on which trajectory was used during reconstruction. Some visual differences can be seen in the magnitude images and figure 4.13 points out some examples in the image with 1.0 mm resolution and R = 3. By considering the difference images, it is more clear to see that the quality of the images changes depending on the reconstruction type. In the difference images of the nominal trajectories, dark shades can be seen followed by lighter areas close to the edges of the brain, indicating that the nominal image is more blurred than the reference. By introducing delay-correction to the images, the area inside the brain shows a more homogeneous difference from the reference image, but the blurring effect on the edges is still present as can be seen in the difference images.

By applying GIRF predictions during reconstruction, the image quality is increased when compared to the reference image just as seen in the phantom case. Improvements are seen in the magnitude images as shown in figure 4.13, but is perhaps more convincing in the difference images shown in figure 4.12. The average RMS of the difference images shown in figure 4.12 is reduced from 5.1% in the nominal case to 0.4% with GIRF-correction. Whether or not ϕ_{B_0}-correction is applied does not seem to increase the quality substantially. The average RMS of the difference images in figure 4.12 is only reduced by 0.03% when applying ϕ_{B_0}-correction. Note that just as for the phantom reconstructions, all results are from images acquired in the transversal orientation, and it might be reasonable to expect larger improvements with ϕ_{B_0}-correction for different slice orientations.
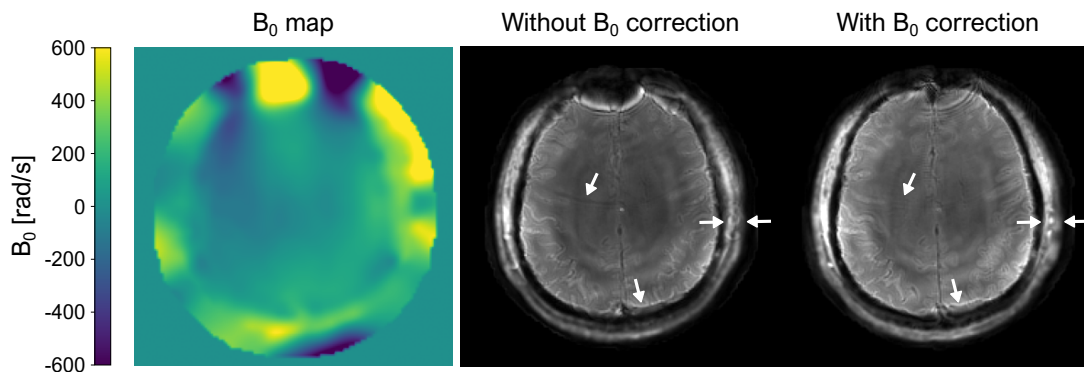
Figure 4.11: B_0-inhomogeneity during in vivo measurements, and the effect of B_0-correction. The B_0-map is windowed to [-600 rad/s, 600 rad/s], and the reconstructed image has a resolution of 1.0 mm and an acceleration factor of R = 3 during acquisition. Due to the increased FOV during reconstruction, the reconstructed R-value is closer to 3.4. The arrows are pointing out the more subtle differences in the images.
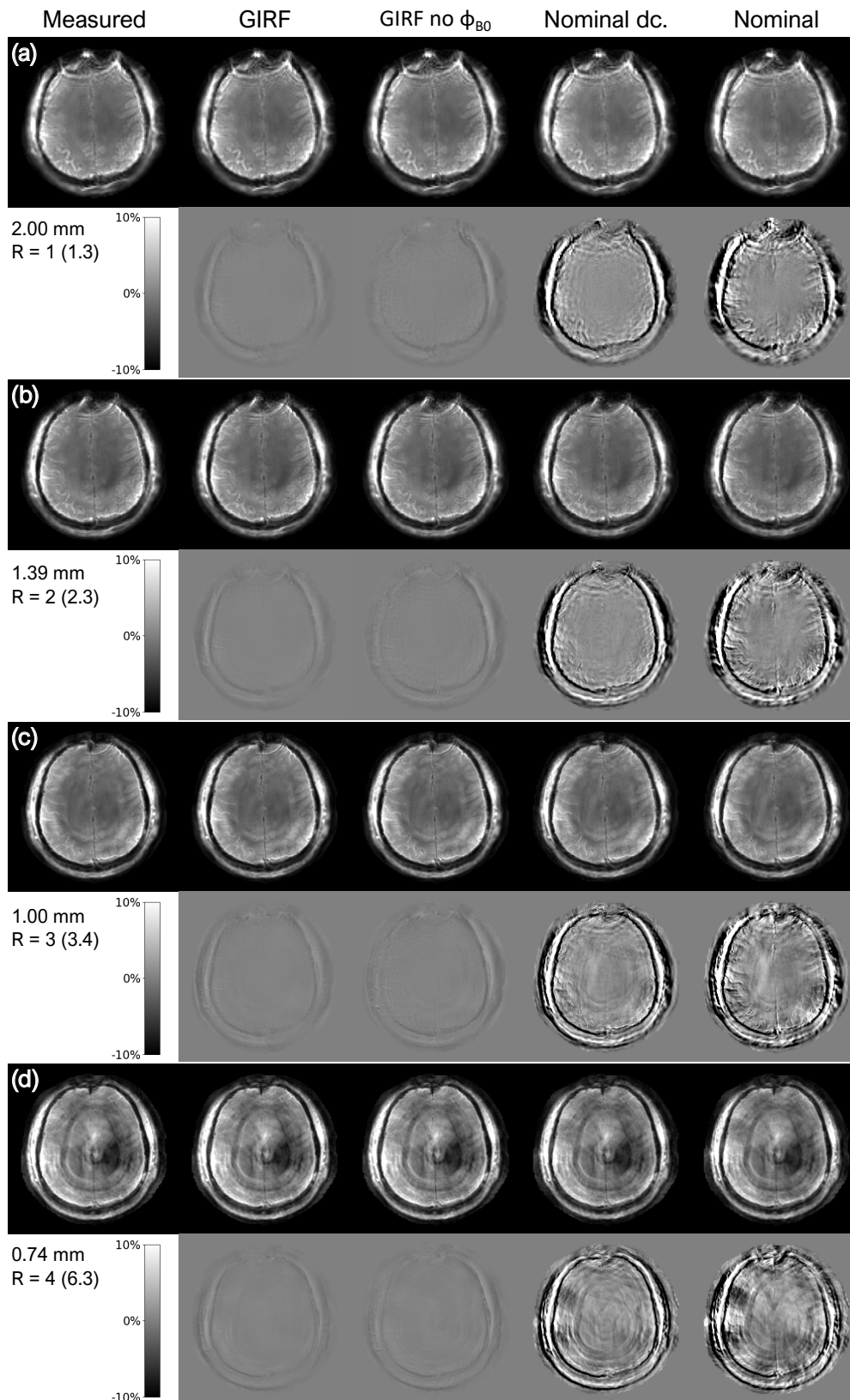
Figure 4.12: In vivo images of selected spiral imaging sequences in transverse orientation. All reconstruction types performed in this work are shown including difference images with the reconstruction with measured k-space trajectories as reference. The difference images are scaled to ±20% of the maximum image value in the measured image. The R-value in parenthesis shows the true value when considering the increase in reconstructed FOV.
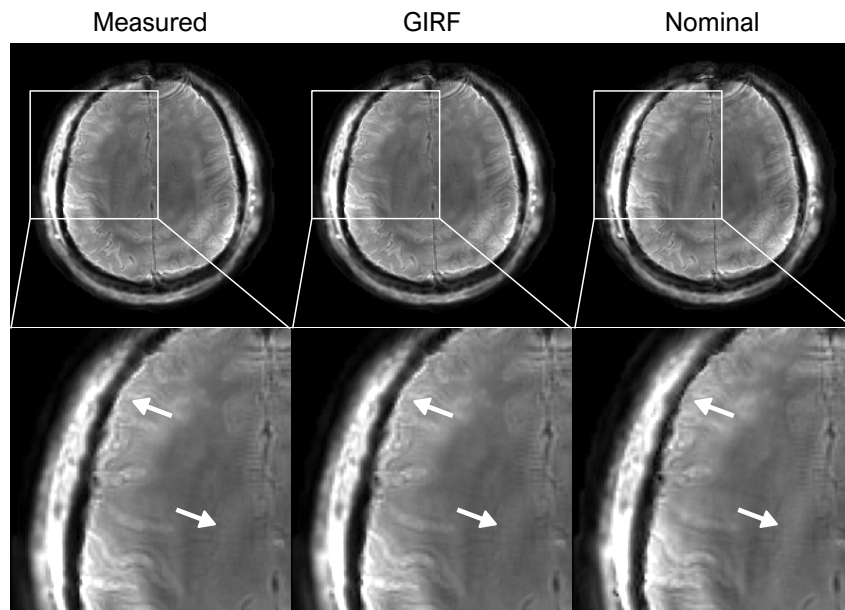
Figure 4.13: Differences in magnitude images for the measured, GIRF, and nominal reconstruction types for the spiral sequence with 1.0 mm resolution and R = 3. The lower row is zoomed in on the rectangles in the upper row, and the arrows point out the main visual differences in the images.

For R $\geq$ 2, ring-like intensity variations can be seen in the central region of the brain images even for the reconstructions based on the measured trajectories. In figure 4.12b with R = 2.3, these are barely visible and have a broader appearance than in figure 4.12c with R = 3.4. For very high R-values, as shown in figure 4.12d with R = 6.3, the rings appear with sharp edges, similar to the phantom images with the highest R-value. Such artifacts are typical to see when there are residual aliasing in spiral images. But despite seeing more severe aliasing artifacts for higher R-values, the B_0-corrections seem to improve with increasing R, just as for the phantom measurements. For the highest R-value shown in figure 4.12 the distortion due to the field variations in the frontal area is almost entirely gone after B_0-correction.

5 Discussion

In this section, the chosen methods and acquired results will be discussed in four steps. First, the results will be interpreted and compared with other works and literature. Second, the choice of methods will be discussed and the limitations and restrictions of the methods will be laid bare. Third, possible applications for the results will be discussed. In the fourth and final part, possible extensions and further work will be presented.

5.1 Interpretation of the results

In the first part of the work presented in this report, a GIRF was determined for a 7T system for two different coil setups. The GIRF was made to include all responses between two relevant end-points for the user, which are gradient input on the scanner and the actual field behavior seen by the object placed inside the scanner. The results show that GIRF-characterization based on trajectory measurements acquired with a thin-slice excitation method is straightforward and fast. Due to limitations of the trajectory measurements, only self-responses and the cross response between 1st and 0th order fields were determined, although the GIRF-model is easily extended to include more cross-responses of higher-order fields.

The GIRF-results can be interpreted by comparing them to an ideal system. In an ideal system, the self-response would have had a magnitude of one and zero phase for all frequencies. This is not the case for the self-response of the system looked at in this work. The system has a low-pass behavior, where the magnitude of the response starts to fall off for frequencies above 10 kHz. It should be noted that the frequency composition of the input gradients does not cover infinite frequencies, so the response might not be accurate for very high frequencies. Luckily, frequencies of 10 kHz and above are rarely used in spiral imaging, and the spiral sequences looked at in this work all had frequencies well below 4 kHz. In this range (≤ 4 kHz) the magnitude of the response is close to one but does show a very frequency-dependent behavior with all the distinct peaks. An ideal response with a constant group delay would have a linear phase response where the slope of the phase determined the duration of the delay. For low frequencies, the phase of the measured response is approximately linear, indicating that delay-correction will have a good effect on trajectory correction, but in similarity to the magnitude response, it has frequency-dependent peaks and bumps that a simple delay-correction will not be able to correct for. All of these deviations from the ideal system, with or without group delay, indicate that improvements are expected when using the GIRF to correct for gradient, and thus k-space trajectory, deviations.

The GIRF can also be used for more than just trajectory correction, as the GIRF determined in this work also includes a cross-response that describes the time-dependent behavior of eddy-current induced 0th order fields. An ideal system would not have any eddy currents, and an ideal cross-response is zero for all frequencies, both in magnitude and phase. The cross-response measured for the 7T system in this work is highly frequency-dependent and displays a high-pass behavior. The magnitude of the response varies greatly over the three input directions. A gradient in the z-direction induces a much larger 0th

order field than a gradient in the x-direction. If this is not corrected for, one might expect worse quality in images that use gradients along the z-direction. The z-direction also shows resonance peaks at 1.44 kHz, which is within the range of frequencies covered by the spiral sequences in this work. Unfortunately, later parts of the work only included transversal measurements which mainly utilize gradients along the x- and y-directions, so the effects of this resonance have not been investigated.

When the GIRF is defined and determined as in this work, it combines the response of all linear distortions of the gradient waveforms from the gradient design on the scanner to the field measurements. It is therefore impossible to separate the origins of the response without performing additional measurements that measure both input and output of isolated stages in the gradient processing chain. Some examples that will affect the frequency composition of the gradient are software signal processing, eddy-current compensation, gradient amplifier characteristics, cable effects, coil coupling, eddy currents, and mechanical responses of the gradient system [23]. However, some steps might add such distinct responses to the gradient that they might be distinguished from the shape of the GIRF. One such example is the channel-specific characteristic peaks that were observed in the self-response of the GIRF. Based on their frequencies these peaks are most likely due to mechanical resonances of the gradient coils. This is supported by earlier observations of acoustic responses at similar frequencies [43, 44]. Furthermore, in the work presented by Vannesjo et al., which the GIRF-calculation in this work is based on, they measure peaks in the range of 1.0 - 1.7 kHz which they also ascribe to mechanical resonances of the gradient coils [23].

Despite being called a one-time effort, the GIRF might need to be determined once for each coil setup that is to be used alongside GIRF-predictions. The results of this work show differences between the field responses of a one-channel and 32-channel head receive coil. The reason for this is unknown, but a leading theory is that the eddy currents that are induced in a coil will vary depending on the coil geometry, and as a result, the unique response will affect the image encoding in a coil-specific manner. It is therefore important to measure coil-specific GIRFs by performing separate field measurements inside the relevant coils if the responses are too different. It has been shown in some cases that the effects of different coils are negligible [34], but this must be determined on a coil-to-coil basis. Note that the effect of different GIRFs on the trajectory predictions and image reconstructions has not been investigated in the current work, so it has not been shown whether the differences between the coils will impact the image quality.

In the second part of the work, spiral sequences were measured and compared to the nominal and GIRF-predicted gradient waveforms. This part had two main aims, (i) to measure the true deviation of the nominal trajectories from the measured trajectories, and (ii) to assess the quality of the GIRF by comparing the GIRF-predictions to the measured field responses. If the GIRF was determined correctly, all deviations between the measured and predicted trajectories are expected to be due to either non-linear effects, insufficient frequency coverage of the input used for GIRF-calculation, or higher-order field terms. The results show that (i) there is a large difference between the nominal and measured gradients. By introducing a simple delay correction, the error is reduced but it still causes deviations in the k-space trajectories that are expected to negatively affect the quality of the reconstructed images. The results also show that (ii) the GIRF-predicted trajectories only have small deviations from the measured waveforms, and greatly increase the quality compared to nominal trajectories. The median RMS error over all measured gradients in this work falls from 0.26 to 0.02 mT/m when using nominal and predicted trajectories, respectively. In addition, the nominal trajectory provides no information about the time fluctuation of the magnetic field, and the RMS difference to the measured B_{0e} field is reduced from 0.78 to 0.25 µT when applying GIRF-correction to the nominal response.

The third part of the work demonstrated that the GIRF-predictions can be used to achieve spiral image reconstructions that have the same level of quality as those made with measured trajectories. It further emphasizes and demonstrates why the nominal trajectories are not sufficient and that a simple delay-correction will have little effect on improving the image quality for this system in the transversal slice orientation. Another interesting observation was that inclusion of the 0th order field term, ϕ_{B_0}, had little effect on the image quality. It has earlier been shown to affect spiral imaging [29, 34], but it has also been shown to have an even larger effect on other imaging schemes such as EPI [34]. The results also show that further measures may be required to achieve a sufficient reconstruction quality as even the images reconstructed with the measured trajectories show artifacts and blurring for the in-vivo case.

This might also cause the images with the different trajectories to look almost identical, despite voxel-by-voxel difference maps showing an improvement with GIRF-predictions when compared to reconstructions with measured trajectories. Overall, GIRF-prediction holds great promise towards being a key trajectory correction strategy, as it yields reconstructions with RMS differences of $> 1\%$ over entire slices compared to measured trajectories.

Although the quality may seem low for the reconstructed in vivo images, the images are promising considering earlier work on single-shot spiral imaging. Spiral imaging was introduced in the early days of fast imaging, before the introduction of gradient systems capable of handling EPI [45]. Due to the arrival of EPI and issues relating to gradient deviations and computationally demanding reconstructions, the effort put into spiral imaging was later reduced. However, in the last few years, several published works have shown great potential for spiral imaging. In a study by Engel et al. [46], single-shot spiral imaging was performed on a 7T system, and examples of their results are shown in figure 5.1. Figure 5.1a shows an image with similar parameters as in this work, with TE = 3 ms, T_{RO} = 18.5 ms, and a resolution of 1.5 mm. Figure 5.1b shows a higher-resolution image from the same work resulting from a longer readout with TE = 25 ms, T_{RO} = 53 ms, and a resolution of 0.8 mm. Both images were acquired with R = 4.

Compared to the images in figure 5.1, the reconstructions shown in this work have more artifacts in the form of off-resonance distortions, residual aliasing, and blurring in the areas around the brain. However, there are three main reasons for this. First, whereas the sequences in the study by Engel et al. either had low resolutions with short acquisition times (1.5 mm, 20 ms) or high resolutions with longer acquisition times (0.8 mm, 60 ms), this work attempted to use higher resolutions with slightly lower acquisition times (1.0 mm, 40 ms). This indicates higher acceleration factors which are expected to increase the amount of noise and residual aliasing in the images. Second, the trajectory corrections in the current work were based on pre-measured trajectories from thin-slice excitation, whereas the work by Engel et al. included concurrent field monitoring with field probes. Third, more time was probably invested in getting the correct parameters in every reconstruction step for the results presented in figure 5.1. Especially the quality of the B_0-maps used for B_0-correction and the sensitivity maps used for SENSE reconstruction is expected to be higher in the study by Engel et al. All in all the reconstructions shown in this work look promising, although there is still work to do to improve the reconstruction quality.

The artifacts in the in-vivo measurements pose an issue for future applications of the spiral reconstruction in this work, which will be discussed later in section 5.3. It is therefore important to understand what exactly is causing the artifacts and how they can be reduced. Due to the high similarity between the measured and predicted spiral trajectories and image reconstructions, the reasons for the low image quality are most likely not due to flaws in the GIRF correction. Besides that, more investigations must be performed to isolate the origins of the image artifacts, but speculations based on observations in this work and other literature can be made. Firstly, spiral imaging is highly susceptible to B_0-inhomogeneities as observed in this work, and even after corrections, there were still strong off-resonance artifacts present

(a)   (b)
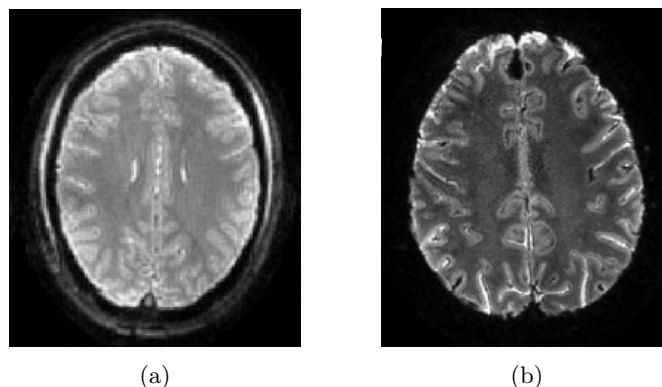
Figure 5.1: Single-shot spiral-out MR images acquired at a 7T scanner with R = 4. (a) TE = 3 ms, T_{RO} = 18.5 ms, resolution = 1.5 mm. (b) TE = 25 ms, T_{RO} = 53 ms, resolution = 0.8 mm. The images are retrieved from the study by Engel et al. [46].

in the reconstructions. Since the precessional frequency of the nuclei is proportional to the field strength, off-resonance effects are expected to be worse at the 7T compared to the 3T scanners. Unfortunately, as B_0-correction is somewhat outside of scope for this work, there was not enough time to optimize the acquisition and calculation of the B_0-maps. The result of B_0-correction strongly depends on the quality of the field maps, so putting more effort into creating high-quality and high-resolution field maps is expected to decrease the appearance of off-resonance effects. Secondly, the residual aliasing seen for high R-values is most likely due to errors during the SENSE reconstruction, which is often caused by imperfections in the sensitivity maps. Just as for the B_0-maps, there was not enough time to optimize the sensitivity maps, and improving these might reduce the residual aliasing. At some point, however, there is a limit to the unfolding that can be achieved with a given coil setup, which means that an increase in acceleration factor will only introduce new artifacts no matter how optimized the sensitivity maps are. Based on the results in this work, this limit seems to be around R = 4 - 5.

Another issue is that the GIRF-predictions are not better than the measurements they were based on, which were made with thin-slice excitations that only account for the 0th and 1st order field terms. Cross-responses between higher-order field terms were not recorded, and their effects are thus not included in the reconstructions with measured or predicted field responses. An example of a higher. Higher-order cross-terms have been reported to affect DWI [24], which is a key application of spiral imaging. However, whether higher-order cross-terms contribute to the low image quality of the results in this work remains unknown. More details about the restrictions of thin-slice excitation as a means for trajectory measurement will be discussed in more detail in section 5.2.

An interesting observation that can be done from the image reconstructions is that the distortions due to B_0 inhomogeneities are less prominent for higher R-values and resolutions. This is not unexpected and can be explained by looking at the speed through k-space during image acquisition. Since the image artifacts caused by off-resonance effects occur due to an accumulation of phase over time, the longer an acquisition is, the worse the artifact will be. By reducing the readout time by increasing the speed through k-space, the amount of phase that accumulates will be smaller and easier to correct. By just looking at the acquisition times of the different spiral acquisitions in this work, however, one might see that the increase in resolution causes the readout time to be approximately the same for all R-values. However, since a high resolution corresponds to higher k-space values, the speed through k-space is considerably greater for the high R-values. Also, most information about the image lies at low frequencies. Thus, despite having the same readout length, sequences with high R-values will spend a shorter time at low frequencies, thus being less strongly affected by off-resonance. In other words, increasing the acceleration factor does not only allow for higher resolutions within reasonable times but also reduces off-resonance artifacts, which are a big issue in spiral imaging, especially at 7T.

5.2 Advantages and limitations of methods

The method used for field measurements in this work was a scheme based on a thin-slice excitation approach. This method was primarily chosen for its simplicity, given that no additional equipment is needed other than a phantom. The main limitation of such a thin-slice approach is that it is restricted to one direction at a time and that it is limited to 0th and 1st order field measurements. Also, the field response measurements must be obtained separately from the image acquisition. The fact that only one direction can be measured at a time, and that twice as many gradient waveforms must be measured to include the effects of B_0 eddy currents, causes such measurements to be rather time-consuming. To achieve good SNR in the measurements, several averages were also performed, resulting in a total acquisition time of 36 minutes for the triangle gradient measurements that were required for the GIRF-calculation.

Other more sophisticated field measurement techniques, such as dynamic field cameras based on NMR field probes [19, 20, 30], allows for concurrent field monitoring as well as recording the full spatiotemporal field evolution in one acquisition. In other words, it is faster and provides higher-order field information compared to the thin-slice method in this work. However, field probe measurements require additional advanced hardware, and are probably beyond the capabilities of most MR sites. Overall, the thin-slice

excitation approach does deliver high-quality results within its limitations. By accepting longer scan times and limited spatial field terms, this approach well serves the aim of determining a GIRF at any site. Should these restrictions limit the quality of the GIRF-predictions, however, another method for measuring field dynamics can be considered.

The main reason why GIRF-correction is of high interest in fast imaging is that it enables high-quality k-space trajectory corrections, potentially along with other field terms, without the additional time or hardware that other trajectory correction approaches demand. This is especially relevant to spiral imaging as there are a limited number of alternative correction strategies compared to more standard imaging schemes such as EPI. However, GIRF-correction is limited by the underlying assumptions of an LTI system. In other words, any system response that is not linear and time-invariant will not be accounted for by the GIRF-predictions. Luckily, the most important sources of dynamic field imperfections are well modeled as LTI, but smaller deviations from the LTI model are expected due to various reasons [47–49]. Some non-linear contributions to the gradient processing chain may include gradient amplifier non-linearities and concomitant fields, and some time-dependent contributions include external sources that induce field fluctuations as well as thermal heating of the gradient coils. The latter might be a problem for extensive EPI or spiral imaging schemes that tests the limits of gradient systems. Some of these effects might be dealt with by applying model extensions or complementary measurements. In a recent work by Nussbaum et al., thermal variation in gradient response was accounted for with a linear thermal extension of the LTI model [49].

When being used as a post-correction strategy, the GIRF-corrections are only applicable if the acquired data contains all necessary image information. This means that the actual k-space sampling must fulfill the Nyquist criterion, or if parallel imaging is used, it must be sampled sufficiently densely given the number and sensitivity profiles of the receive coils. If the field perturbations due to system imperfections cause too large trajectory deviations, the sampled k-space may provide insufficient image information and the reconstructed image will display artifacts. This must be taken into account, especially for high R-values, since the GIRF-correction simply estimates the true k-space trajectory without taking into account whether it will have sufficient coverage or not. As will be described more in detail in section 5.3, insufficient k-space coverage due to gradient imperfections could be accounted for by using the GIRF for pre-emphasis.

To achieve sufficient resolution within a reasonable acquisition time, undersampling with iterative SENSE reconstruction was used in this work. Longer acquisition times will on one side cause increased off-resonance effects and blurring due to T_2^*-decay along the trajectory [46], but on the other side allow for higher resolutions or FOVs by sampling higher or more dense k-values, respectively. What acquisition time or resolution is of interest depends on what kind of application the MR image is meant for, which be discussed in section 5.3. Nevertheless, the higher a resolution that can be achieved within a given acquisition time the better, and parallel imaging is therefore an essential part of any high-resolution MR acquisition.

However, parallel imaging such as SENSE does come at a cost. Since it samples less signal than what is usually necessary to reconstruct an image, the SNR decreases with a factor of $\sqrt{R}$ [37]. In addition, noise in the image can be enhanced during reconstruction if the coil geometry is suboptimal and regions in the coil sensitivity profiles are too similar [6]. Another artifact that may be caused by SENSE reconstruction is residual aliasing, which occurs when there is an error in the unfolding process. Such errors arise if the coil sensitivity maps are inaccurate or if the R-value is too high for the given coil geometry. Inaccuracies in the coil sensitivity profiles can be caused by patient movement or in areas with low signal. Residual aliasing is hard to distinguish in spiral imaging, as opposed to cartesian sampling schemes, as the signal from one pixel in the full FOV is folded into all the pixels in the reduced FOV. In EPI, residual aliasing is seen as discrete ghosts repeated R times over the full FOV, whereas aliasing is more difficult to distinguish in spiral images. An illustration of the effect of aliasing in EPI and spiral imaging is provided in figure 5.2. Therefore, it is essential to have a coil geometry with good coverage along with high-quality sensitivity profiles when using high acceleration factors in SENSE.
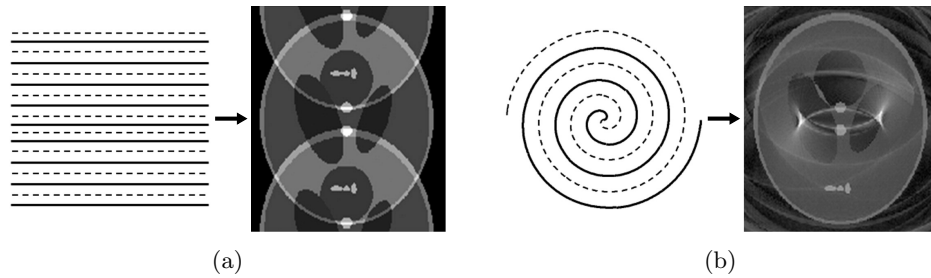
(a) (b)

Figure 5.2: Illustration of aliasing for (a) an EPI sequence and (b) a spiral sequence with an undersampling of R = 2. The images are retrieved from the review paper by Delattre et al. [27].

5.3 Applications

Despite only being applied to spirals in this work, the GIRF-based correction approach is not limited to just spiral trajectories. Studies have shown promising results for several fast imaging schemes, such as in the work by Vannesjo et al. for EPI and variable speed EPI (VS-EPI) [34]. This indicates that GIRF-based predictions might have the potential to remove the need for sequence-specific correction techniques, which usually require additional scan time or sequence alterations. GIRF-predicted k-space trajectories also pose as a good substitute for more hardware- or time-demanding techniques for k-space trajectory or gradient measurements when the time or hardware is lacking. Also, the GIRF-based method used in this work has the potential of correcting for cross-term field responses of any order, if they can be measured [23]. Effects of cross-term responses could then be accounted for by using a higher-order image reconstruction like the one proposed by Wilm et al. [24].

In cases where the altered gradient waveforms cause insufficient encoding, the GIRF could be used as a basis to calculate pre-emphasis filters that can be used to determine nominal gradients that will result in the desired trajectory shapes [50]. This will help solve the issue described in section 5.2 of insufficient k-space sampling due to trajectory deviations caused by the system response. Such filters will attempt to boost the input for the frequencies that are attenuated most by the system response. However, boosting the signal requires more power and might be limited by the hardware. A solution that accounts for the hardware restrictions is to combine pre-emphasis filters with post-acquisition GIRF-correction. Applying pre-emphasis within the limitations of the hardware will still provide improved trajectory coverage, and the remaining errors can be corrected post-acquisition.

The results in this work, along with earlier published results on 3T scanners [29, 34], shows that GIRF-correction might be an important step in the direction of implementing spiral imaging in clinical settings when combined with B_0-correction. Single-shot spiral imaging is especially interesting for neuroimaging applications such as BOLD fMRI [45, 51], DWI [52], and ASL [53]. BOLD fMRI uses T_2^*-weighted imaging to detect neural metabolism by detecting changes in the oxygenation of hemoglobin [1]. When the fraction of oxygenated hemoglobin (oxyhemoglobin) increases due to neural metabolism, the local T_2^* increases and results in a higher signal in the MR image. By acquiring a series of T_2^*-weighted images over time, it is possible to study which parts of the brain that are activated and undergo neural metabolism. DWI is an imaging technique that visualizes the diffusion rates in different tissues by utilizing strong phase-encoding gradients [3], and is reliant on fast imaging to remove contributions from all motion that is not diffusion. ASL is an MR method for measurement of cerebral blood flow and uses fast imaging to ensure a sufficient SNR [2].

Currently, these methods are typically performed with EPI, which does not provide the same acquisition efficiency as spiral imaging. Also, EPI is more sensitive to motion and pulsatory flow compared to spiral imaging. Patient movement will cause discrete ghosting in EPI, whereas spiral will show blurring which is often more desirable. The movement of spins during and between acquisitions can cause artifacts such as signal loss and distortions, which will scale with the additional phase of the spins which is proportional to the size of the gradient moments [45]. In EPI, the gradient moments at the center of k-space, albeit

being zero, grow rapidly at a slight distance to the center. In single-shot spiral-out imaging, however, the center of k-space is sampled at the very beginning of the acquisition, meaning that the gradient moments remain small at the center of k-space. As a result, spiral imaging is less sensitive to pulsatile flow.

The improvements in image quality due to GIRF-correction, as shown in the results, are of particular interest for quantitative MR imaging (qMRI), where the acquired signal is used to calculate quantitative measures. An example of qMRI is when the signal from DWI is used to calculate a map of the apparent diffusion coefficient (ADC). In qMRI, physical values such as ADC, velocity, and relaxation times are determined on a voxel level and are highly dependent on precise signal localization. Thus, even though the in vivo reconstructions presented in the results do not improve much visually, the improvements on a voxel level, as shown in the difference images, show that the GIRF-predictions hold promise for qMRI applications.

What distinguishes the results in this project from the similar works by Robison et al. [29] and Vannesjo et al. [23] is that the measurements in this work were performed on a 7T scanner. Ultra high field MR imaging provides a higher SNR and enables sub-millimeter resolution in fast imaging, which is especially attractive for BOLD fMRI. In a study by Kasper et al., promising results have been found for spiral BOLD fMRI at 7T using concurrent field monitoring with NMR field probes, where a single-shot spiral sequence with a resolution of 0.8 mm provided high-quality fMRI results [51]. ASL usually targets lower resolutions, but benefits from the high duty cycle and short TE that spiral imaging has to offer. The same is true for DWI, although high resolutions at higher field strengths are of increasing interest [54].

The spirals investigated in this project have short TEs and acquisition times. TEs of about 3 ms are mostly relevant for DWI and ASL, as the BOLD fMRI relies on T_2^*-weighed images with TEs in the range of 20-30 ms. However, there are no reasons not to increase the TE-values beyond what is presented in the current work. Due to image artifacts, the highest reasonable R-value that can safely be applied during reconstruction with the GIRF-correction method seems to lie around R = 3, which limits the resolutions to approximately 1.0 mm. However, by increasing the acquisition lengths of the spirals, even higher resolutions may be achieved without increasing the undersampling factor further as long as the resulting increase in off-resonance effects and T_2^*-blurring is not too large. Note that since the thin-slice method for measuring k-space trajectories in this work was limited to an acquisition length of 41 ms, one would not be able to measure the true trajectories before reconstruction, but there is no such limit to the GIRF-predictions. For most applications, acquisition times of approximately 60 ms are sufficient to achieve an acceptable temporal resolution [51]. However, shorter acquisition times can allow for multiple images per readout, as demonstrated with a spiral in-out scheme at 7T by Kasper et al. which increased the contrast-to-noise ratio (CNR) by about 20% [51].

5.4 Further work

The measurements in this work were limited to one slice at isocenter in transversal orientation. Therefore, a natural next step would be to look into other slice orientations as well as multiple slices. Earlier work by Vannesjo et al. on GIRF-predictions on a 3T scanner has reported small differences between the slice orientations [34], but due to the difference in methods for GIRF-determination, it would still be advisable to perform such measurements as a quality measure. Also, the GIRF that was determined by Vannesjo et al. seems to have smaller differences between the responses of the three axes compared to what has been reported in this project. As for more slices, it would be interesting to look into the quality of the reconstructions off-isocenter. In the transversal orientation, a two-dimensional spiral scheme will cause larger concomitant fields further away from the isocenter, which will scale with the square of the gradient strength. This is expected to affect the image quality and may require concomitant field corrections to achieve sufficient quality since the LTI model is incapable of correcting non-linear terms such as concomitant fields. To a first approximation, the concomitant fields amount to a set of second-order field terms, as shown in equation (2.14). Thus, concomitant fields could be corrected for by combining equation (2.14) with a higher-order image reconstruction as in Ref. [24].

The offline reconstruction pipeline presented in this work is time-consuming and depends on a series of steps on different software and locations. For this method to be useful in a clinical context, more work has to be performed to reduce the time and effort in each step and in-between steps. Since the GIRF only has to be determined once and the spiral measurements are only needed as quality assurance, these steps are not as important to streamline compared to the GIRF-prediction and image reconstruction. First of all, there is currently no efficient way to retrieve the gradient waveform from the sequence. In the current pipeline, this is performed by copying a file from the scanner after the sequence has been applied. This file will also be overwritten for each new spiral sequence. Second, the way the code is presented in appendix A, the GIRF-prediction is implemented in Matlab and the image reconstruction is implemented in Julia. Ideally, all steps should be transferred from Matlab and implemented in Julia since that is where the reconstruction is provided and should be the most efficient. Third, the reconstruction code at the point of finishing this project is custom-made for single-shot single-slice spiral sequences. It should ideally be more flexible and allow for multiple slices, contrasts, and interleaves.

To improve the results of the image reconstruction, independent of trajectory type, more work should be put into improving the B_0-correction and sensitivity maps for SENSE to reduce the number of artifacts. The B_0-correction will most likely improve with better field maps, and this should be a priority to get image reconstructions with acceptable levels of off-resonance artifacts. Improved sensitivity maps might mitigate the reduction of residual aliasing that is seen for higher R-values, but is of lesser importance than B_0-correction as the severity of the artifacts is low for R-values below 3. There might also be other causes for the aliasing that has not been covered in the earlier discussion. However, reducing the residual aliasing in the images and allowing for higher R-values will also aid in reducing the off-resonance artifacts in the images. In that sense, improving the B_0-maps and the sensitivity maps will serve the same purpose.

Depending on the future aim for the spiral sequences to be studied, there are several alternatives to single-shot archimedean spirals that might be interesting to look more into, such as interleaved spirals and variable density spirals. The different spiral trajectories are illustrated in figure 5.3, and provide additional advantages or disadvantages depending on the application. Spirals with multiple interleaves will have a higher SNR and fewer artifacts due to phase accumulation, such as off-resonance effects and T_2^*-blurring for higher resolutions, compared to single-shot imaging. This is because each interleave will have a shorter acquisition time while the combination of all interleaves can cover large areas of k-space. However, the overall acquisition time per slice will increase with the number of interleaves, resulting in a lower temporal resolution during time-series imaging which might be undesirable for some applications. Variable density spirals have a higher sampling density at low frequencies before increasing the sampling spacing for higher k-space values, resulting in an oversampling of the central part of k-space which improves the SNR and reduces aliasing artifacts. Despite being faster than multi-leaf spiral imaging, variable density spirals are still less efficient than archimedean spirals in terms of time. Also, variable-density imaging will spend more time at low k-values which might cause more severe off-resonance effects.
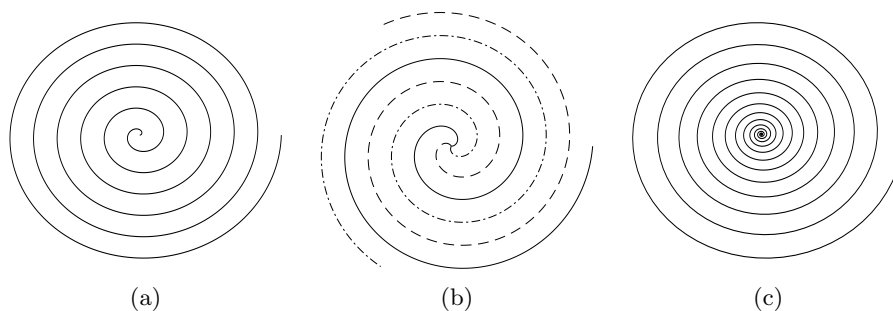

Figure 5.3: Illustrations of different spiral trajecories. (a) Single-shot archimedean spiral, (b) Multi-leaved archimedean spiral, and (c) variable density spiral.

6 Conclusion

In this project, an offline image reconstruction pipeline for single-shot imaging with spiral k-space trajectories has been developed and tested for a 7T MR scanner. The results demonstrate that a GIRF with both self and cross-terms can be determined with simple thin-slice excitation phantom measurements and that the trajectory predictions based on this GIRF yield highly accurate results for the 0th and 1st order field responses for technically challenging single-shot spiral readouts. The results also show that the GIRF-predicted trajectories, together with the predicted B_0 response, enable image reconstruction with the same quality as separately measured trajectories and B_0-responses. Due to off-resonance effects and residual aliasing, the image quality was reduced, and further work should be performed to improve the field maps and sensitivity maps used during reconstruction before the reconstructions can be applied to other projects.

Throughout the different steps of the reconstruction pipeline, from GIRF characterization to iterative reconstruction, the methods have been kept as general as possible in the sense that they are available to all MR sites. The thin-slice excitation method for k-space trajectory measurement does not require any additional hardware, and the code for calculating the GIRF and reconstructing the images is based on open-source code. The measurements and calculations for the GIRF-determination only need to be performed once, and the GIRF can correct for imperfections in any trajectory. In other words, the GIRF-correction pipeline for spiral imaging is available to all MR sites as a feasible and easy way to achieve high-precision trajectory predictions that result in increased MR image quality.

Bibliography

[1] S. Ogawa et al. "Brain magnetic resonance imaging with contrast dependent on blood oxygenation". In: *Proceedings of the National Academy of Sciences* 87 (24 Dec. 1990), pp. 9868–9872. DOI: 10. 1073/PNAS.87.24.9868.

[2] X. Golay, J. Hendrikse, and T. C. C. Lim. "Perfusion imaging using arterial spin labeling". In: *Topics in Magnetic Resonance Imaging* 15 (1 Feb. 2004), pp. 10–27. DOI: 10.1097/00002142-200402000-00003.

[3] R. Bammer. "Basic principles of diffusion-weighted imaging". In: *European Journal of Radiology* 45 (3 Mar. 2003), pp. 169–184. DOI: 10.1016/S0720-048X(02)00303-0.

[4] P. Mansfield. "Multi-planar image formation using NMR spin echoes". In: *Journal of Physics C: Solid State Physics* 10 (3 Feb. 1977), p. L55. DOI: 10.1088/0022-3719/10/3/004.

[5] C. B. Ahn, J. H. Kim, and Z. H. Cho. "High-speed spiral-scan echo planar NMR imaging-I". In: *IEEE Transactions on Medical Imaging* 5 (1 Mar. 1986), pp. 2–7. DOI: 10.1109/TMI.1986.4307732.

[6] A. Deshmane et al. "Parallel MR imaging". In: *Journal of Magnetic Resonance Imaging* 36 (1 July 2012), pp. 55–72. DOI: 10.1002/JMRI.23639.

[7] P. Börnert et al. "Improvements in spiral MR imaging". In: *Magnetic Resonance Materials in Physics, Biology and Medicine 1999 9:1* 9 (1 Oct. 1999), pp. 29–41. DOI: 10.1007/BF02634590.

[8] K. T. Block and J. Frahm. "Spiral imaging: A critical appraisal". In: *Journal of Magnetic Resonance Imaging* 21 (6 June 2005), pp. 657–668. DOI: 10.1002/JMRI.20320.

[9] K. P. Pruessmann et al. "Advances in sensitivity encoding with arbitrary k-space trajectories". In: *Magnetic Resonance in Medicine* 46 (4 Oct. 2001), pp. 638–651. DOI: 10.1002/MRM.1241.

[10] H. Bruder et al. "Image reconstruction for echo planar imaging with nonequidistant k-space sampling". In: *Magnetic Resonance in Medicine* 23 (2 Feb. 1992), pp. 311–323. DOI: 10.1002/MRM.1910230211.

[11] M. H. Buonocore and L. Gao. "Ghost artifact reduction for echo planar imaging using image phase correction". In: *Magnetic Resonance in Medicine* 38 (1 July 1997), pp. 89–100. DOI: 10.1002/MRM.1910380114.

[12] Y. Zhang and F. W. Wehrli. "Reference-scan-free method for automated correction of nyquist ghost artifacts in echoplanar brain images". In: *Magnetic Resonance in Medicine* 51 (3 Mar. 2004), pp. 621–624. DOI: 10.1002/MRM.10724.

[13] W. van der Zwaag et al. "Minimization of Nyquist ghosting for echo-planar imaging at ultra-high fields based on a "negative readout gradient" strategy". In: *Journal of Magnetic Resonance Imaging* 30 (5 Nov. 2009), pp. 1171–1178. DOI: 10.1002/JMRI.21951.

[14] D. M. Spielman and J. M. Pauly. "Spiral imaging on a small-bore system at 4.7t". In: *Magnetic Resonance in Medicine* 34 (4 Oct. 1995), pp. 580–585. DOI: 10.1002/MRM.1910340414.

[15] G. F. Mason et al. "A method to measure arbitrary k-space trajectories for rapid MR imaging". In: *Magnetic Resonance in Medicine* 38 (3 Sept. 1997), pp. 492–496. DOI: 10.1002/MRM.1910380318.

[16] J. H. Duyn et al. "Simple correction method for k-space trajectory deviations in MRI". In: *Journal of Magnetic Resonance* 132 (1 May 1998), pp. 150–153. DOI: 10.1006/JMRE.1998.1396.

[17] Y. Zhang et al. "A novel k-space trajectory measurement technique". In: *Magnetic Resonance in Medicine* 39 (6 June 1998), pp. 999–1004. DOI: 10.1002/MRM.1910390618.

[18] M. T. Alley, G. H. Glover, and N. J. Pelc. "Gradient characterization using a Fourier-transform technique". In: *Magnetic Resonance in Medicine* 39 (4 Apr. 1998), pp. 581–587. DOI: 10.1002/MRM.1910390411.

[19] N. D. Zanche et al. "NMR probes for measuring magnetic fields and field dynamics in MR systems". In: *Magnetic Resonance in Medicine* 60 (1 July 2008), pp. 176–186. DOI: 10.1002/MRM.21624.

[20] C. Barmet et al. "A transmit/receive system for magnetic field monitoring of in vivo MRI". In: *Magnetic Resonance in Medicine* 62 (1 May 2009), pp. 269–276. DOI: 10.1002/MRM.21996.

[21] B. E. Dietrich et al. "A field camera for MR sequence monitoring and system analysis". In: *Magnetic Resonance in Medicine* 75 (4 Apr. 2016), pp. 1831–1840. DOI: 10.1002/MRM.25770.

[22] N. O. Addy, H. H. Wu, and D. G. Nishimura. "Simple method for MR gradient system characterization and k-space trajectory estimation". In: *Magnetic Resonance in Medicine* 68 (1 July 2012), pp. 120–129. DOI: 10.1002/MRM.23217.

[23] S. J. Vannesjo et al. "Gradient system characterization by impulse response measurements with a dynamic field camera". In: *Magnetic Resonance in Medicine* 69 (2 Feb. 2013), pp. 583–593. DOI: 10.1002/MRM.24263.

[24] B. J. Wilm et al. "Higher order reconstruction for MRI in the presence of spatiotemporal field perturbations". In: *Magnetic Resonance in Medicine* 65 (6 June 2011), pp. 1690–1701. DOI: 10.1002/MRM.22767.

[25] Z.-P. Liang and P. C. Lauterbur. *Principles of Magnetic Resonance Imaging: A Signal Processing Perspective.* Vol. 4. John Wiley & Sons, 1999. ISBN: 9780780347236.

[26] S. M. Grieve, A. M. Blamire, and P. Styles. "Elimination of Nyquist ghosting caused by read-out to phase-encode gradient cross-terms in EPI". In: *Magnetic Resonance in Medicine* 47 (2 Feb. 2002), pp. 337–343. DOI: 10.1002/MRM.10055.

[27] B. M. Delattre et al. "Spiral demystified". In: *Magnetic Resonance Imaging* 28 (6 July 2010), pp. 862–881. DOI: 10.1016/J.MRI.2010.03.036.

[28] R. Shankar. *Fundamentals of Physics II: Electromagnetism, Optics, and Quantum Mechanics.* Vol. 2. Yale University Press, 2016. ISBN: 9780300212365.

[29] R. K. Robison et al. "Correction of B0 eddy current effects in spiral MRI". In: *Magnetic Resonance in Medicine* 81 (4 Apr. 2019), pp. 2501–2513. DOI: 10.1002/MRM.27583.

[30] C. Barmet, N. D. Zanche, and K. P. Pruessmann. "Spatiotemporal magnetic field monitoring for MR". In: *Magnetic Resonance in Medicine* 60 (1 July 2008), pp. 187–197. DOI: 10.1002/MRM.21603.

[31] B. U. Foerster, D. Tomasi, and E. C. Caparelli. "Magnetic field shift due to mechanical vibration in functional magnetic resonance imaging". In: *Magnetic Resonance in Medicine* 54 (5 Nov. 2005), pp. 1261–1267. DOI: 10.1002/MRM.20695.

[32] Y. Wu et al. "Gradient-induced acoustic and magnetic field fluctuations in a 4T whole-body MR imager". In: *Magnetic Resonance in Medicine* 44 (4 Oct. 2000), pp. 532–536. DOI: 10.1002/1522-2594(200010)44:4<532::AID-MRM6>3.0.CO;2-Q.

[33] M. Schetzen. *Linear Time-Invariant (LTI) Systems.* IEEE, 2010. ISBN: 9780470545041. DOI: 10.1109/9780470545041.

[34] S. J. Vannesjo et al. "Image reconstruction using a gradient impulse response model for trajectory prediction". In: *Magnetic Resonance in Medicine* 76 (1 July 2016), pp. 45–58. DOI: 10.1002/MRM.25841.

[35] D. K. Sodickson and W. J. Manning. "Simultaneous acquisition of spatial harmonics (SMASH): Fast imaging with radiofrequency coil arrays". In: *Magnetic Resonance in Medicine* 38 (4 Oct. 1997), pp. 591–603. DOI: 10.1002/MRM.1910380414.

[36] M. A. Griswold et al. "Generalized autocalibrating partially parallel acquisitions (GRAPPA)". In: *Magnetic Resonance in Medicine* 47 (6 June 2002), pp. 1202–1210. DOI: 10.1002/MRM.10171.

[37] K. P. Pruessmann et al. "SENSE: Sensitivity encoding for fast MRI". In: *Magnetic Resonance in Medicine* 42 (5 Oct. 1999), pp. 952–962. DOI: `10.1002/(SICI)1522-2594(199911)42:5<952::AID-MRM16>3.0.CO;2-S`.

[38] J. R. Shewchuk. *An Introduction to the Conjugate Gradient Method Without the Agonizing Pain.* Carnegie Mellon University, Pittsburgh, PA, USA, 1994. URL: `https://www.cs.cmu.edu/~quake-papers/painless-conjugate-gradient.pdf`.

[39] J. G. Pipe and N. R. Zwart. "Spiral trajectory design: A flexible numerical algorithm and base analytical equations". In: *Magnetic Resonance in Medicine* 71 (1 Jan. 2014), pp. 278–285. DOI: `10.1002/MRM.24675`.

[40] T. Knopp and M. Grosser. "MRIReco.jl: An MRI reconstruction framework written in Julia". In: *Magnetic Resonance in Medicine* 86 (3 Sept. 2021), pp. 1633–1646. DOI: `10.1002/MRM.28792`.

[41] J. Bezanson et al. "Julia: A fresh approach to numerical computing". In: *SIAM Review* 59 (Mar. 2017), pp. 65–98. DOI: `10.1137/141000671`.

[42] M. Uecker et al. "ESPIRiT—an eigenvalue approach to autocalibrating parallel MRI: Where SENSE meets GRAPPA". In: *Magnetic Resonance in Medicine* 71 (3 Mar. 2014), pp. 990–1001. DOI: `10.1002/MRM.24751`.

[43] W. Li et al. "Acoustic noise analysis and prediction in a 4-T MRI scanner". In: *Concepts in Magnetic Resonance Part B: Magnetic Resonance Engineering* 21B (1 Apr. 2004), pp. 19–25. DOI: `10.1002/CMR.B.20007`.

[44] D. B. Clayton et al. "1H spectroscopy without solvent suppression: Characterization of signal modulations at short echo times". In: *Journal of Magnetic Resonance* 153 (2 Dec. 2001), pp. 203–209. DOI: `10.1006/JMRE.2001.2442`.

[45] G. H. Glover. "Spiral imaging in fMRI". In: *NeuroImage* 62 (2 Aug. 2012), pp. 706–712. DOI: `10.1016/J.NEUROIMAGE.2011.10.039`.

[46] M. Engel et al. "Single-shot spiral imaging at 7T". In: *Magnetic Resonance in Medicine* 80 (5 Nov. 2018), pp. 1836–1846. DOI: `10.1002/MRM.27176`.

[47] J. Busch et al. "Analysis of temperature dependence of background phase errors in phase-contrast cardiovascular magnetic resonance". In: *Journal of Cardiovascular Magnetic Resonance* 16 (1 Dec. 2014), p. 97. DOI: `10.1186/s12968-014-0097-6`.

[48] E. K. Brodsky, A. A. Samsonov, and W. F. Block. "Characterizing and correcting gradient errors in non-cartesian imaging: Are gradient errors linear time-invariant (LTI)?" In: *Magnetic Resonance in Medicine* 62 (6 Dec. 2009), pp. 1466–1476. DOI: `10.1002/MRM.22100`.

[49] J. Nussbaum et al. "Thermal variation in gradient response: Measurement and modeling". In: *Magnetic Resonance in Medicine* 87 (5 May 2022), pp. 2224–2238. DOI: `10.1002/MRM.29123`.

[50] F. G. Goora, B. G. Colpitts, and B. J. Balcom. "Arbitrary magnetic field gradient waveform correction using an impulse response based pre-equalization technique". In: *Journal of Magnetic Resonance* 238 (Jan. 2014), pp. 70–76. DOI: `10.1016/J.JMR.2013.11.003`.

[51] L. Kasper et al. "Advances in spiral fMRI: A high-resolution study with single-shot acquisition". In: *NeuroImage* 246 (1 Feb. 2022), p. 118738. DOI: `10.1016/J.NEUROIMAGE.2021.118738`.

[52] B. J. Wilm et al. "Single-shot spiral imaging enabled by an expanded encoding model: Demonstration in diffusion MRI". In: *Magnetic Resonance in Medicine* 77 (1 Jan. 2017), pp. 83–91. DOI: `10.1002/MRM.26493`.

[53] L. Zhao and J. P. Mugler. "Dual-density and parallel spiral ASL for motion artifact reduction". In: *Proceedings of the 19th Annual Meeting of ISMRM, Montréal, Canada.* 2011. DOI: `10.13140/RG.2.2.17527.62880`.

[54] R. M. Heidemann et al. "Diffusion imaging in humans at 7T using readout-segmented EPI and GRAPPA". In: *Magnetic Resonance in Medicine* 64 (1 July 2010), pp. 9–14. DOI: `10.1002/MRM.22480`.

Appendices

A Code

In this appendix, the code that was implemented to calculate the k-space trajectories and GIRF, as well as the reconstruction code will be presented. The k-space trajectories and GIRF was calculated in MATLAB version R2021b (9.11.0) and is shown in section A.1. The image reconstruction was performed in Julia version 1.7.3 and is provided in section A.2.

A.1 MATLAB

The following MATLAB code is divided into two functions `get_data` and `get_outputs`, and two scripts `calculate_GIRF` and `measured_spiral`. `get_data` is used to retrieve the measurement data from the raw Siemens file in the right format for later calculations. `get_outputs` calculates the the k-space trajectory $\hat{k}$ and ϕ_{B_0} from the data retrieved with `get_data`, as well as the corresponding $\hat{G}$ and B_{0e}. `calculate_GIRF` displays all steps in calculating the GIRF based on raw data from the k-space measurements. `measured_spiral` calculates $\hat{k}$, $\hat{G}$, ϕ_{B_0}, and B_{0e} for the spiral trajectory measurements, as well as performing GIRF-predictions based on the nominal trajectories. Finally, it calculates a time-shift that minimizes the RMS error between the nominal and measured trajectories before all information is stored in a `.mat`-file.

get_data()

```
1  function [data, dt, x0] = get_data(path_to_file, slices)
2  % Retrieves the raw data for the given slices.
3  %
4  % slices is an optional input. If not provided, it will be assigned the
5  % values [1, 4] which corresponds to the outer slices when there is 7
6  % slices in total.
7  %
8  % IN
9  %    path_to_file    [string] path to .dat file with raw data
10 %    slices          [1 x nr_slices] array with desired slice indices
11 %
12 % OUT
13 %    data            [nr_samples x nr_inputs x nr_slices x nr_averages]
14 %                    array with output data
15 %    dt              [float] dwell time (time step) in [s]
16 %    x0              [float] slice position in [m]
17
18 disp("Retrieving data...")
19
20 % Add necessary files to path
21 addpath('code_dependencies\mapVBVD');
22
23 % Retrieve a twix object for the sata
24 twix_obj = mapVBVD(path_to_file);
25
```

```matlab
26  % Read out dt and x0 from the twix object
27  dt = twix_obj.hdr.MeasYaps.sRXSPEC.alDwellTime{1}*1e-9;  % dwelltime in [s]
28  x0 = abs(twix_obj.image.slicePos(3, slices(1)))*1e-3;   % distance in [m]
29
30  % Squeeze the image data and select desired slices
31  data = twix_obj.image{''};
32  data = data(:, :, slices, :, :);
33
34  end
```

get_outputs()

```matlab
1  function [k, G, B0_phase, B0] = get_outputs(data, dt, x0)
2  % Calculates the gradient (G), 0th order spatial component of variations in
3  % B0, and the k-space trajectory (k) based on the data provided.
4  %
5  % The method used for calculation is the one described by Robison et. al
6  % (2018).
7  % NB: assumes only two slices, i.e. nr_slices = 2,  where slice 1 is -x0
8  % and slice 2 is x0.
9  %
10 % IN:
11 %   data    [nr_samples x nr_inputs x nr_slices
12 %           x nr_averages x nr_dimensions] array with sample data
13 %   dt      [double] time step in [s] of samples
14 %   x0      [single] distance in [m] to the slice at position x0
15 %
16 % OUT:
17 %   k        [nr_samples x nr_pos_gradients x nr_dimensions]
18 %            k-space trajectory in [rad/m]
19 %   G        [nr_samples-1 x nr_pos_gradients x nr_dimensions]
20 %            gradient in [T/m]
21 %   B0_phase [nr_samples x nr_pos_gradients x nr_dimensions]
22 %            phase in [rad] of the 0th order spatial component of variations in B0
23 %   B0       [nr_samples-1 x nr_pos_gradients x nr_dimensions]
24 %            0th order spatial component of variations in B0 in [T]
25
26 disp("Calculating measurements...")
27
28 % Crop the first input measurement since there is no need for no gradients.
29 data = data(:, 2:end, :, :, :);
30
31 % Constants
32 gamma = 2.6752218744e+08;   % gyromagnetic ratio of protons in  [rad/(sT)]
33 dims  = size(data);
34 nTs   = dims(1);   % number of timesteps
35 nGs   = dims(2);    % number of applied gradient pulses
36 nSls  = dims(3);    % number of slices
37 nAvs  = dims(4);    % number of averages
38 nDims = dims(5);    % number of dimensions
39
40 % Ensure that only two slices is included, and that there is an even number
41 % of inputs
42 assert(nSls == 2, "Ensure that only the slices at -x0 and +x0 is included in the data.");
43 assert(~mod(nGs, 2), "Number of gradients must be an even number.");
44
45 % Allocate space for results
46 k          = zeros(nTs,   nGs/2, nAvs, nDims);
47 G          = zeros(nTs-1, nGs/2, nAvs, nDims);
48 B0_phase = zeros(nTs,   nGs/2, nAvs, nDims);
49 B0         = zeros(nTs-1, nGs/2, nAvs, nDims);
50
51 % Calculate k and B0 phase
52 for dim = 1:nDims
53     % counter for gradient inputs
54     i = 1;
55     for g = 1:2:nGs
56         for av = 1:nAvs
```

```matlab
57              % Calculate the relative phase at +x0 and -x0
58              phase_posx0 = unwrap(angle(data(:, g, 2, av, dim) ./ data(:, g+1, 2, av, dim)
     ));
59              phase_negx0 = unwrap(angle(data(:, g, 1, av, dim) ./ data(:, g+1, 1, av, dim)
     ));
60
61              % Calculate results
62              k(:, i, av, dim)        = (phase_posx0 - phase_negx0) / (4*x0);
63              G(:, i, av, dim)        = diff(k(:, i, av, dim)) / (dt*gamma);
64              B0_phase(:, i, av, dim) = (phase_posx0 + phase_negx0) / 4;
65              B0(:, i, av, dim)       = diff(B0_phase(:, i, av, dim)) / (dt*gamma);
66          end
67          i = i+1;
68      end
69 end
70
71 % Calculate average over the eight repeated measurements
72 k = squeeze(mean(k, 3));
73 G = squeeze(mean(G, 3));
74 B0_phase = squeeze(mean(B0_phase, 3));
75 B0 = squeeze(mean(B0, 3));
76
77 disp("Done!")
78
79 end
```

calculate_GIRF.m

```matlab
1  clear, clc
2
3  % Add all necessary files to path
4  addpath(genpath('./code/Matlab'));
5  addpath(genpath('./code_dependencies'));
6
7  % Path to data
8  filepath = 'D:\220314_Maren';
9  filenames = {
10     'meas_MID00116_FID41408_t01dt_fid_girf_X.dat',
11     'meas_MID00117_FID41409_t01dt_fid_girf_Y.dat',
12     'meas_MID00118_FID41410_t01dt_fid_girf_Z.dat'
13     };
14
15
16 % Necessary data and constant
17 slices = [1, 4];
18 gamma = 2.6752218744e+08;   % gyromagnetic ratio of protons in  [rad/(sT)]
19
20
21 % Calculate k, G, B0_phase, and B0 %%%%%%%%%%%%%%%%%%%%%%%%%%%%%%%%%%%%%
22 % x-, y- and z are calculated from different measured files
23 switch_dim = [2, 1, 3];
24 for dim = 1:3
25     fprintf("Solving for dimension %i\n", dim)
26
27     % Fetch data, time step (dt) and distance to slices (x0)
28     filename = filenames{dim};
29     [data, dt, x0] = get_data([filepath filesep filename], slices);
30
31     % Calculate outputs with concomitant field correction
32     [ki, Gi, B0_phasei, B0i] = get_outputs(data, dt, x0);
33
34     k(:, :, switch_dim(dim)) = ki(:, :, dim);
35     G(:, :,  switch_dim(dim)) = Gi(:, :, dim);
36     B0_phase(:, :, switch_dim(dim)) = B0_phasei(:, :, dim);
37     B0(:, :, switch_dim(dim)) = B0i(:, :, dim);
38 end
39
40 % More constants
```

```matlab
41  dims = size(G);
42  nTs = dims(1);
43  nIns = dims(2);
44  nDims = dims(3);
45
46  % Time axes
47  tMeas = (1:size(k, 1))*dt - dt/2;    % measured signals (k and B0_phase)
48  tOut  = (1:nTs)*dt;    % calculated output signals (G and B0)
49
50
51  % Filter   %%%%%%%%%%%%%%%%%%%%%%%%%%%%%%%%%%%%%%%%%%%%%%%%%%%%%%%%%%%%
52  G_filtered  =  BWfilter_ft(G, tOut, 60e3, 'rc', 1/4);
53  B0_filtered = BWfilter_ft(B0, tOut, 60e3, 'rc', 1/4);
54  B0_phase_filtered = BWfilter_ft(B0_phase, tMeas, 60e3, 'rc', 1/4);
55
56
57  % Create the input gradient blips %%%%%%%%%%%%%%%%%%%%%%%%%%%%%%%%%%%%
58  tBlips = (1:4096)*10e-6 - 5e-6;
59  nBlips = 7;
60  interval = 20e-6;
61  slewRate = 190.0;
62  tCenter = tBlips(128);   % located at 1/32 of adc (tBlips), i.e. position 128
63
64  % Create blips on the time axis of measured output (G/B0)
65  inBlips = input_blips(tOut, nBlips, tCenter, interval, slewRate);
66  % nominal k-space trajectory
67  % NB: the first point will be located at tMeas(2)!
68  k_nom = gamma*cumsum(inBlips)*dt;   % [rad/m]
69
70
71  % Calculate GIRF %%%%%%%%%%%%%%%%%%%%%%%%%%%%%%%%%%%%%%%%%%%%%%%%%%%%%
72  % Prepare data
73  inChannels = {'X', 'Y', 'Z'};
74  nWs = nIns*nDims;   % Total number of input waves in all directions
75  tIn  = tOut';
76  tOut = tOut';
77  outBasis = 1:4;
78  in  = zeros(nTs, length(inChannels), nWs);
79  out = zeros(nTs, length(outBasis),   nWs);
80
81  % Fill the input and outputs for GIRF calculation
82  for nW = 1:nWs
83      dim = 1+fix((nW-1)/nIns);
84      nIn = nW - (dim-1)*nIns;
85      in(:, dim, nW) = inBlips(:, nIn);
86      out(:, 1, nW) = B0(:, nIn, dim);
87      out(:, dim+1, nW) = G(:, nIn, dim);
88  end
89
90  % Calculate GIRF
91  girf = GirfProvider(tIn, in, tOut, out, inChannels, outBasis);
92  girf.ComputeGirf();
93  girf.WindowFreq(60e3, 'rc', 1/4);
94
95  % save GIRF
96  savepath = './results/GIRF';
97  savename = 'girf_1ch';
98  girf.Save([savepath filesep savename])
99
100 disp(fprintf("Girf saved as %s", savename));
```

measured_spiral.m

```matlab
1  %% CALCULATE MEASURED SPIRAL k-SPACE TRAJECTORIES %%%%%%%%%%%%%%%%%%%%%%%%%
2  clear, clc
3
4  filepath = 'D:\220523_Maren';
5
```

```matlab
filenames = {
    'meas_MID00132_FID46756_t01dt_fid_girf_spiral192mm2p40mmR1.dat',
    'meas_MID00133_FID46757_t01dt_fid_girf_spiral192mm1p39mmR2.dat',
    'meas_MID00134_FID46758_t01dt_fid_girf_spiral192mm1p00mmR3.dat',
    'meas_MID00135_FID46759_t01dt_fid_girf_spiral192mm1p00mmR4.dat',
    'meas_MID00136_FID46760_t01dt_fid_girf_spiral164mm2p00mmR1.dat',
    'meas_MID00137_FID46761_t01dt_fid_girf_spiral164mm1p21mmR2.dat',
    'meas_MID00138_FID46762_t01dt_fid_girf_spiral164mm0p95mmR3.dat',
    'meas_MID00141_FID46763_t01dt_fid_girf_spiral140mm1p71mmR1.dat',
    'meas_MID00143_FID46764_t01dt_fid_girf_spiral140mm1p08mmR2.dat',
    'meas_MID00146_FID46765_t01dt_fid_girf_spiral140mm0p74mmR4.dat'
    };

% Size restriction of G_nom
size_res = 4096;

% Add all necessary files to path
addpath(genpath('./code/Matlab'));
addpath(genpath('./code_dependencies'));

% constants
gamma = 2.6752218744e+08;   % gyromagnetic ratio of protons in  [1/(sT)]
slices = [5, 7];

for spiral = 1:length(filenames)
    fprintf("Spiral nr. %i/%i\n", spiral, length(filenames))

    filename = filenames{spiral};
    G_nom_file = sprintf('ArbGradientRO_%s.txt', filename(end-16:end-4));

    % Retrieve data %%%%%%%%%%%%%%%%%%%%%%%%%%%%%%%%%%%%%%%%%%%%%%%%%%%%
    [data, dt, x0] = get_data_32ch([filepath filesep filename], slices);

    % Sort waveform entries in data to match the structure needed in
    % get_outputs
    data = data(:, :, [3, 1, 2, 4, 5], :, :, [2, 1, 3]);

    % Calculate k, G, B0 and B0-phase %%%%%%%%%%%%%%%%%%%%%%%%%%%%%%%%%%
    [k, G, B0_phase, B0] = get_outputs_32ch(data, dt, x0);

    % Average over index 2 (nr_channels)
    k = squeeze(mean(k, 2));
    G = squeeze(mean(G, 2));
    B0_phase = squeeze(mean(B0_phase, 2));
    B0 = squeeze(mean(B0, 2));

    % Time axes
    tMeas = (1:size(k, 1))*dt - dt/2;   % Time axis of the measured signals (k and
    B0_phase)
    tOut = tMeas(1:end-1) + dt/2;   % Time axis of the calculated input signals (G and B0
    )


    % Filter   %%%%%%%%%%%%%%%%%%%%%%%%%%%%%%%%%%%%%%%%%%%%%%%%%%%%%%%%%%%
    k_filtered =  BWfilter_ft(k, tMeas, 60e3, 'rc', 1/4);
    G_filtered =  BWfilter_ft(G, tOut, 60e3, 'rc', 1/4);
    B0_phase_filtered = BWfilter_ft(B0_phase, tMeas, 60e3, 'rc', 1/4);
    B0_filtered = BWfilter_ft(B0, tOut, 60e3, 'rc', 1/4);

    % Compare with nominal spiral trajectory %%%%%%%%%%%%%%%%%%%%%%%%%%%%
    G_nom = load([filepath filesep G_nom_file]);

    % In all spirals, the gradient input was switched, s.t. G_nom(:, 1) was
    % applied along the y-direction, and G_nom(:, 2) was applied along the
    % x-direction
    G_nom = G_nom*1e-3;   % change units to [T/m]
    tIn = (1:size(G_nom, 1))*1e-5 - 5e-6;   % time axis of nominal gradient

    % Extend G_nom as zeroes to avoid errors when extrapolating
    G_nom_length = size(G_nom, 1);
```

```matlab
74          ext = size_res - size(G_nom, 1);
75          G_nom(end+1:end+ext, :) = zeros(ext, 3);
76          tIn(end+1:end+ext) = tIn(end) + (1:ext)*10e-6;
77
78          % nominal k-space trajectory
79          % NB: time axis is tIn + 5e-6!
80          k_nom = gamma*cumsum(G_nom)*10e-6;
81
82
83          % PREDICT SPIRAL TRAJECTORIES %%%%%%%%%%%%%%%%%%%%%%%%%%%%%%%%%%%%%
84          % Load calculated GIRF
85          girfE = GirfEssential();
86          girfE.Load("./results/GIRF/girf_32ch_34mm.mat");
87
88
89          % Make prediction %%%%%%%%%%%%%%%%%%%%%%%%%%%%%%%%%%%%%%%%%%%%%%%%
90          girfA = GirfApplier(girfE);
91          % Regrid results to tOut
92          [gOut, kOut, tK] = girfA.PredictGrad(tIn', G_nom, tOut');
93
94
95          % Calculate time shift between nominal and measured gradient %%%%%%%%%%%%%
96          % Time shifts to iterate through in [s]
97          tshifts = linspace(-1e-5, 2e-5, 3001);
98
99          % Interpolate G_nom to tOut
100         G_nom_interp = interp1(tIn, G_nom, tOut, "linear", "extrap");
101
102         % Find the timeshift that results in the lowest RMS error
103         [tshiftx, rms_resultsx] = find_delay(G_nom_interp(:, 1), G(:, 1, 1), tOut, tshifts);
104         [tshifty, rms_resultsy] = find_delay(G_nom_interp(:, 2), G(:, 2, 2), tOut, tshifts);
105
106         % Shift the nominal gradient according to the result
107         G_shifted(:, 1) = interp1(tOut, G_nom_interp(:, 1), tOut + tshiftx, 'linear', 'extrap')';
108         G_shifted(:, 2) = interp1(tOut, G_nom_interp(:, 2), tOut + tshifty, 'linear', 'extrap')';
109
110         % Shift k as well
111         k_nom_interp = interp1(tIn+5e-6, k_nom, tK, "linear", "extrap");
112         k_shifted(:, 1) = interp1(tK, k_nom_interp(:, 1), tK + tshiftx, 'linear', 'extrap')';
113         k_shifted(:, 2) = interp1(tK, k_nom_interp(:, 2), tK + tshifty, 'linear', 'extrap')';
114
115         % Print the thime shift
116         fprintf('Delay: %f us in x, %f us in y\n\n', [tshiftx*1e6, tshifty*1e6]);
117
118         % Store results in a struct %%%%%%%%%%%%%%%%%%%%%%%%%%%%%%%%%%%%%%
119         spiral_results.gradient.nominal(:, :, spiral) = G_nom;
120         spiral_results.gradient.nominal_interp(:, :, spiral) = G_nom_interp;
121         spiral_results.gradient.nominal_shifted(:, :, spiral) = G_shifted;
122         spiral_results.gradient.measured(:, :, :, spiral) = G;
123         spiral_results.gradient.measured_filtered(:, :, :, spiral) = G_filtered;
124         spiral_results.gradient.B0(:, :, :, spiral) = B0;
125         spiral_results.gradient.B0_filtered(:, :, :, spiral) = B0_filtered;
126         spiral_results.gradient.predicted(:, :, spiral) = gOut;
127         spiral_results.gradient.t(:, spiral) = tOut;
128         spiral_results.gradient.tNom(:, spiral) = tIn;
129
130         spiral_results.k.nominal(:, :, spiral) = k_nom;
131         spiral_results.k.nominal_interp(:, :, spiral) = k_nom_interp;
132         spiral_results.k.nominal_shifted(:, :, spiral) = k_shifted;
133         spiral_results.k.measured(:, :, :, spiral) = k;
134         spiral_results.k.measured_filtered(:, :, :, spiral) = k_filtered;
135         spiral_results.k.B0phase(:, :, :, spiral) = B0_phase;
136         spiral_results.k.B0phase_filtered(:, :, :, spiral) = B0_phase_filtered;
137         spiral_results.k.predicted(:, :, spiral) = kOut;
138         spiral_results.k.t(:, spiral) = tK;
139         spiral_results.k.tNom(:, spiral) = tIn + 5e-6;
140
141         spiral_results.tshiftx(:, spiral) = tshiftx;
```

```matlab
142     spiral_results.tshifty(:, spiral) = tshifty;
143     spiral_results.specs{spiral} = filename(end-16:end-4);
144     spiral_results.nom_length(spiral) = G_nom_length;
145 end
146
147 % Save results to file %%%%%%%%%%%%%%%%%%%%%%%%%%%%%%%%%%%%%%%%%%%%%
148 fprintf("Saving results... ")
149 save("./results/SpiralMeasurements/spiral_results_32ch_34mm_ny.mat", ...
150     "-struct", "spiral_results");
151 fprintf("Done!")
```

A.2 Julia

The following Julia code consists of three files: `Utils.jl`, `CartesianRecon.jl`, and `SingleShotSpiralRecon.jl`. `Utils.jl` consists of two functions that is used in `CartesianRecon.jl` for calculating B_0-maps and removing oversampling. `CartesianRecon.jl` uses the acquired field map measurements to calculate a sensitivity profile and B_0-map. The sensitivity profile is calculated from the raw measurement data, while the B_0-map is calculated from the reconstructed images. `SingleShotSpiralRecon.jl` reconstructs single-shot spiral images.

Utils.jl

```julia
1  using ROMEO, PyPlot , HDF5, MRIReco
2
3  ## function to calculate the B0 maps from the two images with different echo times
4  function calculateB0Maps(imData,slices)
5
6      b0Maps = mapslices(x -> ROMEO.unwrap(x), angle.(imData[:,:,slices,2,1].*conj(imData
       [:,:,slices,1,1])),dims=(1,2))./((5.1-4.08)/1000)
7
8  end
9
10
11 """
12 removeOversampling!(raw::RawAcquisitionData; dims = 1)
13 removes 2x readout oversampling in specified raw data dimensions by iFFT, cropping FOV
       and FFT
14 # Arguments
15 * `raw::RawAcquisitionData{T}`          - RawAcquisitionData object
16 * `dims`                                - dimension alongside which oversampling is
       removed (default: 1)
17 """
18 function removeOversampling!(raw::RawAcquisitionData; dims = [1])
19     idxDim = dims[1]
20     Ns = raw.params["encodedSize"][idxDim]
21     idxCropFov = convert(Vector{Int64}, [1:floor(Ns/4); ceil(3/4*Ns+1):Ns])
22     # For every profile in the acquisition
23     for iProfile = 1:length(raw.profiles)
24         # IFFT to image space, crop, FFT back to k-space
25         ifft!(raw.profiles[iProfile].data, idxDim)
26         raw.profiles[iProfile].data = fft!(raw.profiles[iProfile].data[idxCropFov,:],
       idxDim)
27
28     end
29
30     # halve encoding size of first dimension
31     raw.params["encodedSize"][idxDim] /= 2
32     raw.params["encodedFOV"][idxDim] /= 2
33
34 end
```

CartesianRecon.jl

```julia
1  using PyPlot, HDF5, MRIReco, LinearAlgebra, DSP, FourierTools, ROMEO
2
3  include("../utils/Utils.jl")
4
5  ## Load data files
6  filepath = "data/Fieldmaps/inVivo_fieldMap_220mm.h5"
7  resolution = 2
8
9  @info "Loading Data Files"
10 dataFileCartesian = ISMRMRDFile(filepath)
11
```

```julia
12  # read in the raw data from the ISMRMRD file into a RawAcquisitionData object
13  r = RawAcquisitionData(dataFileCartesian)
14  removeOversampling!(r)
15
16  # Convert to acquisitionData
17  acqDataCartesian = AcquisitionData(r, estimateProfileCenter=true)
18
19  # Shift image to the left
20  mmshift = 10
21  for s = 1:size(acqDataCartesian.kdata, 1)
22      local k = acqDataCartesian.traj[s].nodes[2, :]
23      for c = 1:size(acqDataCartesian.kdata[s], 2)
24          acqDataCartesian.kdata[s][:, c] = acqDataCartesian.kdata[s][:, c] .* exp.((im*2*
      pi*mmshift/resolution) .* k)
25      end
26  end
27
28  # Define coils and slices
29  nCoils = size(acqDataCartesian.kdata[1], 2)
30  nSlices = numSlices(acqDataCartesian)
31
32
33  @info "Calculating Sense Maps"
34  senseCartesian = espirit(acqDataCartesian, (6,6), 30, eigThresh_1=0.01, eigThresh_2=0.98)
35
36
37  @info "Setting Parameters"
38  paramsCartesian = Dict{Symbol,Any}() # instantiate dictionary
39  paramsCartesian[:reco] = "multiCoil" # choose multicoil reconstruction
40  paramsCartesian[:reconSize] = (acqDataCartesian.encodingSize[1], acqDataCartesian.
      encodingSize[2])
41  paramsCartesian[:regularization] = "L2" # choose regularization for the recon algorithm
42  paramsCartesian[:lambda] = 1.e-9 # recon parameter (there may be more of these, need to
      dig into code to identify them for solvers other than cgnr)
43  paramsCartesian[:iterations] = 5 # number of CG iterations
44  paramsCartesian[:solver] = "cgnr" # inverse problem solver method
45  paramsCartesian[:solverInfo] = SolverInfo(ComplexF32,store_solutions=false) # turn on
      store solutions if you want to see the reconstruction convergence (uses more memory)
46  paramsCartesian[:senseMaps] = ComplexF32.(senseCartesian) # set sensitivity map array
47
48
49  @info "Performing Reconstruction"
50  cartesianReco = reconstruction(acqDataCartesian, paramsCartesian)
51  resampledRecon = mapslices(x->FourierTools.resample(x, (200, 200)), cartesianReco.data;
      dims=[1, 2])
52
53  ## Calculate B0 maps from the acquired images (if two TEs)
54  b0Maps = calculateB0Maps(resampledRecon, 1)
55
56  # Apply a mask to remove contributions from outside the phantom
57  absData = abs.(resampledRecon[:, :, 1, 1, 1]) ./ maximum(abs.(resampledRecon[:, :, 1, 1,
      1]))
58  mask = absData .> 0.09
```

SingleShotSpiralRecon.jl

```julia
1   using MRIReco, PyPlot, DSP, MAT, Dierckx, ROMEO, JLD, DelimitedFiles
2
3
4   # Retrieve sensitivity and B0-maps from fieldMap measurement
5   include("../recon/CartesianRecon.jl")
6   ref107 = matread("data/Fieldmaps/107_Ref.mat")
7   b0Maps = reverse(ref107["B0map"], dims=2)
8   mask = reverse(ref107["reconMask"], dims=2)
9
10  # Input info, change this to change which measurement to recontstruct
11  fov = 192   # Field of view [mm]
12  resolution = 1.00   # Resolution [mm]
```

```julia
13 R = 3    # Acceleration factor
14 trajType = "meas"     # "nom", "nom_dc", "pred", or "meas"
15 applyk0corr = true
16 applyB0corr = true
17 saveImage = false
18
19 # Find names of files
20 (fres, ires) = modf(resolution)
21 fres = Int16(round(fres, digits=2)*100)
22 ires = Int16(ires)
23
24 spiral = "$(fov)mm$(ires)p$(lpad(fres, 2, '0'))mmR$R"
25
26 # Input filenames
27 dataFilename = "data/Spirals/32ch_$spiral.h5"
28 trajFilename = "data/Trajectories/k_$(trajType)_$(spiral).txt"
29
30 # Set encoding and reconstruction FOV
31 encFOV = (fov, fov)
32 reconFOV = (192, 192)
33
34 # Calculate encoding size from resolution and fov
35 # NB: must be an even number
36 if iseven(round(fov/resolution))
37   eS = Int64(round(fov/resolution))
38 else
39   eS = Int64(round(fov/resolution)) - 1
40 end
41
42 # Calculate recon size from resolution and fov
43 # NB: must be an even number
44 if iseven(round(reconFOV[1]/resolution))
45   rS = Int64(round(reconFOV[1]/resolution))
46 else
47   rS = Int64(round(reconFOV[1]/resolution)) - 1
48 end
49
50 # Set parameters relevant for reconstruction
51 encSize = (eS, eS)
52 reconSize = (rS, rS)
53 delay = 0.0
54 dt_s = 2.5*10^(-6)
55 dt_k = 2.5*10^(-6)
56
57
58 @info "Loading data files"
59 # Read in as ISMRMRD-format
60 dataFile = ISMRMRDFile(dataFilename)
61
62 # Read in RawAcquisitionData from ISMRMRD-file
63 rawData = RawAcquisitionData(dataFile)
64
65 ## Update information in rawData
66 rawData.params["reconSize"][2] = reconSize[2]
67 rawData.params["reconFOV"][2] = reconFOV[2]
68 rawData.params["encodedSize"][2] = encSize[2]
69 rawData.params["encodedFOV"][2] = encFOV[2]
70 if size(rawData.profiles, 1) == 22
71   rawData.profiles = rawData.profiles[3:end]
72 end
73
74
75 @info "Loading trajectory"
76 # Retrieve trajectory from gradient file
77 trajData = readdlm(trajFilename,',','\n')
78
79 B0_phase = trajData[:, 1];  # in [rad]
80 k_traj = trajData[:, 2:end];  # in [rad/m]
81
82 # Convert to to [1/m]
```

```julia
83  k_traj ./= (2*pi)
84
85  # Convert to dimensionless form used by MRIReco (k = [-0.5, 0.5])
86  k_traj[:, 1] = k_traj[:, 1] .* encFOV[1] / encSize[1] / 1000;
87  k_traj[:, 2] = k_traj[:, 2] .* encFOV[2] / encSize[2] / 1000;
88
89  # Permute directions to [sample_nr, dimension]
90  k_traj = permutedims(k_traj, [2, 1])
91
92  # Create trajectory object
93  traj = Trajectory(k_traj, 1, size(k_traj, 2), TE=0.0, AQ=size(k_traj, 2)*1e-6, numSlices
        =1, cartesian=false, circular=true)
94
95
96  @info "Synchronizes trajectory data and k-space data onto same time grid"
97  ## Interpolate trajectory onto same times as the sampled signal
98  ### Get size of trajectory and signal vectors
99  Ns = size(rawData.profiles[1].data, 1)
100 Nk = size(traj.nodes, 2)
101
102 ### Define time vectors for signal and trajectory
103 t_s = (1:Ns)*dt_s .- dt_s/2
104 if trajType == "meas"
105   t_k = (1:Nk)*dt_k .- dt_k/2
106 else
107   t_k = (1:Nk)*dt_k .+ dt_k/2
108 end
109
110 ### Interpolate trajectory onto the same sample times as the sampled signal
111 trajNodes_interpolated_X = Spline1D(t_k, traj.nodes[1,:], w=ones(length(traj.nodes[1,:]))
        , k=3)
112 trajNodes_interpolated_Y = Spline1D(t_k, traj.nodes[2,:], w=ones(length(traj.nodes[1,:]))
        , k=3)
113 B0_phase_spline = Spline1D(t_k, B0_phase, w=ones(length(B0_phase)), k=3)
114 B0_phase = B0_phase_spline(t_s)
115
116 ### Concatenate the trajectory node kx and ky positions
117 adjustedTraj = vcat(trajNodes_interpolated_X(t_s)', trajNodes_interpolated_Y(t_s)')
118
119 ## Add trajectory to RawAcquisitionData.profiles[i]
120 if idx_crop != 0
121   for i = 1:length(rawData.profiles)
122     rawData.profiles[i].traj = adjustedTraj[:, 1:idx_crop]
123     rawData.profiles[i].data = rawData.profiles[i].data[1:idx_crop, :]
124   end
125   t_s = t_s[1:idx_crop]
126   B0_phase = B0_phase[1:idx_crop]
127 else
128   for i = 1:length(rawData.profiles)
129     rawData.profiles[i].traj = adjustedTraj
130   end
131 end
132
133 # Adjust header (see adjustHeader! in Utils.jl:223)
134 for i = 1:length(rawData.profiles)
135
136     # Set the discard post to 0 (don't discard any samples from the end of the
        acquisition)
137     rawData.profiles[i].head.discard_post = 0
138
139     # Set the discard pre to 0 (don't discard any samples from the beginning of the
        acqustion)
140     rawData.profiles[i].head.discard_pre = 0
141
142     ## Set the number of samples properly
143     rawData.profiles[i].head.number_of_samples = Ns
144
145     ## Set center sample to 0 (only for spiral scans)
146     rawData.profiles[i].head.center_sample = 0
147
```

```julia
148     end
149
150     # Convert RawAcquisitionData to AcquisitionData
151 @info "Converting RawAcquisitionData to AcquisitionData"
152 acqData = AcquisitionData(rawData, estimateProfileCenter=true)
153
154 ## Update acqData.traj
155 for i = 1:length(acqData.traj)
156     acqData.traj[i].times = t_s # set times to the total time vector
157     acqData.traj[i].TE = 0.00 # set the TE to 0
158     acqData.traj[i].AQ = t_s[end] # set the acquisition time to the last element of the
        time vector (should be the latest time)
159     acqData.traj[i].circular = false # set whether to use a circular filter on the kspace
        data
160 end
161
162 # Shift image to the left
163 mmshift = 10
164 k = acqData.traj[1].nodes[2, :]
165 for s = 1:size(acqData.kdata, 3)
166     for c = 1:size(acqData.kdata[s], 2)
167         acqData.kdata[s][:, c] = acqData.kdata[s][:, c] .* exp.((im*2*pi*mmshift/
        resolution) .* k)
168     end
169 end
170
171 if applyk0corr
172     @info "Correct for B0-phase"
173     for numRep = 1:20
174         acqData.kdata[numRep] = acqData.kdata[numRep] .* exp.(-1im .* B0_phase)
175     end
176 end
177
178 # Check acquisition nodes
179 acqData.traj[1].nodes[acqData.traj[1].nodes[:] .> 0.5] .= 0.5
180 acqData.traj[1].nodes[acqData.traj[1].nodes[:] .< -0.5] .= -0.5
181
182
183 @info "Validating Sense Maps \n"
184 # Resize sense maps to match encoding size of data matrix
185 sensitivity = mapslices(x->imresize(x, (reconSize[1], reconSize[2])), senseCartesian,
        dims=[1,2])
186
187
188 @info "Validating B0 Maps \n"
189 # Resize B0-maps and signal mask to match encoding size of data matrix
190 resizedB0 = mapslices(x->imresize(x, (reconSize[1], reconSize[2])), b0Maps, dims=[1,2])
191 resized_mask = mapslices(x->imresize(x, (reconSize[1], reconSize[2])), mask, dims=[1,2])
192
193
194 @info "Setting reconstruction parameters"
195 # Set reconstruction parameters
196 params = Dict{Symbol,Any}()
197 params[:reco] = "multiCoil"
198 params[:reconSize] = reconSize
199 params[:regularization] = "L2"
200 params[:lambda] = 1.0e-9
201 params[:iterations] = 10
202 params[:solver] = "cgnr"
203 params[:normalizeReg] = true
204 params[:solverInfo] = SolverInfo(ComplexF32, store_solutions=false)
205 params[:senseMaps] = ComplexF32.(sensitivity[:,:,[1],:])
206 if applyB0corr
207     params[:correctionMap] = ComplexF32.(1im.*resizedB0)
208 end
209
210
211 @info "Performing reconstruction"
212 # Perform reconstruction
213 reco = reconstruction(acqData, params)
```

```
214
215 # Save images
216 if saveImage
217   @info "Saving images to file"
218   filename = "./data/Reconstructions/$(spiral)_$(trajType)"
219   if applyB0corr
220     filename = "$(filename)_wB0"
221   end
222   if applyk0corr
223     filename = "$(filename)_wk0"
224   end
225   save("$(filename).jld", "reco", reco.data)
226 end
```

B   GIRF for 32-channel head-coil

This appendix presents the results of the triangle gradient measurements and GIRF-calculation for the 32-channel head receive coil. For a more detailed description and comparison with the one-channel head receive coil, see Results section 4.1.

B.1   Measured response to triangle gradients

The upper row of figure B.1 shows the calculated k-space trajectory and the lower row shows the ϕ_{B_0} of the triangle gradient measurements. The column to the left shows the entire time course of the measurements, while the column to the right is zoomed in on times around the application of the triangle pulses.

The upper row of figure B.2 shows the calculated gradient and the lower row shows the B_{0e} of the triangle gradient measurements. The column to the left shows the entire time course of the measurements, while the column to the right is zoomed in on times around the application of the triangle pulses.
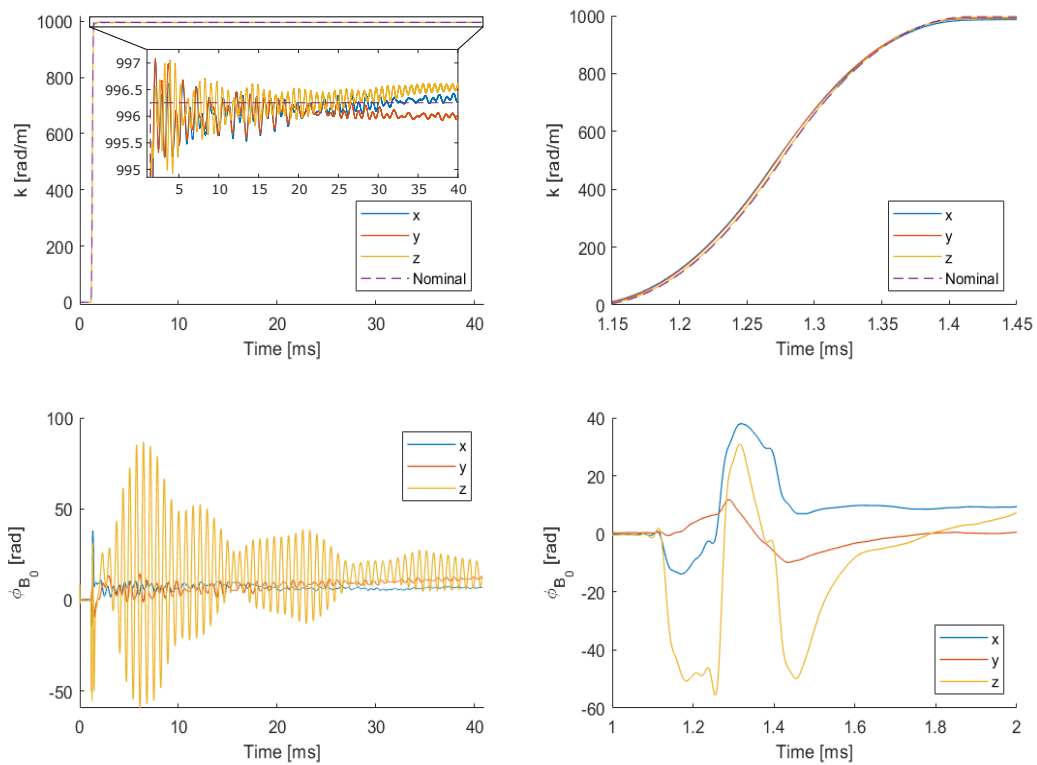
Figure B.1: Measured k (upper row) and B_0-phase ϕ_{B_0} (lower row) of the largest triangle gradient with a maximum amplitude of 26.6 mT/m measured with a 32-channel head-coil. The column to the left show the entire acquisition, while the column to the right displays the data for a short time interval around the application of the gradient pulse.
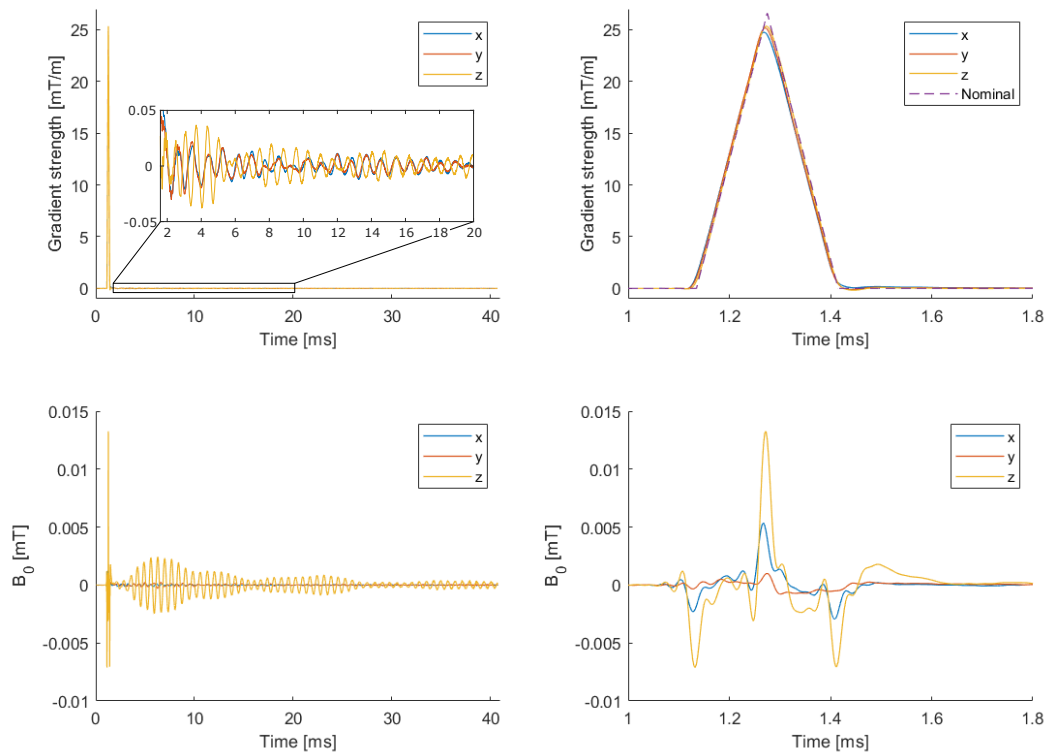
Figure B.2: Measured G (upper row) and B_0 (lower row) of the largest triangle gradient with a maximum amplitude of 26.6 mT/m measured with a 32-channel head-coil. The column to the left show the entire acquisition, while the column to the right displays the data for a short time interval around the application of the gradient pulse.

B.2   GIRF

Figure B.4 shows the calculated cross-response of the gradient system with the 32-channel head coil. The upper row shows the magnitude of the response, and the phase of the response is presented in the lower row. The left column shows the response for the whole frequency range until the magnitude response reaches zero, while the right column is zoomed in on positive frequencies below 2.5 kHz.

Figure B.3 shows the calculated self-response of the gradient system with the 32-channel head coil. The figure to the left contains the magnitude of the response and the figure to the left displays the phase of the response. The phase has not been unwrapped due to the low signal that causes a lot of noise for frequencies near zero.

Figure B.5 shows the GIRF of the gradient system with the 32-channel head coil in the time domain. The self- and cross-responses are displayed in the left and right figures, respectively. To better see the differences between the responses along the x-, y-, and z-directions, a vertical shift has been applied.
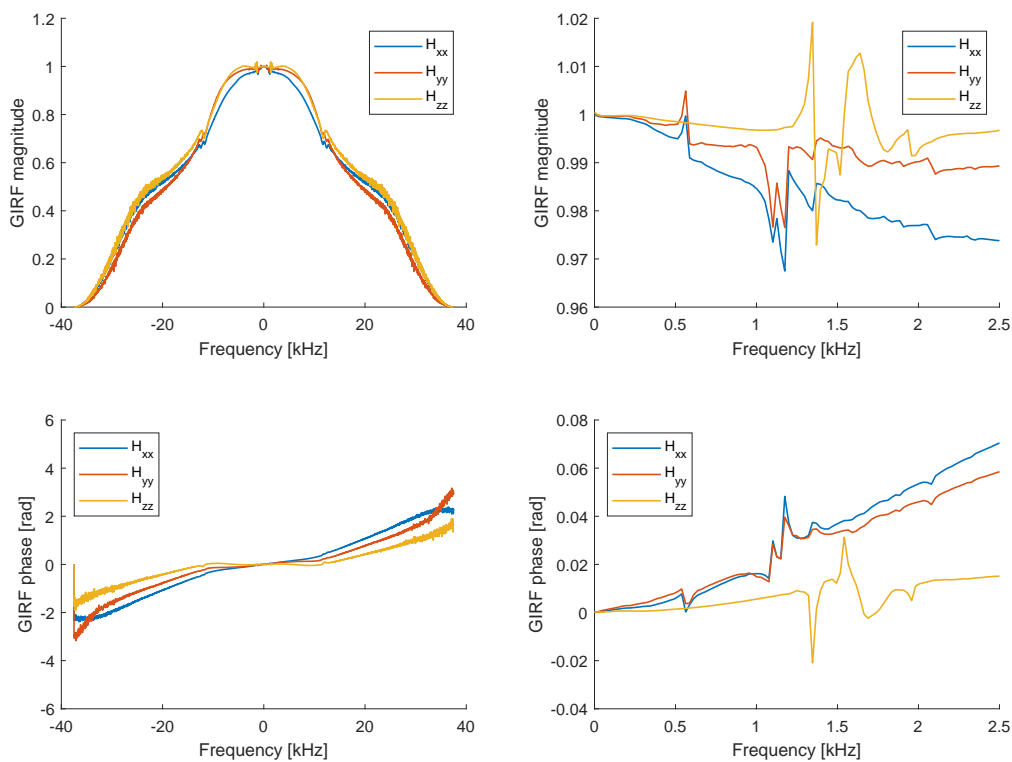
Figure B.3: Magnitude (upper row) and phase (lower row) of the GIRF describing the self-response of the gradient system with a 32-channel head coil. The column to the left shows the whole frequency domain, and the column to the right is zoomed in to low positive frequencies.
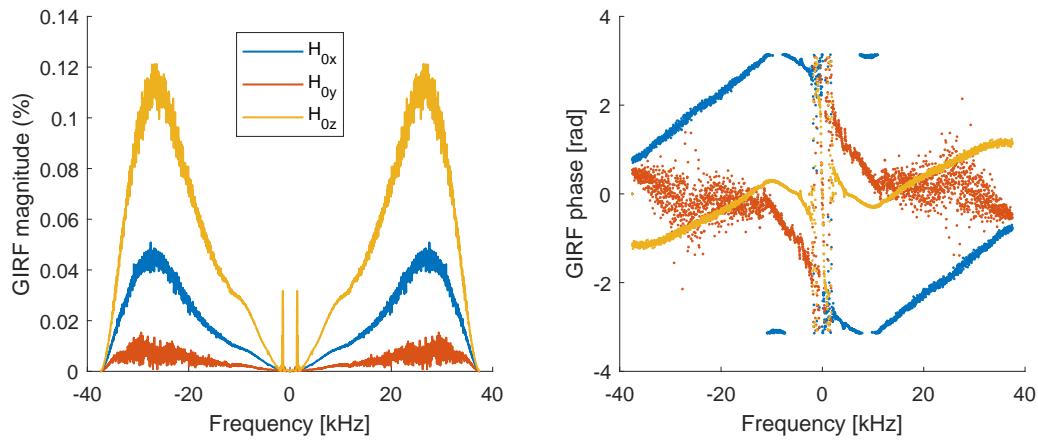
Figure B.4: Magnitude scaled to percent of input (left) and phase (right) of the GIRF describing the cross-response of the gradient system with a 32-channel head coil
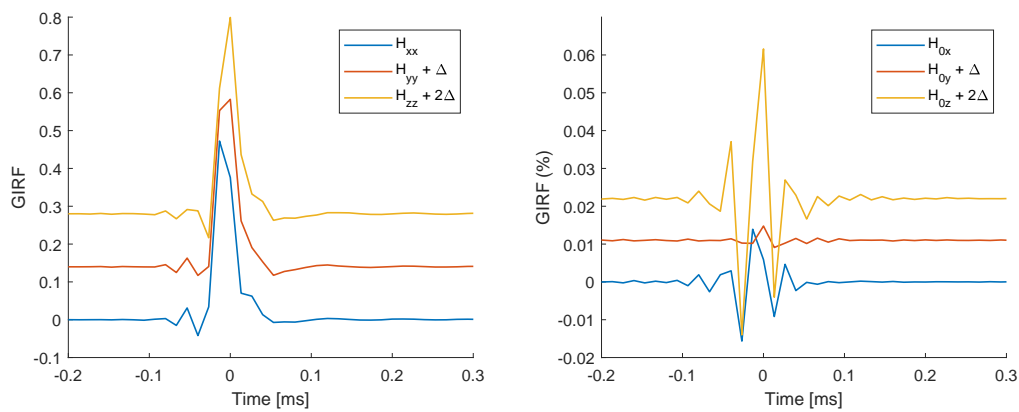

Figure B.5: GIRF in the time domain for the gradient (left) and B_0 (right) responses of the gradient system with a 32-channel head coil. Vertical shifts (Δ) are added to the y- and z-components for better readability.

C   RMS for all spiral trajectory measurements

This appendix contains the RMS values of the difference between the measured values and the nominal, nominal delay-corrected, or predicted values for all spiral sequences included in this project. The values included in table C.1 are the RMS difference of $\hat{k}$, $\hat{G}$, and B_{0e}.

Table C.1: RMS-values of the difference between the measured values and the GIRF-predicted (pred), nominal delay-corrected (nom dc), and nominal (nom) values, for all spiral trajectories included in this work.

Res [mm]	SENSE	Coil	RMS for k [rad/m]			RMS for G_x [mT/m]			RMS for B_0 [μT]	
			Pred	Nom dc	Nom	Pred	Nom dc	Nom	Pred	Nom
2.40	1x	1ch	1.4	11.0	12.8	0.023	0.143	0.190	0.34	1.20
2.00	1x	1ch	0.9	11.5	12.7	0.017	0.137	0.172	0.20	0.93
2.40	1x	32ch	0.8	10.0	16.7	0.018	0.123	0.275	0.25	0.82
1.39	2x	32ch	1.0	13.6	20.5	0.018	0.129	0.266	0.24	0.69
1.00	3x	32ch	1.8	16.1	22.3	0.025	0.144	0.268	0.27	0.84
2.00	1x	32ch	0.9	11.3	18.6	0.018	0.127	0.283	0.25	0.78
1.21	2x	32ch	1.2	14.7	21.1	0.019	0.133	0.259	0.25	0.70
1.71	1x	32ch	1.0	12.6	20.2	0.019	0.132	0.288	0.25	0.76
1.08	2x	32ch	1.5	14.8	20.5	0.022	0.132	0.245	0.25	0.79
0.74	4x	32ch	1.3	10.8	19.5	0.017	0.077	0.179	0.29	0.62